

REPORT DOCUMENTATION PAGE			Form Approved OMB NO. 0704-0188		
<p>The public reporting burden for this collection of information is estimated to average 1 hour per response, including the time for reviewing instructions, searching existing data sources, gathering and maintaining the data needed, and completing and reviewing the collection of information. Send comments regarding this burden estimate or any other aspect of this collection of information, including suggestions for reducing this burden, to Washington Headquarters Services, Directorate for Information Operations and Reports, 1215 Jefferson Davis Highway, Suite 1204, Arlington VA, 22202-4302. Respondents should be aware that notwithstanding any other provision of law, no person shall be subject to any penalty for failing to comply with a collection of information if it does not display a currently valid OMB control number. PLEASE DO NOT RETURN YOUR FORM TO THE ABOVE ADDRESS.</p>					
1. REPORT DATE (DD-MM-YYYY) 18-01-2015		2. REPORT TYPE Ph.D. Dissertation		3. DATES COVERED (From - To) -	
4. TITLE AND SUBTITLE Turbulent Coolant Dispersion in the Wake of a Turbine Vane Trailing Edge			5a. CONTRACT NUMBER W911NF-11-1-0506		
			5b. GRANT NUMBER		
			5c. PROGRAM ELEMENT NUMBER 611102		
6. AUTHORS Sayuri Yapa			5d. PROJECT NUMBER		
			5e. TASK NUMBER		
			5f. WORK UNIT NUMBER		
7. PERFORMING ORGANIZATION NAMES AND ADDRESSES Stanford University 3160 Porter Drive, Suite 100  Palo Alto, CA 94304 -8445			8. PERFORMING ORGANIZATION REPORT NUMBER		
9. SPONSORING/MONITORING AGENCY NAME(S) AND ADDRESS (ES) U.S. Army Research Office P.O. Box 12211 Research Triangle Park, NC 27709-2211			10. SPONSOR/MONITOR'S ACRONYM(S) ARO		
			11. SPONSOR/MONITOR'S REPORT NUMBER(S) 59164-EG.7		
12. DISTRIBUTION AVAILABILITY STATEMENT Approved for public release; distribution is unlimited.					
13. SUPPLEMENTARY NOTES The views, opinions and/or findings contained in this report are those of the author(s) and should not be construed as an official Department of the Army position, policy or decision, unless so designated by other documentation.					
14. ABSTRACT Magnetic resonance-based velocity (MRV) and concentration (MRC) measurements were performed to measure the time averaged three-dimensional, three-component velocity and scalar concentration fields in a double passage vane cascade representative of a high pressure turbine vane from a gas turbine engine. The understanding and prediction of the highly three-dimensional flow and heat transfer in a modern gas turbine engine is a problem that has not been solved over many years of turbomachinery research. Turbine blades and vanes are both internally and externally cooled to withstand the hot gas environment. The external film cooling is generally fed by discrete holes					
15. SUBJECT TERMS Gas Turbine, Film Cooling, Magnetic Resonance Imaging, Turbulent Mixing, Hot Streaks					
16. SECURITY CLASSIFICATION OF:		17. LIMITATION OF ABSTRACT	15. NUMBER OF PAGES	19a. NAME OF RESPONSIBLE PERSON	
a. REPORT	b. ABSTRACT			c. THIS PAGE	John Eaton
UU	UU	UU	UU	19b. TELEPHONE NUMBER 650-723-1971	

## Report Title

Turbulent Coolant Dispersion in the Wake of a Turbine Vane Trailing Edge

### ABSTRACT

Magnetic resonance-based velocity (MRV) and concentration (MRC) measurements were performed to measure the time averaged three-dimensional, three-component velocity and scalar concentration fields in a double passage vane cascade representative of a high pressure turbine vane from a gas turbine engine. The understanding and prediction of the highly three-dimensional flow and heat transfer in a modern gas turbine engine is a problem that has not been solved over many years of turbomachinery research. Turbine blades and vanes are both internally and externally cooled to withstand the hot gas environment. The external film cooling is generally fed by discrete holes on the vane surface, except for at the trailing edge which is cooled by slots that are cut into the pressure side of the vane. Hot streaks from the combustor and cool streaks from the vane film cooling impose strong inlet temperature variations on the turbine blades, which can lead to local hot or cold spots, high thermal stresses, and fatigue failures. Furthermore, the complex three dimensional flows around the vane may act to concentrate cool or hot fluid exiting the vane row. Experiments were performed to show the validity of the application of the scalar transport analogy to the study of turbulent thermal energy transport using turbulent passive scalar transport studies. These experiments were conducted in a three-dimensional mixing layer in the wake of a blunt splitter plate built into two identical test sections. One test section was magnetic resonance-compatible and used water as the working fluid and the other was adapted for high subsonic Mach number air flows and allowed physical access for a thermocouple probe to take temperature profiles. In the water-based MRV/MRC experiments, the mainstream flow was water and the secondary flow was a copper sulfate solution. In the air experiments, the main flow was room temperature air and the secondary flow was heated. The energy separation effect due to coherent vortex structures in the compressible flow experiments affected the measured temperature profile because of the small difference in stagnation temperature between the two flows. This effect is expected to be negligible in the high temperature difference flows found in real engine conditions. This effect is easily corrected in the temperature profiles extracted from this experiment. The agreement between the corrected temperature and concentration data was found to be excellent, validating the application of MRC for quantitative measurement of thermal transport in turbomachinery components via the scalar transport analogy. The MRV/MRC experimental technique was applied to the study of turbulent dispersion of coolant injected through the trailing edge cooling slots, with the focus on dispersion in the vane wake. A new high concentration MRC technique was developed to provide accurate measurements in the far wake of the turbine vane. Three component velocity data showed the development of the passage vortex, a key element of the vane secondary flows. This mean flow structure is the dominant mechanism for turbulent mixing near the cascade endwalls. However, strong variations in coolant concentration remained in the wake downstream of the center span region. Asymmetric dispersion in this region indicated that longitudinal vortices shed from the coolant injection structures played a dominant role in the wake spreading. A separate experiment was performed to evaluate the behavior of the dispersion of combustor hot streaks in the turbine vane cascade. The velocity and concentration distributions were evaluated using the MRV/MRC technique. Streamtubes and concentration isosurfaces reveal that the streaks spread slowly as they pass through the cascade. This suggests that turbulence suppression by strong acceleration plays a significant role in maintaining the streaks. It is important to note that coherent hot streaks still exist at the exit of the test section in the far wake of the vane. The concluding message for these experiments is that the temperature distributions of the gases impacting the blades downstream of the turbine vanes remains significantly non-uniform and that accurate prediction of the temperature distribution downstream of the vanes is critical for advanced turbine design.

TURBULENT COOLANT DISPERSION  
IN THE WAKE OF A TURBINE VANE TRAILING EDGE

A DISSERTATION  
SUBMITTED TO THE DEPARTMENT OF MECHANICAL  
ENGINEERING  
AND THE COMMITTEE ON GRADUATE STUDIES  
OF STANFORD UNIVERSITY  
IN PARTIAL FULFILLMENT OF THE REQUIREMENTS  
FOR THE DEGREE OF  
DOCTOR OF PHILOSOPHY

Sayuri D. Yapa

January 2015

# Abstract

Magnetic resonance-based velocity (MRV) and concentration (MRC) measurements were performed to measure the time-averaged, three-dimensional, three-component velocity and scalar concentration fields in a double passage vane cascade representative of a high pressure turbine vane from a gas turbine engine. The understanding and prediction of the highly three-dimensional flow and heat transfer in modern gas turbine engines is a problem that has not been solved over many years of turbomachinery research. Turbine vanes and blades are both internally and externally cooled to withstand the hot gas environment. The external film cooling is generally fed by discrete holes on the vane surface, except for at the trailing edge, which is cooled by slots that are cut into the pressure side of the vane. Hot streaks from the combustor and cool streaks from the vane film cooling impose strong inlet temperature variations on the turbine blades, which can lead to local hot or cold spots, high thermal stresses, and fatigue failures. Furthermore, the complex three dimensional flows around the vane may act to concentrate cool or hot fluid exiting the vane row.

Experiments were performed to show the validity of the application of the scalar transport analogy to the study of turbulent thermal energy transport using turbulent passive scalar transport studies. These experiments were conducted in a three-dimensional mixing layer in the wake of a blunt splitter plate built into two identical test sections. One test section was magnetic resonance-compatible and used water as the working fluid and the other was adapted for high subsonic Mach number air

flows and allowed physical access for a thermocouple probe to take temperature profiles. In the water-based MRV/MRC experiments, the mainstream flow was water and the secondary flow was a copper sulfate solution. In the air experiments, the main flow was room temperature air and the secondary flow was heated. The energy separation effect due to coherent vortex structures in the compressible flow experiments affected the measured temperature profile because of the small difference in stagnation temperature between the two flows. This effect is expected to be negligible in the high temperature difference flows found in real engine conditions. This effect is easily corrected in the temperature profiles extracted from this experiment. The agreement between the corrected temperature and the concentration data was found to be excellent, validating the application of MRC for quantitative measurement of thermal transport in turbomachinery components via the scalar transport analogy.

The MRV/MRC experimental technique was applied to the study of turbulent dispersion of coolant injected through trailing edge cooling slots, with the focus on dispersion in the vane wake. A new high concentration MRC technique was developed to provide accurate measurements in the far wake of the turbine vane. Three component velocity data showed the development of the passage vortex, a key element of the vane secondary flows. This mean flow structure is the dominant mechanism for turbulent mixing near the cascade endwalls. However, strong variations in coolant concentration remained in the wake downstream of the center span region. Asymmetric dispersion in this region indicated that longitudinal vortices shed from the coolant injection structures played a dominant role in the wake spreading.

A separate experiment was performed to evaluate the behavior of the dispersion of combustor hot streaks in the turbine vane cascade. The velocity and concentration distributions were evaluated using the MRV/MRC experimental technique. Streamtubes and concentration isosurfaces reveal that the streaks spread slowly as they pass

through the cascade. This suggests that turbulence suppression by strong acceleration plays a significant role in maintaining the streaks. It is important to note that coherent hot streaks still exist at the exit of the test section in the far wake of the vane. The concluding message from these experiments is that the temperature distribution of the gases impacting the blades downstream of the turbine vanes remains significantly non-uniform and that accurate prediction of the temperature distribution downstream of the vanes is critical for advanced turbine cooling design.

# Acknowledgments

I am grateful to the National Science Foundation, which supported me through a Graduate Research Fellowship. Financial support for the research presented in this thesis was provided by the Army Research Office (Agreement No.W911NF-11-1-0506) and the General Electric Corporation through the GE-Stanford University Strategic Alliance Program. The support of the Thermal Fluid Science Affiliates (TFSA) Program at Stanford University is also greatly appreciated.

Firstly, I'd like to thank my advisor, Prof. John Eaton, for all of his guidance and mentorship over the last five years. His constant support has been crucial to my growth as a researcher and throughout my PhD. His positive attitude and dedication to his students contributes to a wonderful work environment and a hugely collaborative lab group. I'd also like to thank the entire Eaton research group, both past and present, but in particular the MRV/MRC team: Chris Elkins, Mike Benson, Emin Issakhanian, Filippo Coletti, Julia Ling, Kevin Ryan, Andrew Banko, Daniel Borup, Sascha Burton, Pablo Vasquez-Guzman, John Schoech, John D'Atri, and Pedro Milani. The complete dedication of this team and the cheerful and upbeat attitudes that they have at all hours of the day and night have made the long hours that the experiments require into fun and productive times. The research presented in this thesis could not have been accomplished without the efforts of Dr. Chris Elkins. I'd especially like to thank Laura Campo, Julia Ling, and Kevin Ryan for their friendship and ability to both celebrate and commiserate the ups and downs of research. The

following people at Stanford University were indispensable for their efforts in ensuring that the MRV/MRC experimental program logistics were handled: Tom Finnigan and Manny Infante at Environmental Health and Safety, Anne Sawyer, Dr. Gary Glover, and Dr. Marc Alley at the Richard M. Lucas Center for Imaging, Lakhbir Johal in the Thermosciences Machine Shop, and Rika Bosmans, Rosa Fernandez, and Marlene Lomuljo-Bautista in Flow Physics and Computational Engineering and the Center for Turbulence Research.

There are too many people who've supported me in some way to thank each individually, but I'd particularly like to thank Rebecca Zarin Pass, Piyushee Jha, Holly Morris, Joyce Chai, Kimberly Won, and William Nguyen. Finally, I could not have done this at all without the endless support of my sister, Nadeeka, and parents, Kyoko and Poojitha.

# Nomenclature

$A_{\text{streamtube}}$	Streamtube local cross-sectional area
$B$	Background run signal magnitude
$\vec{B}_0$	Constant external magnetic field
$B_1$	Radiofrequency magnetic pulse
$\bar{C}$	Mean concentration
$c$	Concentration
$DNS$	Direct Numerical Simulation
$\Delta E$	Mean absolute difference
$k$	Specific heat ratio
$LES$	Large Eddy Simulation
$LDV$	Laser Doppler Velocimetry
$M$	Mach number
$M_c$	Convective Mach number
$MR$	Magnetic Resonance
$MRI$	Magnetic Resonance Imaging
$NMR$	Nuclear Magnetic Resonance
$P_{\text{norm}}$	Normalized perimeter
$P_{\text{streamtube}}$	Perimeter of streamtube
$PIV$	Particle Image Velocimetry
$PLIF$	Planar Laser Induced Fluorescence

$Pr_t$	Turbulent Prandtl number
$R$	Reference run signal magnitude
$\vec{r}$	Position of fluid element
$R^2$	Linear correlation coefficient
$RANS$	Reynolds Averaged Navier Stokes
$Re$	Reynolds number
$RF$	Recovery Factor
$S$	Standard run signal magnitude
$S$	Normalized curvilinear coordinate
$Sc_t$	Turbulent Schmidt number
$SLA$	Stereolithography
$SNR$	Signal-to-noise ratio
$TE$	Echo time
$Tu$	Turbulence intensity
$\bar{T}$	Mean temperature
$t$	Time
$u$	Velocity
$v$	Local velocity
$\vec{v}$	Velocity of fluid element
$venc$	Encoding velocity
$\alpha_t$	Turbulent scalar diffusivity
$\gamma$	Gyromagnetic ratio
$\mu_c$	Standard deviation of the MRC experimental uncertainty
$\mu_B$	Standard deviation in background run signal magnitude
$\mu_{MRV}$	Standard deviation of the MRV experimental uncertainty
$\mu_R$	Standard deviation in reference run signal magnitude
$\mu_S$	Standard deviation in standard run signal magnitude

$\Theta_o$	Total temperature ratio
$\theta$	Normalized temperature
$\Phi$	Phase of signal
$\omega_0$	Larmor frequency

# Contents

<b>Abstract</b>	<b>iv</b>
<b>Acknowledgments</b>	<b>vii</b>
<b>Nomenclature</b>	<b>ix</b>
<b>1 Introduction</b>	<b>1</b>
1.1 Three-dimensional Flows in Turbomachinery . . . . .	1
1.2 Film Cooling Schemes and Temperature Distribution Non-Uniformity	4
1.3 Motivation and General Objectives . . . . .	7
1.4 Magnetic Resonance Imaging as a Fluid Mechanics Analysis Tool . .	11
1.5 Specific Objectives and Organization of this Thesis . . . . .	12
<b>2 Magnetic Resonance Techniques</b>	<b>14</b>
2.1 Basic Principles of Magnetic Resonance Imaging . . . . .	15
2.2 Magnetic Resonance Velocimetry (MRV) . . . . .	16
2.2.1 Specific MRV Procedures . . . . .	22
2.2.2 MRV Uncertainty . . . . .	23
2.3 Magnetic Resonance Concentration (MRC) . . . . .	26
2.3.1 Specific MRC Procedures . . . . .	28
2.3.2 MRC Uncertainty . . . . .	32

2.4	Scalar Transport Analogy . . . . .	33
2.5	Compressibility Effects Experiment . . . . .	34
2.5.1	Experimental Test Facility . . . . .	36
2.5.2	Results . . . . .	44
2.5.3	Conclusions . . . . .	60
<b>3</b>	<b>Double Passage Vane Cascade Experimental Design</b>	<b>62</b>
3.1	Rotating, Infinite, and Linear Cascades . . . . .	62
3.2	Design of Double Passage Vane Cascade Geometry . . . . .	65
3.3	Design of Experimental Setup . . . . .	70
3.4	Flow loop for MRV . . . . .	75
3.5	Flow loop for MRC . . . . .	76
3.6	Limitations due to Magnetic Field . . . . .	82
<b>4</b>	<b>Results from Double Passage Experiments</b>	<b>83</b>
4.1	Development of the Passage Vortex . . . . .	83
4.2	Concentration field in the vane wake . . . . .	88
4.3	Summary . . . . .	104
<b>5</b>	<b>Hot Streaks Generator Experiments</b>	<b>106</b>
5.1	Introduction to Hot Streaks Experiments . . . . .	106
5.2	Experimental Apparatus and Parameters . . . . .	108
5.3	Magnetic Resonance-based Measurement Technique . . . . .	112
5.3.1	Magnetic Resonance Velocimetry . . . . .	112
5.3.2	Magnetic Resonance Concentration . . . . .	114
5.4	Results . . . . .	117
5.5	Summary . . . . .	137

<b>6</b>	<b>Conclusions and Recommendations</b>	<b>145</b>
6.1	Compressibility Effects Experiment . . . . .	145
6.2	Double Passage Vane Cascade Experiments . . . . .	147
6.2.1	Endwall vortex studies . . . . .	147
6.2.2	Coolant dispersion in the vane wake . . . . .	147
6.2.3	Hot streaks experiments . . . . .	149
<b>A</b>	<b>Coordinates for VKI vane</b>	<b>152</b>
<b>B</b>	<b>Double Passage Vane Cascade Wall Coordinates</b>	<b>162</b>
	<b>Bibliography</b>	<b>173</b>

# List of Tables

2.1	MRC scan types . . . . .	28
2.2	Key experimental parameters . . . . .	37
3.1	Key airfoil and trailing edge parameters . . . . .	73
5.1	Hot streaks concentration inlet conditions for peak concentration analysis	126
5.2	Hot streaks concentration inlet conditions for the low concentration data set . . . . .	128
5.3	Hot streaks concentration inlet conditions for the high concentration data set . . . . .	128

# List of Figures

1.1	Schematic of 1st stage in a high pressure turbine. . . . .	2
1.2	Three-dimensional flows in a turbine vane cascade. . . . .	5
2.1	Comparison between turbulent pipe flow velocity profiles extracted from LDA data ( $Re = 5400$ ) and MRV data ( $Re = 6400$ ). . . . .	19
2.2	Normalized MRV vectors in black and PIV vectors in gray are plotted for centerplane flow downstream of a backward facing step . . . . .	20
2.3	Comparison of region of interest for acquiring full-field double passage vane cascade data vs. wake-specific data. . . . .	22
2.4	Slice directions for 3D MR measurements . . . . .	24
2.5	Experimental setup for MRC and PLIF comparison. . . . .	28
2.6	MRC experimental validation using PLIF measurements. . . . .	29
2.7	Schematic of test channel. . . . .	38
2.8	Detail of cylinder and splitter plate geometry. . . . .	38
2.9	MRC experimental flow loop. . . . .	40
2.10	Schematic of stagnation temperature probe. . . . .	42
2.11	Orientation of extracted data. . . . .	47
2.12	Streamlines and velocity contours at spanwise centerplane ( $z = 0$ ). . .	47
2.13	Isosurfaces of vorticity, plotted at normalized vorticity levels of $\pm 0.5$ . . .	48

2.14	Streamwise RMS vorticity and velocity are calculated in the secondary flow at $x = 0$ mm. . . . .	48
2.15	Contours of streamwise velocity at $y = 5$ mm. . . . .	49
2.16	Spanwise vorticity contours plotted in the centerplane ( $z = 0$ ). . . . .	49
2.17	Contours of concentration at $z = 0$ mm. . . . .	51
2.18	60% isosurface of concentration. . . . .	52
2.19	Concentration contours in the $y$ - $z$ plane at $x = 38$ mm. . . . .	52
2.20	Energy separation effect: raw stagnation temperature profiles measured at $x = 19.4$ mm, $z = 10$ mm. . . . .	54
2.21	Normalized temperature profiles at $x = 19.4$ mm, $z = 10$ mm. . . . .	55
2.22	Normalized profile comparison: $x = 11.4$ mm, $x = 23.4$ mm, $x = 35.4$ mm, $x = 47.4$ mm, $x = 59.4$ mm, centerline ( $z = 0$ mm). . . . .	58
2.23	Normalized profile comparison: $x = 7.2$ mm, $x = 19.2$ mm, $x = 31.2$ mm, $x = 43.2$ mm, $x = 55.2$ mm, off-centerline( $z = 10$ mm). . . . .	58
3.1	Relationship between original engine geometry and double passage vane cascade experimental setup. . . . .	64
3.2	Setup of infinite cascade CFD simulation. . . . .	67
3.3	Pressure coefficient distribution of airfoil from FLUENT simulations . . . . .	69
3.4	Evolution of double passage vane cascade channel walls. . . . .	70
3.5	Schematic of double passage test channel. . . . .	72
3.6	Profile of VKI vane used in double passage vane cascade experiments. . . . .	72
3.7	Schematic of vane and pressure-side cutback cooling and feed system. . . . .	73
3.8	Detailed view of pressure side cutback cooling. . . . .	74
3.9	Schematic for flow loop for MRV. . . . .	76
3.10	3T1 Magnet Suite at Richard M. Lucas Center for Imaging, Stanford University. . . . .	77

3.11 Schematic for flow loop for “reference” runs. . . . .	78
3.12 Schematic for flow loop for “background” runs. . . . .	79
3.13 Schematic for flow loop for “inverted” runs. . . . .	80
3.14 Schematic for flow loop for “standard” runs. . . . .	81
4.1 Streamlines through the endwall vortex . . . . .	85
4.2 Contours of streamwise vorticity, normalized by bulk inlet velocity and vane chord . . . . .	87
4.3 Contours of streamwise vorticity in the wake region, normalized by bulk inlet velocity and vane chord . . . . .	89
4.4 Isosurface of 12% coolant concentration . . . . .	90
4.5 Slices of concentration contours showing spanwise variation of concen- tration in the vane wake . . . . .	91
4.6 Profiles of spanwise-averaged concentration showing variation of con- centration in the vane wake normal to the flow direction . . . . .	92
4.7 Concentration profiles are plotted against the spanwise direction for $x$ $= 90$ mm, $x = 100$ mm, $x = 110$ mm, $x = 120$ mm, and $x = 130$ mm	95
4.8 Streamtubes with contours of concentration at $x = 90, 100, 110, 120,$ $130$ mm . . . . .	96
4.9 Locations of streamtubes. . . . .	97
4.10 Evolution of perimeter of streamtube with streamwise position . . . . .	97
4.11 Peak, minimum and average concentration in the center and endwall streamtubes for $90 \text{ mm} < x < 130 \text{ mm}$ . . . . .	99
4.12 Concentration distribution in the small (3 mm-diameter) center and endwall streamtubes for $x=90$ mm, $100$ mm, $110$ mm, $120$ mm, and $130$ mm. . . . .	101
4.13 Concentration transport in center and endwall streamtubes . . . . .	103

4.14	Mean streamwise velocity in center and endwall streamtubes . . . . .	104
5.1	Schematic of test channel . . . . .	109
5.2	Schematic of hot streaks generator - injection airfoil and feed system	111
5.3	Spanwise centerplane slice of streamwise velocity contours with injector airfoil schematic for reference . . . . .	112
5.4	Spanwise centerplane slice of $V_x$ velocity contours comparing test sec- tion velocity fields with and without hot streak injectors . . . . .	113
5.5	Isosurfaces of 20% normalized concentration . . . . .	118
5.6	Isosurfaces of 10% concentration inside suction-side streamtube . . .	120
5.7	Isosurfaces of 10% concentration inside center region streamtube . . .	120
5.8	Isosurfaces of 10% concentration inside pressure-side streamtube . . .	121
5.9	Geometry of vane, streamlines, and extraction planes . . . . .	122
5.10	Normalized perimeter of streamtubes . . . . .	123
5.11	Streamtube cross-sectional area as a function of local streamwise velocity.	124
5.12	Mean streamwise velocity in each streamtube vs. $x$ -coordinate and normalized curvilinear coordinate . . . . .	125
5.13	Contours of concentration in suction side hot streak, in slices normal to the flow velocity at various $x$ -locations . . . . .	129
5.14	Contours of concentration in center hot streak, in slices normal to the flow velocity at various $x$ -locations . . . . .	130
5.15	Contours of concentration in pressure side hot streak, in slices normal to the flow velocity at various $x$ -locations . . . . .	131
5.16	Normalized peak concentration vs downstream location . . . . .	132
5.17	Locations of slices of contours of concentration plotted in Figures 5.18 and 5.21 . . . . .	132

5.18	Contours of concentration in the wake of the vane trailing edge at locations illustrated in Figure 5.17, high concentration data set . . . .	138
5.19	Contours of concentration in the wake of the vane trailing edge at Locations 1 and 4 as illustrated in Figure 5.17. . . . .	139
5.20	Profiles of concentration at spanwise locations $z = -6$ , $z = -3$ , $z = 0$ , $z = 3$ , $z = 6$ mm at downstream locations 2,4, and 6 from Figure 5.17, high concentration data set . . . . .	140
5.21	Contours of concentration in the wake of the vane trailing edge at locations illustrated in Figure 5.17, low concentration data set . . . .	141
5.22	Profiles of concentration at spanwise locations $z = -6$ , $z = -3$ , $z = 0$ , $z = 3$ , $z = 6$ mm at downstream locations 2,4, and 6 from Figure 5.17, low concentration data set . . . . .	142
5.23	Geometry of vane, streamlines, and extraction planes in the wake of the vane trailing edge . . . . .	143
5.24	Normalized concentration transport . . . . .	144

# Chapter 1

## Introduction

### 1.1 Three-dimensional Flows in Turbomachinery

*This chapter includes excerpts from a manuscript accepted to the 2014 ASME International Gas Turbine Institute Conference cited as Yapa SD, Elkins CJ, Eaton JK (2014). “Endwall vortex effects on turbulent dispersion of film coolant in a turbine vane cascade”. Proceedings of ASME Turbo Expo 2014 (GT2014-25484). Additional excerpts are from Yapa SD, D’Atri JL, Schoech JM, Elkins CJ, Eaton JK, 2014. “Comparison of Magnetic Resonance Concentration Measurements in Water to Temperature Measurements in Compressible Air Flows”. Exp Fluids 55(11), November, pp.1834-1 - 1843-14.*

The understanding and prediction of the highly three-dimensional flow and heat transfer in modern gas turbine engines is a problem that has not been solved over many years of turbomachinery research. Continuing demands for increased thrust and engine life and reduced fuel consumption and noise have driven engine design towards higher and higher peak cycle temperatures. This creates acute problems in the high pressure turbine stages where the nozzle vanes and rotor blades must endure extremely high heat loads.

Figure 1.1 shows a schematic of a typical first stage turbine in a modern propulsion

gas turbine. The stage consists of a set of stationary vanes to accelerate the flow leaving the combustor and an axial flow turbine to extract work from the high speed gas stream. The heat transfer aspects of the nozzle vanes are important for two reasons. First, cooling of the vanes is critical because they are exposed to the highest gas temperatures in the engine. Second, the outflow from the vane row determines the temperature distribution passing over the highly stressed turbine blades, dictating their cooling requirements.

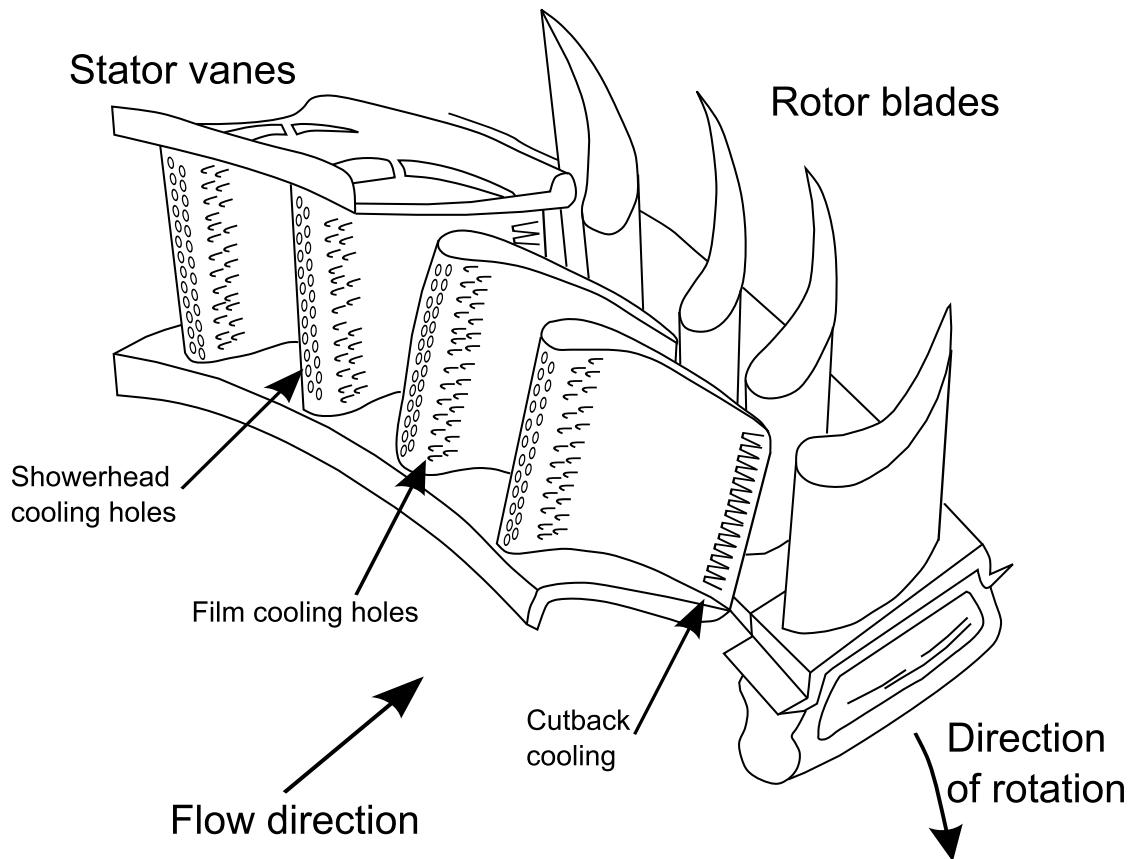


Figure 1.1: Schematic of 1st stage in a high pressure turbine. Mainstream flow is entering from the combustor from the left. The nozzle vanes are fixed into two concentric rings and serve to accelerate and turn the flow. The rotating blades turn the flow back in the opposite direction and extract work from the flow. They are fixed into a rotating disk using dovetail joints.

Turbine vanes are both internally and externally cooled to withstand the hot gas environment. The internal cooling consists of ribbed serpentine passages to convectively cool the vane metal. Regions of the vane exposed to the highest heat loads often have local internal impingement or pin fin arrays to further increase internal convective cooling. External film cooling is used to locally decrease the convective heat flux to the vane outer surface. The film cooling is generally fed by discrete holes on the vane surface, except for at the trailing edge which is cooled by slots that are cut into the pressure side of the vane.

Hot streaks from the combustor and cool streaks from the vane film cooling impose strong inlet temperature variations on the turbine blades, which can lead to local hot or cold spots, high thermal stresses, and fatigue failures. Furthermore, the complex three dimensional flows around the vane may act to concentrate cool or hot fluid exiting the vane row.

In order to optimize the cooling design of the turbine blades, the designer must be able to predict the temperature distribution entering the turbine rotor. Therefore, it is important to understand and predict how coolant streaks from the vane film cooling system are dispersed in the turbulent vane wake, and the mean distortion and turbulent dispersion of combustor hot streaks as they pass through the vane row. This requires flow simulation models that can capture the complex three dimensional flow features of the vane passage flow and accurately represent turbulent mixing both in the boundary layers and in the vane wake. This is beyond the state of the art of present day design methodology which is based on simulations using Reynolds Averaged Navier-Stokes (RANS) equations. RANS solvers require a model to represent turbulent mixing in order to calculate the temperature field. The most widely used models were developed for simple shear flows and tuned using flat plate boundary layer data. The three dimensional rotating flows found in gas turbine engines have anisotropic mixing and previous studies have shown that the mixing models can have

turbulent Prandtl and Schmidt numbers that are off by a factor of two or three. Because of this, the RANS solvers that most commercial Computational Fluid Dynamics (CFD) models use overpredict the effectiveness of the turbine film cooling schemes, causing the designs to grossly underperform during tests.

It is apparent that new data sets are needed that can be used to guide the development of and validate turbulent mixing models for use in turbine flows. Previous experiments have focused on the surface temperature or heat transfer coefficient on vanes and blades. While this information is directly relevant to turbine design, it does little to guide improved model development or to give physical insight into these flows. Experiments in simple boundary layers are not adequate because they miss the effects of the dominant three dimensional features in turbine flows. Experiments which provide full-field three component velocity data along with distributions of a passive scalar such as a non-reacting contaminant or temperature will be particularly useful. Ideally, the data would include direct measurements of the turbulent Reynolds stresses and scalar transport. However, as will be shown, considerable new understanding can be gained using full-field mean velocity and scalar measurements.

## **1.2 Film Cooling Schemes and Temperature Distribution Non-Uniformity**

Turbine vanes are made of proprietary high-temperature alloys. The maximum allowable temperature of these materials is generally around 1500°F to 2000 °F. Cooling air is bled from the compressor discharge and passes through holes and cutaway slots in the external surface of the component to create a layer of relatively cool air between the turbine vane and the hot mainstream gases. Engine efficiency is primarily limited by the turbine inlet temperature. Over the years since the introduction of

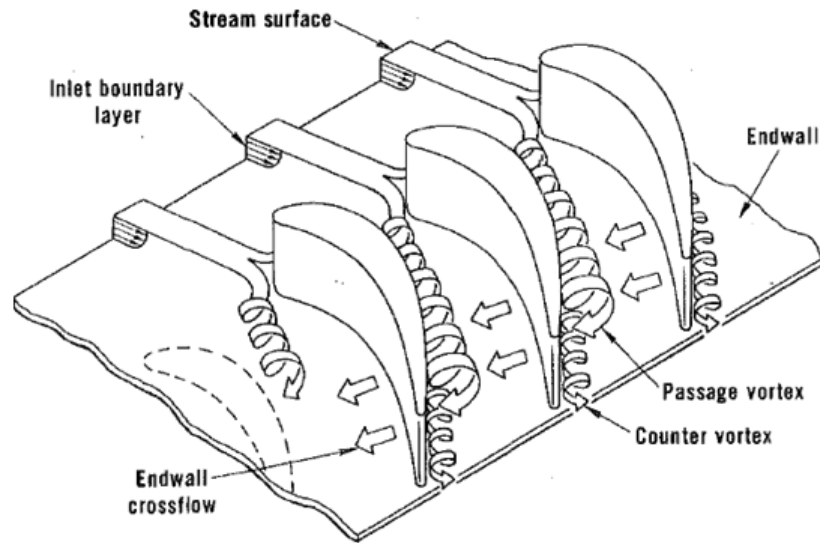


Figure 1.2: Three-dimensional flows in a turbine vane cascade. The endwall is the back plate to which the vanes attach. Mainstream flow is entering the field from the top left corner. Figure from Langston, L.S. *Cross Flows in a Turbine Cascade Passage* [36]

film cooling in gas turbine engines, turbine inlet temperatures have increased from  $1700^{\circ}\text{F}$  to over  $3000^{\circ}\text{F}$  [44]. This has been at the expense of increased diversion of compressor outlet flow for cooling.

Flow diverted for cooling is a loss to the thermodynamic cycle. As much as 30% of the airflow through the engine can be bled off to contribute to component film cooling, leading to a decrease in engine efficiency. Because of this, it has become imperative that effective film cooling schemes be developed to minimize film cooling flowrates while still achieving longer component lifetime by reducing the amount of thermal stress and fatigue experienced by the components. The performance of the cooling schemes of the turbine components can increase the part life, or a decision can be made to reduce the amount of cooling flow provided a longer part life is not needed (thereby increasing engine performance)[8]. While the coolant mixes quite

rapidly with the hot freestream flow, the three-dimensionality of the fluid mechanics in these complex geometries ensures anisotropic mixing. Additionally, the coolant is not completely mixed into the freestream by the time that it encounters the next stage of components such that temperature non-uniformities exist in the mainstream flow.

In general, a uniform turbine inlet temperature is assumed for turbine design, even though the gases coming in from the combustor to the high pressure turbine experience circumferential and radial temperature nonuniformities due to discrete fuel injection [16, 44, 49, 58]. These temperature non-uniformities, known as hot and cold streaks, in the turbine vane inlet conditions should be taken into consideration when designing the cooling features, since designers must account for the highest possible temperature that will be experienced, as well as areas of high temperature gradients. A high temperature gradient, while not affecting the local heat transfer coefficient, may cause a considerable change in the rate of heat transfer to and from the surface of the vane [48]. Additionally, the positioning of the hot streaks relative to the turbine vanes is important to determine what sort of effects the interaction of the hot streaks with the coolant have on the film cooling surface effectiveness of the turbine vane [27, 28].

The combination of the hot and cold streaks, along with the unmixed coolant from the turbine vanes, causes temperature non-uniformities in the wake of the turbine vane. Accurate prediction of where and with what strength these non-uniformities occur can help with the design of the turbine components downstream of the vane. Engine designers could then alter the positions of the film cooling holes, or determine if less cooling airflow is needed to sufficiently cool the downstream components. By better understanding the turbulent mixing of the flows, turbine designers can limit the amount of air bled from the compressor and achieve significant gains in engine efficiency.

### 1.3 Motivation and General Objectives

Currently, the turbine vane designers in industry use commercially available CFD programs to design film cooling schemes. Numerous studies have been conducted both experimentally and numerically on the performance of showerhead film cooling, discrete hole film cooling, and pressure-side cutback film cooling in effectively cooling the surface of the vane, but fewer studies have been done on the mixing of the film coolant with mainstream fluid in the wake of the vane. This is due to the difficulty of conventional experimental techniques in gathering meaningful data in the vane wake. The complex geometry of turbine vanes impedes optical access for experimental techniques such as particle image velocimetry (PIV), laser doppler anemometry (LDA) or laser doppler velocimetry (LDV), and the large amount of time and effort necessary to gather three-dimensional data at a high spatial resolution limits the effectiveness of these methods. Probe techniques such as hot wire anemometry or pitot probes suffer from access problems and can cause flow interference. The situation is even more difficult for temperature measurements. Thermocouple probes and rakes have limited spatial resolution, cause flow interference, and take large amounts of test time to amass three dimensional data sets. Surface temperature measurement methods including resistance temperature detectors (RTDs) and liquid crystals cannot provide off surface field measurements. Optical methods for temperature are limited to line-of-sight integration, so are unsuitable for acquiring three dimensional data.

Research into the behavior of flows downstream of vane trailing edges in a cascade has shown that the secondary flows are significant. Flow visualization studies such as those carried out by Sieverding and Van Den Bosche [55] have shown that complex three-dimensional flow exists in the endwall region (see Figure 1.2). As yet, an analytical model of the flow in the endwall region has not been derived, and the small number of parameters studied (or able to be studied) does not span all of the

possible influences affecting the flow [37]. Binder and Romey [7] conducted total pressure and laser velocity field measurements, using Kiel type pressure probes for the velocity measurements. Calculations of total pressure loss coefficients indicated significant mixing effects in the vane wake and the presence of strongly rotational flow. Sieverding et al. [56] found using total pressure and temperature probes and oil flow visualization that mixing is strong in the wake region closest to the trailing edge. The mixing slows far downstream of the trailing edge of turbine guide vanes with trailing edge pressure side cutback cooling slots. Sieverding and Van Den Bosche [55] also used flow visualization to corroborate the work of Langston et al. [37] and establish that a large vortex forms between the vane suction surface and the endwall and contributes greatly to the secondary flows in the wake of the trailing edge. This vortex is now known as the passage vortex, and is schematically illustrated by Figure 1.2.

It is interesting to note that while Sieverding et al. and Langston et al. agree on the existence of the passage vortex, they and many others dispute the mechanism that leads to its development. A sample of the previous literature shows the diversity of opinion on the vortex behavior. Sieverding and Van Den Bosche [55] determined from colored smoke visualization that the passage vortex results from the subjection of an endwall boundary layer to a transverse pressure gradient. Langston [36] and Langston et al. [37] used pressure probes to determine the broad-scale fluid mechanics in a linear turbine vane cascade. They concluded that the pressure-side leg of the horseshoe vortex becomes the passage vortex, and the suction-side leg becomes a counter vortex that interacts with the passage vortex in the vane-endwall corner. Sharma and Butler [54] concluded from numerical studies that the suction-side leg intertwined with the passage vortex, while Goldstein and Spores [22] found that the suction-side leg of the horseshoe vortex is a distinct vortex above the passage vortex. Kang and Thole [31] made LDV measurements in the endwall boundary layer and

found that the suction-side leg of the horseshoe vortex was attenuated by the passage vortex as the vortices moved downstream.

The reason for these discrepancies exists in the nature of the measurements. Probe measurements and conventional imaging techniques have low spatial resolution and require optical access (respectively), limiting the number of points or planes at which data can be collected. The behavior of the fluid in the intermediate locations is unknown and CFD models cannot be reliably validated using that data. Meaningful analytical models have not been formulated due to these restrictions as well.

An additional topic of interest is that of hot streak dispersion in a vane wake, mentioned in Section 1.2. Many experiments and simulations have been conducted to investigate the behavior of the hot streaks, but a coherent set of inlet temperature profiles does not exist due to the difficulty in extracting experimental data from rotating experiments and from real combustors [49]. Dorney et al. [16] reviewed both hot streak experiments and simulations and determined that the behavior of the hot streaks was highly three-dimensional and two-dimensional simulations cannot predict the experimental hot streak behavior. Jenkins et al. [28] studied hot streak dispersion interacting with a turbine vane with showerhead and pressure and suction side film cooling using thermocouple rakes. They found that hot streaks that impacted an adiabatic vane experienced significantly less dispersion because the vane boundary layers and wake reduced the mixing effects than those hot streaks that simply passed through a channel. Additionally, they found that moderate freestream turbulence levels ( $Tu = 3.5\%$ ) caused the hot streaks to experience less dispersion than under high turbulence conditions ( $Tu = 20\%$ ). The interaction of film coolant with the hot streak diminished the peak hot streak temperature downstream of the vane, but left significant temperature gradients in the vane wake.

Existing analysis methods are not capable of predicting the evolution of these streaks as they interact with the three dimensional fluid flow around the vane and

the turbulent vane wake. RANS models incorporate turbulent mixing models using gradient diffusion approximations and most models assume isotropic diffusivity with constant turbulent Schmidt and Prandtl numbers. Such models are adapted from flat plate boundary layer theory and are highly inaccurate in complex, three-dimensional flows. A typical value of turbulent Prandtl number implemented in a RANS solver is 0.85-0.9, but Buice and Eaton [10] measured a turbulent Prandtl number ( $Pr_t$ ) of 1.7 in a highly disturbed turbulent boundary layer. In experimental investigation of heat transfer in a three-dimensional boundary layer, Elkins [17] showed that the cross-flows in 3D flows heavily impact the value of turbulent Prandtl number, causing it to vary between values of  $Pr_t = 0.6-1.1$ , further demonstrating that the gradient diffusion models are insufficient approximations for predicting turbulent mixing and heat transfer. More accurate CFD techniques, such as large-eddy simulation (LES) or direct numerical simulation (DNS) use fewer inherent approximations, but the large increase in computation power needed over a comparable RANS computation is a limiting factor in their widespread applicability [8].

The problems that exist in the development of improved models for dispersion of temperature variations due to film cooling or hot streaks are due to a lack of appropriate data. Therefore, the general objectives of this thesis are to use modern measurement techniques to fill this gap. Data sets with 3D velocity and scalar concentration fields can now be acquired in complex flows using magnetic resonance imaging (MRI) techniques. The overall goal of this thesis is to use MRI techniques to provide detailed measurements needed to understand the three-dimensional non-uniformity in the temperature distributions that exist downstream of a realistic turbine vane row.

## 1.4 Magnetic Resonance Imaging as a Fluid Mechanics Analysis Tool

Although Suryan first discussed the technique of making phase-contrast velocimetry measurements using MRI techniques over 60 years ago [57], the use of magnetic resonance velocimetry (MRV) in the study of turbomachinery applications is a fairly recent development. In the 1990s, the scientific basis for measuring turbulent flow using MRI techniques was established by Gatenby and Gore [21] and over the last ten years, the MRV technique has been applied to internal cooling passages of turbine vanes and blades, (Elkins et al. [20] and Iaccarino and Elkins [25]), unstable diffusers in power plants (Lo et al. [41]), turbine blade film cooling (Benson et al. [6], Issakhanian et al. [26], Ling et al. [40], Coletti et al. [12], Yapa et al. [60]), swirling flows (Grundmann et al. [24]), and for high-performance heat exchangers (Coletti et al. [13]). The MRV experimental technique has been validated using high-fidelity numerical simulations such as LES by Cherry et al. [11] and DNS by Ohlsson et al. [45]. Established experimental techniques such as PIV have also been used to validate MRV measurements, with excellent agreement between the two techniques (Elkins et al. [19], Coletti et al. [12]).

Benson et al. [4] introduced the magnetic resonance concentration (MRC) technique. This method uses nuclear magnetic resonance (NMR) principles to measure the mixing of two flow streams by measuring the concentration of a marker molecule carried by one of the streams. The method produces a three-dimensional map of the marker molecule concentration. The MRC method has been applied to turbine blade and vane film cooling by utilizing the scalar transport analogy between heat and mass transport (Benson et al. [6], Issakhanian et al. [26], Ling et al. [40], Coletti et al. [12], Yapa et al. [60]). The theory behind the scalar transport analogy approach is detailed in Section 2.4.

The power of the MRV and MRC experimental technique is especially apparent when compared to traditional techniques for quantifying fluid flows. MRV/MRC acquires a three-dimensional time-averaged data set for both velocity and scalar mixing. Traditional velocity measurements include pitot probes, thermal anemometry (hot wire anemometry), and optical techniques such as PIV and LDV, to name a few. These techniques require physical or optical access to either a surface or the flow, which limits the complexity of the geometries that can be considered. Additionally, the point-by-point nature of thermal anemometry, LDV, and pressure probe measurements, and the two-dimensional nature of techniques like PIV make the gathering of a three-dimensional flow field, while technically possible, an arduous and time-intensive process [23].

Similarly, the acquisition of temperature data using thermocouple or infrared camera measurements, or concentration measurements using planar laser-induced fluorescence (PLIF) or gas tracers are limited in spatial resolution and by optical access requirements. MRV/MRC's three-dimensional nature presents a unique look at an arbitrarily complex given flow field by providing a wealth of information over a three-dimensional region of interest.

## **1.5 Specific Objectives and Organization of this Thesis**

This thesis is intended to provide three dimensional full-field data of the turbulent mixing behavior in the wake of a turbine vane or blade from pressure side cutback film cooling and from the hot streaks that exit the combustor due to the discrete fuel injectors. Experimental validation of the applicability of the MRV and MRC techniques are discussed, and arguments for the application of MRV and MRC to

these studies are presented.

Extensive literature reviews are conducted in three parts. In Chapter 2, the MRV and MRC experimental techniques are discussed in detail, as well as the scalar transport analogy by which concentration measurements of a passive scalar can be used to accurately predict heat transfer. Since MRV/MRC experiments use a working fluid of water and real gas turbine engines operate in transonic air conditions, an experiment was designed and tested to experimentally validate the applicability of using MRI to understand mixing in compressible air flows. This chapter presents a survey of the literature involving the use of the scalar transport analogy and previous experimental findings on compressibility effects.

Chapter 3 presents a literature review on linear vane cascade measurements, as well as previous work done in film cooling and studies on vane wake mixing. The inverse design process for a double passage vane cascade is documented, as well as design specifications and considerations for the experimental setup as a whole. Experimental results from the double passage vane cascade are presented in Chapter 4.3.

The effect of non-uniform inlet conditions on the scalar distribution downstream of the vane comprises Chapters 5. A review of the existing literature on hot streaks experiments and simulations is presented in Chapter 5, as well as modifications to the double passage vane cascade setup. This chapter shows experimental results and includes a discussion of the hot streaks experiments, followed by general conclusions from all three experiments in Chapter 6.2.3.

## Chapter 2

# Magnetic Resonance Techniques

*This chapter includes excerpts from a manuscript accepted to the 2014 ASME International Gas Turbine Institute Conference cited as Yapa SD, Elkins CJ, Eaton JK (2014). “Endwall vortex effects on turbulent dispersion of film coolant in a turbine vane cascade”. Proceedings of ASME Turbo Expo 2014 (GT2014-25484). Section 2.5 is a reformatted version of Yapa SD, D’Atri JL, Schoech JM, Elkins CJ, Eaton JK, 2014. “Comparison of Magnetic Resonance Concentration Measurements in Water to Temperature Measurements in Compressible Air Flows”. Exp Fluids 55(11), November, pp.1834-1 - 1843-14.*

This chapter explains the experimental techniques used in this thesis. This chapter will first walk through the basic principles of MRI imaging, then discuss the MRV experimental technique, specific MRV procedures, and sources and calculation of MRV uncertainty. The same treatment is given to the MRC experimental technique, procedure, and uncertainty. A discussion of using the scalar transport analogy for assessing thermal mixing is presented. Finally, a validation experiment for assessing the applicability of MRV/MRC measurements to compressible flow heat transfer analysis is presented and discussed.

MRI is based on nuclear magnetic resonance (NMR) measurement techniques. The high spatial resolution and non-invasive nature of the measurements have brought

it to the forefront of medical imaging, particularly in soft-tissue applications. Its application to turbulent flow and turbomachinery, as stated in the previous chapter, is relatively new (within the last 2 decades).

## 2.1 Basic Principles of Magnetic Resonance Imaging

The background on basic MR principles is drawn in large part from three sources: the first being course content from a graduate course at Stanford University, EE 369B: Medical Imaging II and its corresponding textbook by (content and textbook by Professor Nishimura [43]), the second being the paper that introduced MRV for turbulent flow applications by Elkins et al. [20] and the last being a PhD thesis by Ling [39] that helpfully details the specific processes used in the MRV and MRC experimental techniques.

At its core, NMR measurements use the properties of the atomic nuclei present to gather information about the material or object being imaged. MR-relevant nuclei in the object to be imaged are known as spins. In MRV and MRC applications (and most MR-applications), these nuclei are the hydrogen nuclei (one hydrogen nucleus is a single proton) in water molecules. The large magnet in an MRI setup creates a constant external magnetic field, commonly referenced as  $\vec{B}_0$ . The hydrogen nuclei orient themselves to be aligned in the same direction as  $\vec{B}_0$ . This direction is conventionally defined as the  $z$ - or longitudinal direction and the spins precess around the  $z$ -axis with what is known as the Larmor frequency,  $\omega_0$ , with the Larmor frequency defined as seen in Equation 2.1:

$$\omega_0 = \gamma \vec{B}_0 \tag{2.1}$$

where  $\gamma$  is the gyromagnetic ratio, specific to the atom being imaged. A radiofrequency (RF) magnetic pulse is applied in the  $x$ - $y$  plane, which tips the spins away from their equilibrium position (aligned with the  $z$ -axis). A set of RF pulses of various frequencies are used to excite a slab of finite thickness in the volume being imaged. These RF pulses, named  $B_1$ , can have varying strengths and lengths of application, controlling how far away from the  $z$ -axis the net magnetization vector is tipped. After the RF pulse is turned off, the net magnetization vector realigns with the  $z$ -axis by precessing around the longitudinal axis at the Larmor frequency. An RF coil specially outfitted to process the electromagnetic signal generated by the rotating magnetization vector can then be used to gather the MR signal. At each measurement, information is gathered in the spatial frequency domain (commonly referred to as  $k$ -space). Varying the magnetic field gradients in space will determine the locations of the spins (the strength of the magnetization vector correlates to spatial location), and entire two- or three-dimensional MR images can be built up by repeating the measurement process over the entire region of interest. This process is known as the pulse sequence.

## 2.2 Magnetic Resonance Velocimetry (MRV)

MRV as implemented in the present work provides a fully three dimensional, three component velocity field at a spatial resolution as high as 0.5 mm x 0.78 mm x 0.5 mm in an approximately 150mm x 150mm x 250mm maximum volume. The phase contrast pulse sequence developed by Markl et al. is applied to this work [42, 20]. This method was previously used in-vivo to image laminar flows in living organisms [18]. It was first applied to complex turbulent flows in 2003 by Elkins et al. [20], who published the first experimental results on using MRV to study turbulent flows in turbomachinery applications. They studied fully turbulent flows in a serpentine

cooling passage. Phase-contrast MRV measures velocity by encoding the phase of the spin of the hydrogen proton using bipolar gradients. Linear combinations of the orientations of these gradients are used to determine the velocity of the flow. Additionally, the plastic of the channel can be differentiated from the fluid based on the signal magnitude since the water has a much higher density of protons.

Pelc et al [47] and Markl et al. [42] developed the 4D phase-contrast MRI first as a tool for the diagnosis and treatment of cardiac disease. This is also detailed by following Equations 2-4 from Elkins et al. [20], which follow the process of using the phase contrast method by first separating the position of an element of fluid into two terms, as seen in Equation 2.2:

$$\vec{r}(t) = \vec{r}_0 + \vec{v} \cdot t \quad (2.2)$$

where these two terms represent the element's initial position,  $\vec{r}_0$  and the distance the element has moved from that initial position (a function of time and constant velocity).

$$\Phi(\vec{r}, t) = \Phi_0(\vec{r}_0, t_0) + \gamma \int_0^{TE} \vec{G} \bullet \vec{v} \cdot t \cdot dt \quad (2.3)$$

The phase of the signal is represented by Equation 2.3. In this equation,  $TE$  is the time over which the bipolar gradient  $\vec{G}$  is applied.  $\vec{G}$ , the bipolar gradient, is applied in two different directions in two separate acquisitions of phase data. The difference in phase between these two acquisitions is given in Equation 2.4 and is used to determine flow direction and velocity [18].

$$\Delta\Phi(\vec{r}, t) = \gamma \int_0^{TE} \vec{G} \bullet \vec{v} \cdot t \cdot dt \quad (2.4)$$

The 4D phase-contrast MRV sequence is executed by performing four flow encodes at each spatial frequency (detailed in Markl et al. [42] and Pelc et al. [47]). Each of these four flow encodes corresponds to a different orientation for the gradient field ( $\vec{G}$ ), leading to phase shifts in the signal in each of the velocity directions measured. These encodes are designed such that when the information from the four flow encodes is combined, the correct three-component velocities result [47]. This information is then transformed back to velocity information at each measurement location. Currently, MRV has only been rigorously validated for mean (time-averaged) flow. However, capabilities also exist for pulsatile flow.

Elkins et al. [20] compared MRV results to LDA measurements for pipe flow at similar fully turbulent Reynolds numbers. Figure 2.1 shows the comparison between velocity profiles extracted from LDA experiments at a Reynolds number of 5400 and velocity profiles from MRV results at multiple streamwise locations in a flow of  $Re = 6400$ . The comparison between the LDA and MRV results are well within the experimental uncertainty and indicate good agreement between the two methods. Similarly, Elkins et al. [19] evaluated the MRV method by comparing MRV results to PIV measurements of the flow in a square channel in the downstream region of a backward facing step. Figure 2.2 shows the comparison between MRV and PIV velocity vectors, where the MRV vectors are plotted in black and PIV vectors are plotted in gray. The point by point comparison shows excellent agreement between the two techniques. These two studies, in addition to many others, show that the MRV method is applicable and accurate for turbulent flow.

For the present work, MRV is performed in a GE 3.0 Tesla whole-body magnet in

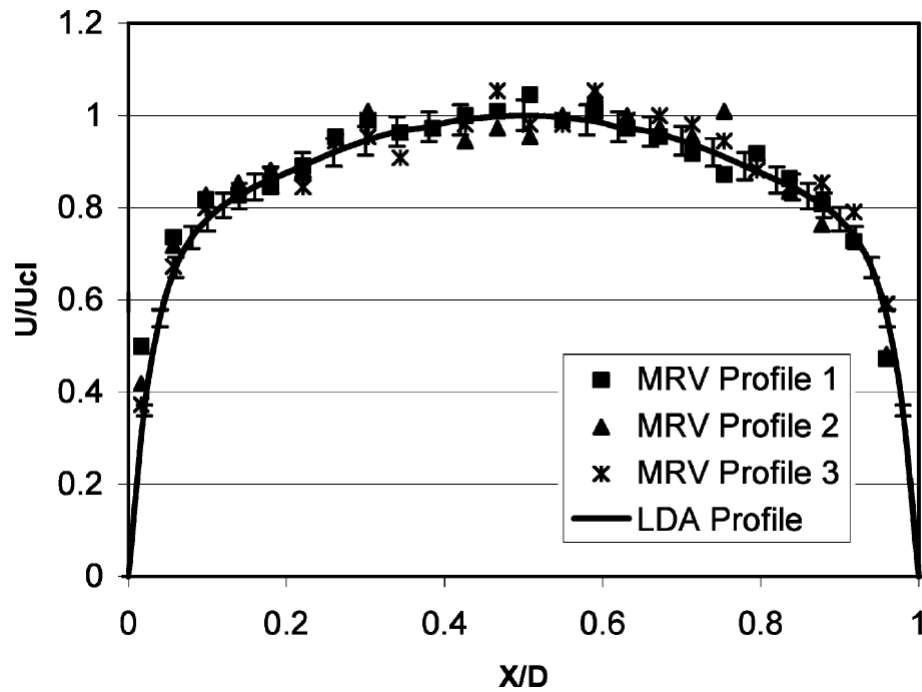


Figure 2.1: Comparison between turbulent pipe flow velocity profiles extracted from LDA data ( $Re = 5400$ ) and MRV data ( $Re = 6400$ ). The streamwise velocity normalized by the centerline velocity ( $U/U_{cl}$ ) is plotted on the y-axis, while the x-axis plots location within the tube, normalized by the tube diameter ( $X/D$ ). The centerline of the tube is located at  $X/D = 0.5$ . The MRV data are extracted from three streamwise locations. The MRV uncertainty is plotted with errorbars at  $\pm 3\%$ . The two methods are shown to have excellent agreement. Figure from Elkins et al. [20].

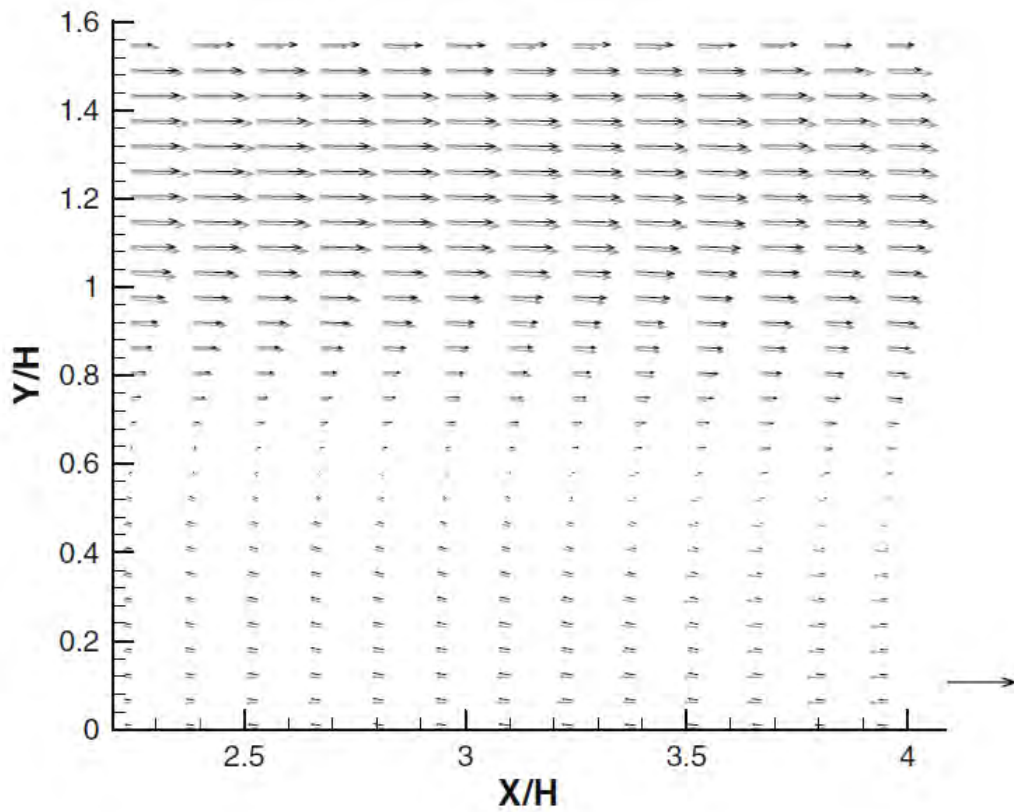


Figure 2.2: Normalized MRV vectors in black and PIV vectors in gray are plotted for centerplane flow downstream of a backward facing step. The vectors are normalized by  $U_{step}$ , the flow velocity at the step. The reference vector plotted is for a normalized velocity of 1.0. Both  $x$ - and  $y$ - coordinates are normalized by the step height,  $H$ . Excellent agreement is shown between the MRV and PIV results Figure from [19].

the Richard M. Lucas Center for Imaging at Stanford University. A transmit-receive RF head coil is used to improve spatial resolution and boost the signal-to-noise ratio (SNR). For certain scans in which the region of interest does not fit into the head coil, a cardiac coil is used instead of the head coil.

Scan times are limited by the amount of time it takes the spins to re-align to the  $\vec{B}_0$  field. This time, known as the relaxation time, can be reduced by adding a contrast agent to the water. In human subjects, gadolinium is used as a contrast agent (injected intravenously) to decrease scan times and increase signal. A working fluid of dilute (0.06M) copper sulfate solution in deaerated water is used as a contrast agent in the present MRV experiments.

For the compressibility effects experiments (Section 2.5), the data have a resolution of 0.6 mm x 0.6 mm x 0.8 mm in the streamwise ( $x$ ), splitter-plate wall-normal ( $y$ ), and spanwise directions ( $z$ ), respectively. In the double passage vane cascade experiments (Chapters 3-5), two different types of MRV data sets are acquired. These two data sets are referred to as full-field (low resolution) and wake-specific (high resolution) data sets. The full-field data sets cover the entire test section of the double passage vane cascade and have a resolution of 0.86mm x 0.9mm x 1.0mm in the inlet streamwise, inlet wall-normal, and spanwise directions, respectively. The low resolution data are acquired to get a full-field look at the velocity field, covering the sections both upstream and downstream of the vane. The high resolution data set is necessary to better resolve the wake and trailing edge region and has a resolution of 0.5mm x 0.78mm x 0.5mm in the inlet streamwise, inlet wall-normal, and spanwise directions, respectively. The difference in spatial locations imaged between the two data sets is shown in Figure 2.3.

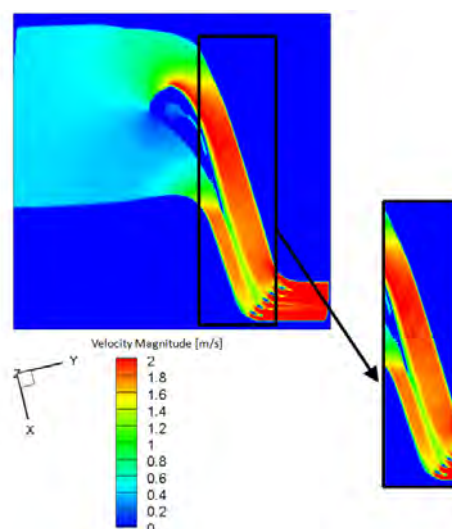


Figure 2.3: Comparison of region of interest for acquiring full-field double passage vane cascade data (left) vs. wake-specific data (right). Velocity magnitude data from the centerplane of the data are plotted for both data sets. The high resolution data set is focused on the wake and trailing edge.

### 2.2.1 Specific MRV Procedures

MRV data sets are compiled using two types of scans: “flow-on” and “flow-off” scans. A “flow-on” scan is one in which copper sulfate solution is recirculated through the system at prescribed flow rates. “Flow-off” scans are acquired when the pumps are turned off and the working fluid has been allowed to settle so that there is no fluid movement inside the test channel. During the data processing, the “flow-off” scans acquired on either side of a “flow-on” scan are averaged together, then subtracted from the “flow-on” scan of interest to perform a background subtraction. If there is any drift in the signal magnitude as the experiment progresses (magnet heats up with increasing number of scans, which can affect the baseline signal magnitude measured in a scan with no flowing liquid), then performing a background subtraction with “flow-off” scans that book-end the “flow-on” scan can serve to remove any bias.

Vencs (encoding velocities) are a parameter for MRV data acquisition and represent the maximum possible measured velocity. Vencs are set independently for each of the three velocity components. This parameter is similar to sampling frequencies in traditional experiments; if the maximum sampling frequency is too low, high frequency data will “wrap around” and be captured as low frequency data. Similarly, if the vencs are set too low for the measured velocity in a specific direction, areas of low velocity will show up unexpectedly. Fortunately, this is quite easy to see with preliminary measurements and the vencs can be adjusted accordingly. For the compressibility effects experiment, vencs of 300 cm/s ( $x$ -direction), 150 cm/s ( $y$ -direction), and 180 cm/s ( $z$ -direction) are used to acquire the data. In the double passage vane cascade experiments, the data are acquired using encoding velocities (vencs) of 270 cm/s (inlet streamwise direction), 250 cm/s (inlet wall-normal) and 60 cm/s (spanwise) for both high and low resolution data sets.

Other MRV parameters that are used are slice direction, bandwidth, and field of view. Slices can be taken in the coronal, sagittal, or axial directions, as illustrated in Figure 2.4. The frequency field of view is usually selected as the streamwise direction, and is set to 25.6cm in most scans. The bandwidth of the MRV measurements is 62.5 kHz, and the flip angle is  $15^\circ$ . The bandwidth determines how the signal is sampled and also helps to determine the signal-to-noise ratio. The flip angle is the angle by which the RF pulse ( $B_1$ ) excites the hydrogen nuclei.

### 2.2.2 MRV Uncertainty

The MRI experimental techniques have three main sources of error: 1) turbulent dephasing, 2) partial volume effects, and 3) noise. Turbulent dephasing occurs when turbulent flow causes the phase of the signal to be offset slightly and leads to a decrease in signal inside the channel. Partial volume effects occur when a voxel is situated on the boundary between the channel geometry and the fluid. The velocity

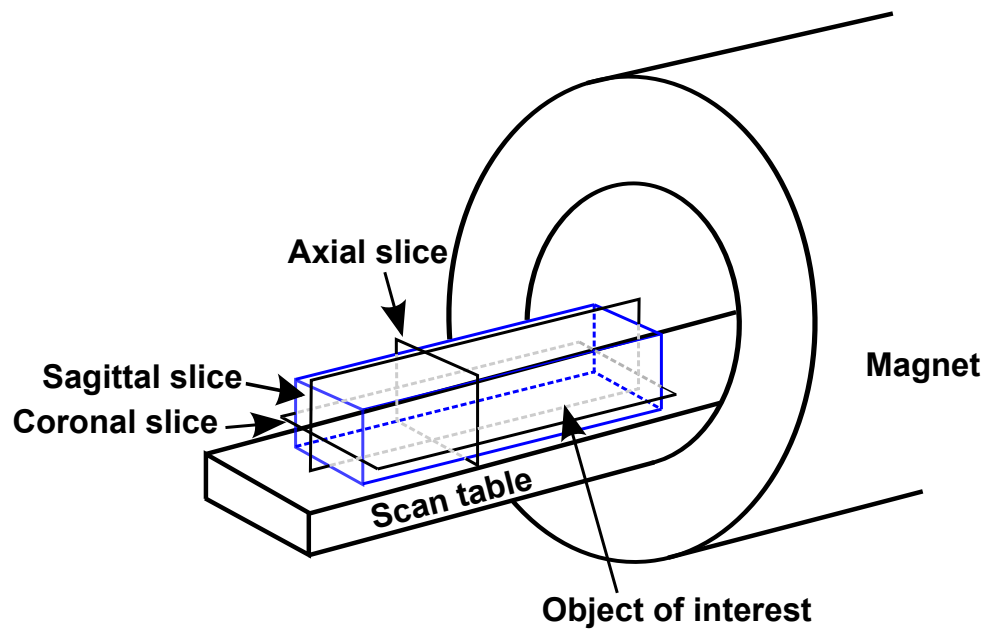


Figure 2.4: Slice directions for 3D MR measurements. These directions are coronal, sagittal, and axial. They are named using conventions from medical applications, and refer to the position of human body as it lies on the magnet table.

or concentration measurement appears to be smaller than it actually is in the fluid next to the wall, because part of the voxel is actually the plastic of the channel. The low signal magnitude in the plastic, when combined with flow or concentration signal over an entire voxel, creates an artificially low velocity or concentration measurement in the near-wall region. Noise is simply inherent in the measurements. The receiver coil's electrical resistance creates noise, as does the electromagnetic signal losses in the object being imaged. Similarly, the electronics of the MR system also produce noise [14].

The uncertainty in the MRV measurements is estimated using the techniques first explored by Conturo and Smith [14], Kaufman et al. [32], and Pelc et al. [46], and validated by Elkins et al. [20]. The uncertainty estimate is determined using Equation 2.5:

$$\mu_{MRV} = \frac{\sqrt{2}V_{enc}}{\pi SNR} \quad (2.5)$$

where  $\mu_{MRV}$  is the standard deviation of the experimental uncertainty,  $V_{enc}$  is the encoding velocity in the inlet streamwise direction, and  $SNR$  is the signal-to-noise ratio. The SNR is determined by dividing the mean signal magnitude in a flow region by the mean signal magnitude in an area of no flow. SNR depends heavily on the number of scans performed, increasing with an increasing number of scans.

Numerous comparisons between MRV and other techniques generally have validated the use of Equation 2.5. For example, Elkins et al. [19] and Coletti et al. [12] made detailed point-by-point comparisons between PIV and MRV and found that Equation 2.5 bounded the deviations. Ohlsson et al. [45] performed a well-resolved DNS of the separated flow studied by Cherry et al. [11] and found close agreement even with weak secondary flow features. Schiavazzi et al. [53] developed a numerical method to remove spurious divergence from three dimensional, three component

experimental data. The corrections required for typical MRV data sets were commensurate with MRC uncertainty estimates.

The SNRs for the individual measurements reported in Chapters 2, 4.3 and 5 vary depending on the specific flow features, the spatial resolution of the measurements, and the number of repeated scans. Therefore, specific uncertainty results are reported with the experimental results for each case.

## 2.3 Magnetic Resonance Concentration (MRC)

The MRC method was introduced in 2010 by Benson et al. [5]. In its simplest application, it is an effective way to measure the mixing between two flows in an arbitrarily complex geometry. In what is called a "standard" scan, working fluid of plain, deaerated water is set as the main flow, and working fluid of copper sulfate solution (the copper sulfate solution acts as a passive scalar) is introduced as a secondary flow. In an "inverted" scan, the roles are reversed, and the copper sulfate solution is set as the main flow and plain water is used as the secondary flow. These two scans are ultimately averaged together to remove any bias error in measurement.

The MRC technique provides a 3D concentration field quantitatively documenting the mixing of the secondary flow with the main flow, and it is relatively simple to provide a geometrically coordinated three-dimensional, three-component velocity field. MR-based experimental techniques are non-invasive and require no optical access, so it is possible to measure flow around arbitrarily complex geometries. Combining rapid prototyping techniques such as stereolithography (SLA) to build the test channels with the fast data acquisition period (one entire data set can be acquired in less than a day) enables a fast design/re-design process, allowing many different geometries to be tested in a short period of time. Furthermore, an idealized non-penetration boundary condition analogous to an adiabatic wall in thermal studies

can be implemented exactly.

MRC measurements are acquired using a custom 3D Fast Spoiled Gradient Echo (SPGR) sequence. The output from this sequence is signal intensity values formatted in a three-dimensional array [2, 5]. This pulse sequence is a modified version of the proprietary GE software furnished on the scanner. All MRC measurements are performed on a GE 3.0 Tesla whole-body magnet equipped with a transmit-receive RF head coil to improve spatial resolution and SNR.

Benson et al [5] used a two fluid plane mixing layer to validate MRC using Planar Laser Induced Fluorescence (PLIF) measurements. The same flow apparatus (Figure 2.5) was used in both types of experiments to allow for direct comparison. For these experiments, the two fluids used in the MRC were water and water with 0.8% gadolinium by volume. In the PLIF experiments, the two fluids used were water and water with Rhodamine Water Tracing (WT) dye at 150 parts per billion. Two types of experiments were performed for both the MRC and PLIF: “standard” and “inverted”. In a “standard” run, the MRC experiments had the gadolinium in the low speed flow, while the high speed flow had pure water, while in the PLIF experiments, the gadolinium was replaced with rhodamine dye. In an “inverted” run, the two flows were switched, such that the low speed flow was water, while the high speed flow contained either gadolinium or rhodamine dye. The comparison between the two experimental techniques is presented in Figure 2.6. Concentration profiles were extracted at multiple streamwise locations and plotted for both PLIF and MRC “standard” and “inverted” scans. Agreement is excellent among all of the data sets. There is a slight discrepancy between the MRC inverted scans and the rest of the data, but it has been hypothesized that this is due to turbulent dephasing and partial volume effects, which will be discussed later in this chapter.

Further validation of the MRC method has been done as part of this thesis using temperature probe measurements, and is detailed in Section 2.5.

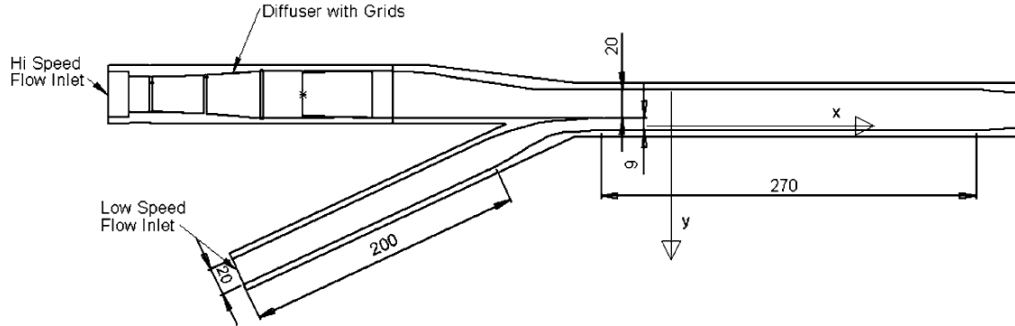


Figure 2.5: Experimental setup for MRC and PLIF comparison. The same setup was used in both the PLIF and MRC experiments, ensuring identical flow geometry between the two. In each of the experiments, water is injected as one flow, and water plus a passive scalar is used as the second flow. The mixing between the two flows can then be measured downstream of the splitter plate. Figure from Benson, et al. [5].

### 2.3.1 Specific MRC Procedures

For a complete MRC data set, four different scans are performed. These scans are known as “reference”, “background”, “standard”, and “inverted” runs. The “reference” and “background” runs are used for normalization of the data and background subtraction, respectively, while the “standard” and “inverted” runs contain scalar concentration maps of the mixing of the two flows.

Table 2.1: MRC scan types

Scan type	Number of scans	Description
Reference	$N_R$	Both coolant and main flows consist of copper sulfate
Background	$N_{B,I}, N_{B,S}$	Both coolant and main flows consist of deaerated water
Standard	$N_S$	Coolant flow is copper sulfate solution, main flow is deaerated water
Inverted	$N_I$	Coolant flow as deaerated water, secondary flow is copper sulfate solution

In a “standard” run, the main flow uses deaerated water as its working fluid, and

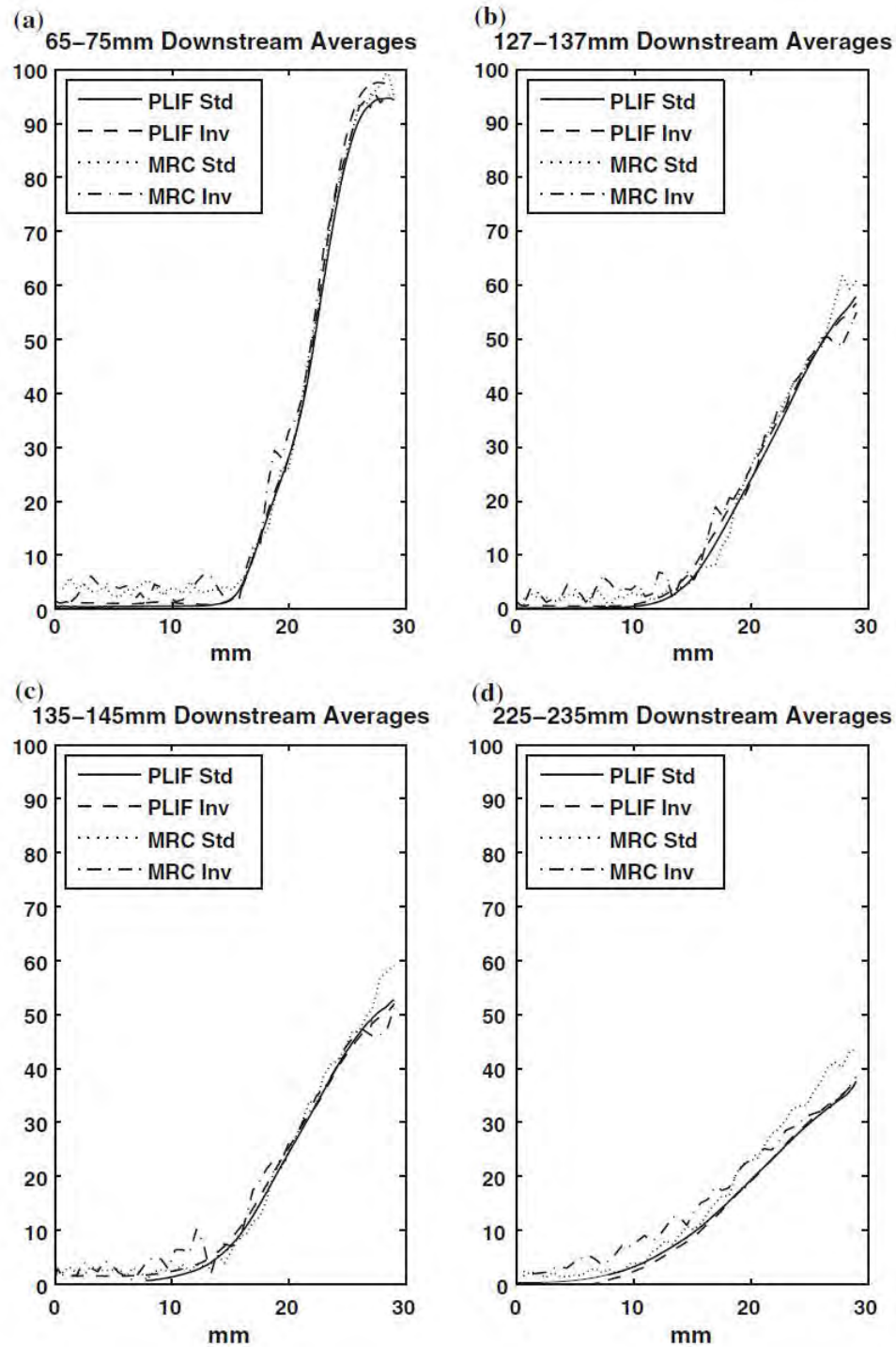


Figure 2.6: MRC experimental validation using PLIF measurements. Concentration profiles have been extracted and averaged over 10mm streamwise blocks at four different downstream locations. Figure from Benson, et al. [5].

the MRC technique measures the concentration of the copper sulfate as it mixes with the main flow. In most MRC experiments, a 0.015M copper sulfate solution is used as the secondary flow (also referred to as the coolant flow). This concentration of copper sulfate is used because a linear calibration curve between signal magnitude and copper sulfate concentration exists for up to a concentration of 0.015M. In an “inverted” run, the main flow uses 0.015M copper sulfate solution as its working fluid, and the secondary flow is deaerated water. A reference run uses 0.015M copper sulfate solution in both flows, while a background run uses deaerated water in both flows. These are detailed in Table 2.1.

Because the MRC output is in the form of signal magnitude, some data processing is necessary to get the data into a usable form. This process is laid out in Ling et al. [40] and Benson [2] and is paraphrased here.  $N_R$  “reference” runs,  $N_S$  “standard” runs, and  $N_I$  “inverted” runs are performed, scaled, and ensemble-averaged together, respectively.  $N_{B,I}$  “background” runs are performed for the “inverted” runs, and  $N_{B,S}$  “background” runs are performed for the “standard” runs. The “background” data for the “inverted” runs are ensemble-averaged and scaled so that areas of 0% concentration have the same magnitude as areas of 0% concentration in the “inverted” case. Similarly, the “background” data for the “standard” runs are ensemble-averaged and scaled to the “standard” case. This removes any drift in the signal magnitude as the magnet heats up over the course of the experiment. At this point, 5 data sets exist: the  $N_S$  “standard” runs ( $S$ ), the  $N_I$  “inverted” runs ( $I$ ), the scaled and averaged “background” data for “standard” ( $B_S$ ) and “inverted” ( $B_I$ ), and the scaled and ensemble-averaged “reference” data ( $R$ ). These data are in the form of three-dimensional arrays of signal magnitude values. To convert this information into an array of concentration values, the “reference”, “standard”, and “inverted” runs are first scaled to match the signal magnitudes in areas of 100% concentration to mean standard and inverted data sets. The standard and inverted data sets are normalized

using the following equations:

$$C_S = \frac{S - B_S}{R - B} \quad (2.6)$$

$$C_I = 1 - \frac{I - B_I}{R - B} \quad (2.7)$$

The “standard” and “inverted” concentrations are represented as  $C_S$  and  $C_I$ . The “standard” and “inverted” concentration runs are ensemble-averaged together to get one final data set of concentration,  $C$ , normalized to be between 0% and 100%.

The number of scans,  $N_S$ ,  $N_I$ ,  $N_{B,I}$ ,  $N_{B,S}$ , and  $N_R$  are determined by a separate calibration process in which it is determined how many scans are needed to achieve the target SNR (SNR increases with an increasing number of scans). Additionally, the number of scans is limited by the amount of main flow contamination that can be sustained to achieve good data quality. Calibration of the MRC technique is performed by performing reference runs with various concentrations of copper sulfate solution. In each of these runs, the signal magnitude is calibrated against the known copper sulfate concentration, and a nearly linear fit is found for the range 0 to 0.015M copper sulfate solution. Because of this linear fit, 0.015M copper sulfate solution is used and is regarded as 100% concentration in the “standard” runs.

A separate “high concentration” experimental technique has been developed for the double passage vane cascade experiments, which focus on turbulent mixing of film coolant in the far-wake of a turbine vane cooled by pressure side cutback cooling. The high concentration data set uses a 0.08M copper sulfate solution as the coolant fluid. The purpose of this technique is to get an in-detail look at the mixing behavior in the far-wake of the airfoil. In a regular MRC experiment, the 0.015M copper sulfate would have mixed out by the measurement region of interest such that the signal magnitude would be too weak to provide accurate analysis. By using the 0.08M copper sulfate

solution, the concentration of the copper sulfate will fall in the linear region of the calibration curve in the wake of the vane. “Inverted” runs are not performed for the high concentration technique, as placing 0.08M copper sulfate solution in the main flow will saturate the MR signal and yield incorrect measurements. In the data processing, the “inverted” data do not exist, and “reference” runs are still conducted with 0.015M copper sulfate solution. The final concentration results are scaled by a factor of 0.015M/0.08M since the desired result is the concentration at a given position relative to the injection concentration. This procedure substantially reduces the uncertainty by increasing the SNR in the region of interest.

MRC scan parameters include flip angle and bandwidth. These are set to be a flip angle of 55° and a bandwidth of 31.25 kHz.

### 2.3.2 MRC Uncertainty

The uncertainty for the MRC measurements is determined by first calculating the variances for each of the four scan types (“Standard”, “Inverted”, “Reference”, and “Background”) in the vane wake using a 95% confidence interval from a Student *t*-distribution. These uncertainties are combined as in Equation 2.8 to find the total uncertainty for the point-by-point concentration measurements using the root-sum of squares technique, presented in Benson [2] and Ling et al. [40].

$$\mu_c = \sqrt{\left(\mu_S \frac{\partial c}{\partial S}\right)^2 + \left(\mu_I \frac{\partial c}{\partial I}\right)^2 + \left(\mu_B \frac{\partial c}{\partial B}\right)^2 + \left(\mu_R \frac{\partial c}{\partial R}\right)^2} \quad (2.8)$$

Uncertainties in the MR measurements result from the total scan time (the period of time over which the flow is averaged), partial volume effects, and turbulent flow, which causes the SNR to decrease. Benson et al. [5] determined that the MRC and PLIF experiments agreed to within 5%, except for the near-wall region, where the experiments agreed to within 7%.

## 2.4 Scalar Transport Analogy

MRC implemented in this thesis measures the concentration of copper sulfate, which enters the flow in one of two flow streams. At the present concentration levels, the copper sulfate does not affect the fluid properties so may be considered a scalar contaminant. For the actual application, the quantity of interest is the temperature field. This is directly related to the concentration field using the scalar transport analogy. The three-dimensional thermal energy transport equation for turbulent convection is given in Equation 2.9. Assuming that the molecular thermal diffusivity ( $\alpha$ ) is overwhelmed by the turbulent thermal diffusivity and that the turbulent diffusivity is isotropic, Equation 2.9 can be simplified to Equation 2.10.

$$\bar{u} \frac{\partial \bar{T}}{\partial x} + \bar{v} \frac{\partial \bar{T}}{\partial y} + \bar{w} \frac{\partial \bar{T}}{\partial z} = (\alpha + \alpha_{tx}) \frac{\partial^2 \bar{T}}{\partial x^2} + (\alpha + \alpha_{ty}) \frac{\partial^2 \bar{T}}{\partial y^2} + (\alpha + \alpha_{tz}) \frac{\partial^2 \bar{T}}{\partial z^2} \quad (2.9)$$

$$\bar{u} \frac{\partial \bar{T}}{\partial x} + \bar{v} \frac{\partial \bar{T}}{\partial y} + \bar{w} \frac{\partial \bar{T}}{\partial z} = \alpha_t \left( \frac{\partial^2 \bar{T}}{\partial x^2} + \frac{\partial^2 \bar{T}}{\partial y^2} + \frac{\partial^2 \bar{T}}{\partial z^2} \right) \quad (2.10)$$

An analogous transport equation can be derived for a trace chemical carried by the fluid with concentration  $C(x, y, z)$  as shown in Equation 2.11. Assuming that neither heat nor chemical concentration affects the velocity field, then both are scalar contaminants and they would have the same turbulent diffusivity.<sup>1</sup>

$$\bar{u} \frac{\partial \bar{C}}{\partial x} + \bar{v} \frac{\partial \bar{C}}{\partial y} + \bar{w} \frac{\partial \bar{C}}{\partial z} = \alpha_t \left( \frac{\partial^2 \bar{C}}{\partial x^2} + \frac{\partial^2 \bar{C}}{\partial y^2} + \frac{\partial^2 \bar{C}}{\partial z^2} \right) \quad (2.11)$$

Under these assumptions, the transport equations for temperature ( $T$ ) and concentration ( $C$ ) are identical and if the dimensionless boundary conditions are identical,

---

<sup>1</sup>At a low but still turbulent Reynolds number, there might be a weak effect of the molecular Schmidt number on turbulent diffusivity. This effect is insignificant in fully turbulent flows.

they will have the same solution. This is known as the scalar transport analogy, and it is widely used for heat transfer measurements [22] in which mass flux is analagous to heat flux. In principle then, MRI measurements can be used to quantitatively determine the temperature distribution for thermal mixing problems.

## 2.5 Compressibility Effects Experiment

There are many advantages to the MRV/MRC experimental technique over traditional experimental fluid mechanics measurements, such as PIV, laser doppler velocimetry (LDV), and planar laser-induced fluorescence (PLIF). The MRC technique provides a 3D concentration field, and it is relatively simple to provide a geometrically coordinated 3D, 3-component velocity field. MR-based experimental techniques are non-invasive and require no optical access, so it is possible to measure flow around arbitrarily complex geometries. Combining rapid prototyping techniques such as stereolithography (SLA) to build the test channels with the fast data acquisition period (one entire data set can be acquired in less than a day) enables a fast design/re-design process, allowing many different geometries to be tested in a short period of time. Furthermore, an idealized no-penetration boundary condition analagous to an adiabatic wall in thermal studies can be implemented exactly.

Some limitations do exist for MRV/MRC. Currently, the technique is limited to a working fluid of water. This allows for a limited range of Reynolds numbers that can be studied. To date, the model sizes are limited to tens of centimeters, with flow velocities of a few meters per second. The Prandtl and Schmidt numbers of the working fluid are also confined to a narrow range. Additionally, only mean velocity and concentration fields can be measured accurately at this time. Reynolds normal stresses can be measured with limited accuracy, but full turbulence statistics and instantaneous data are not available. The biggest criticism, however, comes from

those who argue that the compressibility effects present in high speed gas flows are not present in water experiments. Thus, the applicability of the conclusions from MRV/MRC analysis of a given flow to a compressible environment is in question.

Previous studies on compressibility effects in turbulent flows have used simple geometries, such as the plane mixing layer studied in Brown and Roshko [9]. Dellimore et al. [15] determined that compressibility effects influence the fluid mechanics and heat transfer only when the convective Mach number ( $M_c = (u_\infty - u_{secondary}) / (a_\infty + a_{secondary})$ ) is higher than 0.3 and the total temperature ratio ( $\Theta_0 = T_{0,secondary} / T_{0,\infty}$ ) is lower than 0.6. In these relationships,  $u_\infty$  is the freestream velocity,  $u_{secondary}$  is the secondary flow velocity,  $a_\infty$  is the speed of sound in the freestream,  $a_{secondary}$  is the speed of sound in the secondary flow,  $T_{0,secondary}$  is the secondary flow stagnation temperature, and  $T_{0,\infty}$  is the freestream flow stagnation temperature. These studies corroborate the work of Repukhov [50], which found that compressibility effects do not significantly affect film cooling performance in turbomachinery.

The goals of this study were to 1) test the applicability of the MRC experimental technique to model high Reynolds number compressible applications, 2) investigate the robustness of the scalar transport analogy and 3) determine if MRC results can be applied quantitatively to determine the temperature field in high subsonic Mach number flows. A three-dimensional mixing experiment in the wake of a thick splitter plate was conducted. MRV/MRC measurements were taken in a working fluid of water, while temperature profiles were measured in an airflow of  $M_\infty = 0.7$  using a stagnation temperature probe in a test section of identical geometry. In the water experiments, a secondary flow with a passive scalar was mixed with a mainstream flow of water, and concentration profiles were extracted. These concentration profiles were then compared with normalized stagnation temperature profiles taken of a heated secondary flow of air mixing with a room-temperature mainstream flow. The relatively complex geometry was chosen to capture some of the important features of

practical mixing flows including a highly turbulent stream and reversed flow behind the blunt splitter plate.

Shock waves have a strong effect on the mean flow structure and their effects cannot be replicated in an incompressible liquid. Therefore, measurements of scalar transport in water cannot be used to infer mixing rates for gas flows where shock waves are present. Many high speed flows of practical interest are designed specifically to avoid shock waves which can cause unacceptable losses and high heat transfer rates. Therefore, there are numerous applications where water flow experiments could be used if the scalar transport analogy proves to be adequate.

### 2.5.1 Experimental Test Facility

Two identical experimental configurations were built into a portable, magnetic resonance compatible test channel illustrated in Figures 2.7, 2.8 and 2.9. Metered flow is delivered to the apparatus through a 38 mm diameter hose. Two successive diffusing sections expand to a 102 mm square cross-section. In the flow development section, fluid is directed through a series of grids and a honeycomb to improve flow uniformity. A 10.4:1 area ratio contraction feeds into the 25 mm x 40 mm mainstream flow inlet. A 6 mm thick splitter plate with a series of five 0.8 mm high boundary layer trips on the mainstream flow side divides the mainstream from the secondary flow. The boundary layer trips serve to create a thick, fully turbulent boundary layer on the mainstream flow side of the splitter plate. In the high subsonic Mach number air experiments, this boundary layer would be turbulent without the trips because the Reynolds number is quite high. However, the Reynolds number is considerably lower in the water experiments and an untripped boundary layer would have been transitional. The trips ensure that the boundary layer is fully turbulent and reduce the sensitivity of the boundary layer thickness to Reynolds number.

The outlet section of the air apparatus is enlarged compared to the MRV/MRC

experiments in order to prevent choking and reduce back pressure. The test section is adapted from a 38 mm diameter fitting to a 51 mm diameter flexible hose, which is then exhausted to the atmosphere via a 152 mm diameter hose. In comparison, the water rig exhausts from the test section to a 38 mm diameter hose, which recirculates to the water supply tank.

The secondary flow is introduced from a separate supply system via a 25 mm diameter hose. The flow passes through an array of five rows of cylinders as the flow passage adapts into a 6 mm x 40 mm cross-section, detailed in Figure 2.8. The cylinder array was carefully designed to prevent choking of the secondary flow in the air experiments while introducing three-dimensional turbulence into the secondary flow and helping distribute the flow across the full span of the test section. The diameters and spacings of the cylinder were chosen to minimize mean flow distortion at the secondary flow exit. The secondary flow area also contracts by a factor of 2.05 from the inlet tube to the rectangular slot exit. The thick splitter plate also was chosen to prevent heat conduction in the air experiments from the warm secondary flow to the cooler mainstream. The specifics of the water and air experiments are detailed in later in this section.

Table 2.2: Key experimental parameters

PARAMETER	MRV/MRC	Air (high subsonic Mach number)
Main flow Mach #	0	0.7
Secondary flow Mach #	0	0.56
Blowing ratio	0.8	0.8
Mainstream Re	12,000	86,000
Main flow velocity	2 m/s	232 m/s
Main flow fluid	Deaerated water	Air at $T_0 = 300K$
Secondary flow scalar	Copper sulfate solution	Air at $T_0 = 320K$

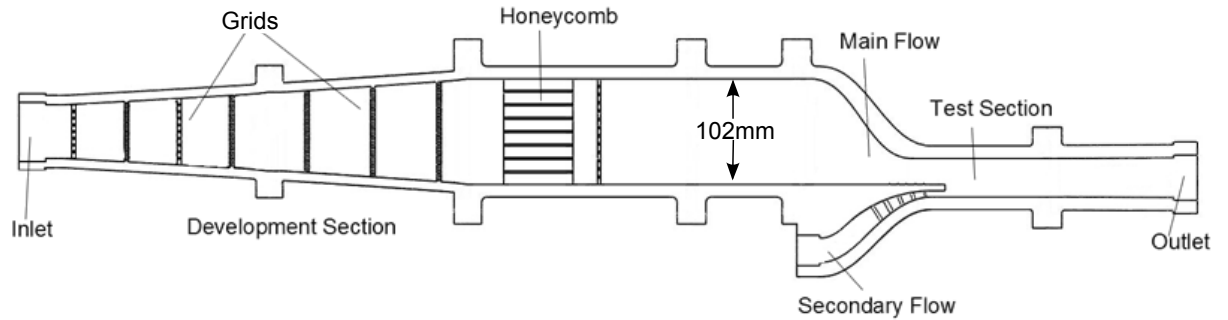


Figure 2.7: Schematic of test channel. A series of diffusers with grids conditions the mainstream flow before it passes into the contracting nozzle. The secondary flow passes from a 1-inch diameter hose through an array of cylinders. This cylinder array is shown in detail in Figure 2.8.

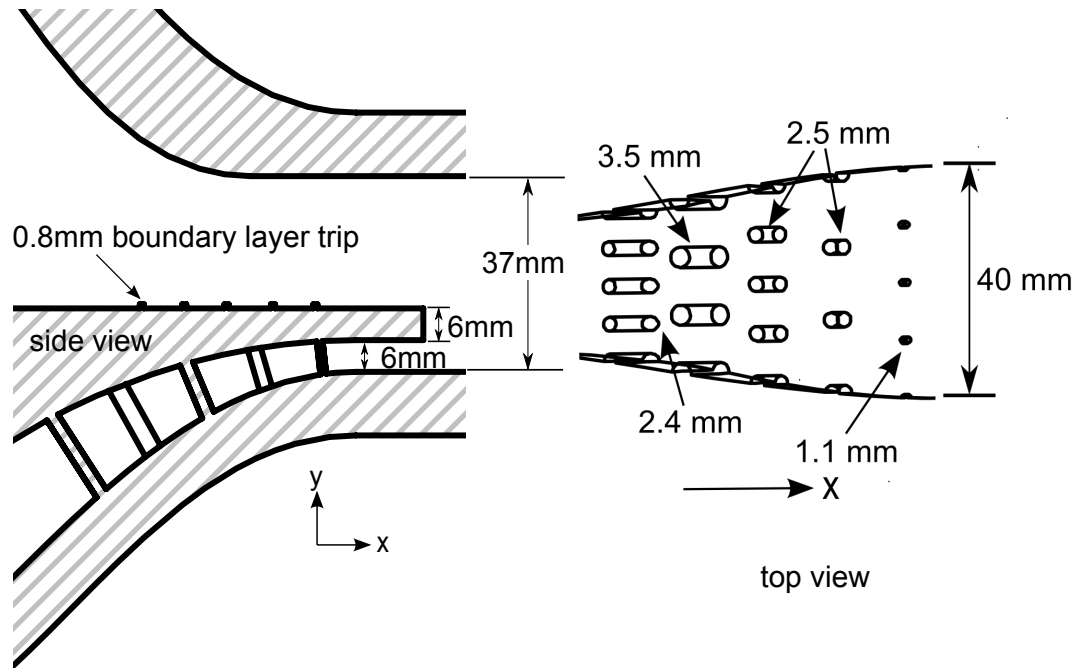


Figure 2.8: Detail of cylinder and splitter plate geometry. Five rows of pin fins serve to both reduce any inflow effects and introduce three-dimensionality into the secondary flow. Diameters for different rows of pin fins are indicated. The top view of the cylinder array is a cross-section taken inside the secondary flow inlet, and the top wall of the channel and the splitter plate have been removed for ease of viewing.

### MRV and MRC Measurements in Water Flow

The MRV and MRC experiments are acquired in a water channel setup as illustrated in Figure 2.9, with the test section placed in a GE 3.0T wholebody MRI scanner with a transmit-receive head coil. The experiment was designed to run at a main flow rate of 120 LPM of water. The main flow Reynolds number based on the thickness of the splitter plate is 12,000. The secondary flowrate is 23 LPM. At the trailing edge of the splitter plate, the bulk mainstream velocity is 1.7 m/s, while the bulk secondary flow velocity is 1.4 m/s, giving a blowing ratio of 0.8. The blowing ratio is traditionally defined in wall-jet flows as the ratio of the secondary momentum flux to the bulk momentum flux, but since the densities of the fluids are the same, the blowing ratio can be defined as the ratio of the bulk average velocity of the secondary flow to the bulk average velocity of the mainstream flow at the trailing edge of the splitter plate. Other important experimental parameters are given in Table 2.2. Flowmeters for the mainstream and secondary supply were continuously monitored and controlled to be within 3% of the nominal flow rate.

MRV uses phase-contrast magnetic resonance velocimetry principles to capture the 3D, 3-component mean velocity field inside the water channel using the experimental technique developed by Pelc et al. [46] and adapted to turbulent flows by Elkins et al. [20]. The present data have a resolution of 0.6 mm x 0.6 mm x 0.8 mm in the streamwise ( $x$ ), splitter-plate wall-normal ( $y$ ), and spanwise directions ( $z$ ), respectively. Vencs (encoding velocities) of 300 cm/s ( $x$ -direction), 150 cm/s ( $y$ -direction), and 180 cm/s ( $z$ -direction) are used to acquire the data. A dilute (0.06 M) copper sulfate solution in deaerated water is used as a working fluid. Each scan requires 7 minutes and 45 seconds. The MRV data set consists of six “flow-off” and five “flow-on” scans, where a “flow-on” scan refers to scans in which the pumps recirculate the working fluid through the main and secondary flows at the desired flow rates and the “flow-off” scans are those in which there is no fluid movement inside the

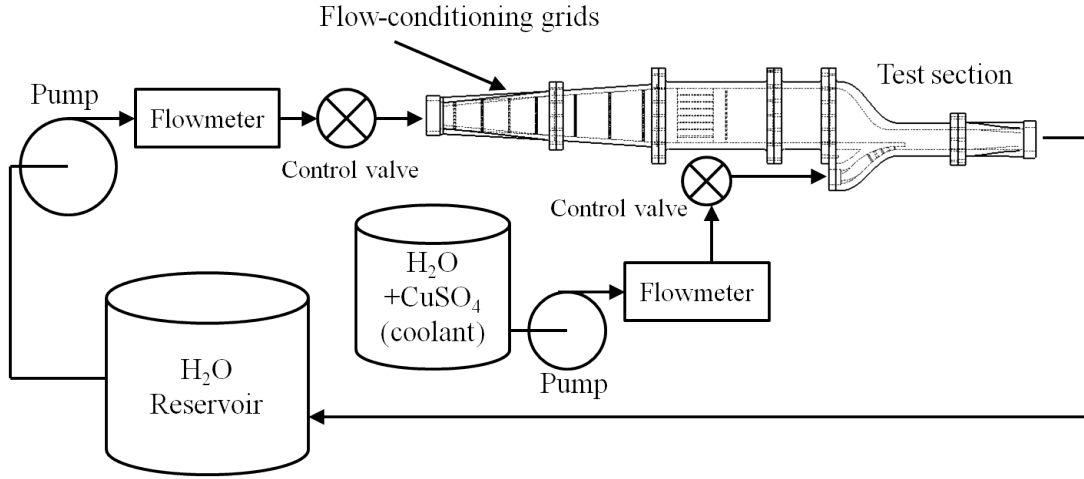


Figure 2.9: MRC experimental flow loop. A pump-flowmeter system recirculates the working fluid at 120 LPM as the main flow, while a separate pump-flowmeter system maintains a flowrate of 23 LPM as secondary flow. The test section is placed inside a transmit-receive head coil inside an MRI scanner for data acquisition.

channel. Each “flow-on” scan is taken between two “flow-off” scans. During the data processing, the “flow-off” scans acquired on either side are averaged together, then subtracted from the “flow-on” scan of interest to perform a background subtraction. The background-subtracted “flow-on” scans are then averaged together to get one final data set. The estimated uncertainty in the MRV measurement is calculated using Equation 2.5. The measured SNR of 14.7 led to value of 5.0% uncertainty when normalized by the local main velocity at the splitter plate lip in the streamwise direction.

The MRC experimental technique was developed by Benson et al.[5, 4, 6]. This technique is able to measure the three-dimensional concentration distribution of a passive scalar dissolved in one of the inlet flow streams. Measurements are acquired on a Cartesian grid of 3D volume elements (voxels). The main flow is pure deaerated water while the secondary flow is a dilute solution of copper sulfate in deaerated water. The MRC technique measures the concentration of the copper sulfate as it

mixes with the main flow. A 0.018 M copper sulfate solution was used because a linear calibration curve between signal magnitude and copper sulfate concentration can be obtained for concentrations up to 0.018 M. This concentration of copper sulfate has negligible effect on water density and viscosity.

As detailed earlier in this chapter, four different types of scans are conducted for complete data processing. The “Reference” scans, consist of 24 scans where both secondary and main flows use copper sulfate solution. These scans are used to determine what the signal magnitude should be in the flow when there is 100% concentration. The “Inverted” scans consist of 23 scans with main flow at 0.018 M copper sulfate solution and the secondary flow is deaerated water. These scans are combined with “Standard” scans - 24 scans with secondary flow at 0.018M copper sulfate solution and the main flow is deaerated water. The fourth type of scan is the “Background” scan, where the 20 scans have deaerated water as both the main and secondary flow. The large number of scans was used because the SNR increases with increasing number of scans. A separate calibration process was used to determine how many scans are needed to achieve the target SNR. Each scan required 2 minutes and 6 seconds. The total number of scans that can be performed is limited by the amount of main flow contamination that can be sustained to achieve good data quality. The MRC uncertainties are combined as in Equation 2.8 to find the total uncertainty for the point-by-point concentration measurements using the root-sum of squares technique. The point-by-point concentration measurements were determined to have an uncertainty of less than 3%.

### **Temperature Measurements in High Subsonic Mach Number Airflow**

The high subsonic Mach number air flow experiments are conducted in a test channel that is identical to the one used for MRV/MRC measurements, except that the test section upper wall was modified to allow a traversing stagnation temperature probe

to be inserted. The same flow development section is used for both the air and water experiments. Air flow is supplied to the channel using a large external Ingersoll-Rand compressor and controlled using a pilot-operated pressure regulator. The flow is then split into main and secondary flows, each of which is metered by its own pressure regulator and orifice plate. The secondary flow then passes through a 2kW heater controlled by a variable AC transformer, which is used to create a stagnation temperature difference between the main and secondary flows.

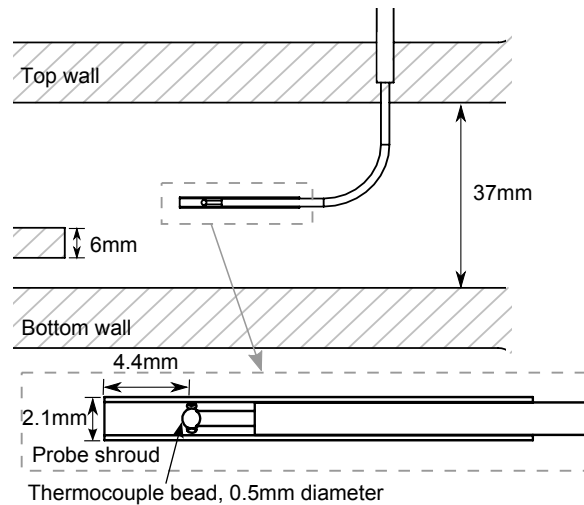


Figure 2.10: Schematic of stagnation temperature probe

Stagnation temperature profiles are measured using a traversing thermocouple probe illustrated in Figure 2.10. The probe was designed following guidelines in Ladenburg [35]. A 0.5 mm diameter thermocouple bead mounted on a 1.6 mm diameter stem is surrounded by a 2.1 mm outer diameter shroud which protrudes 4.4 mm upstream of the bead. The shroud has four 0.5 mm diameter vent holes at the position of the thermocouple bead. The probe is calibrated in the main flow freestream and the recovery factor is found to be 0.97. This factor is applied at each measurement point using Equation 2.12:

$$T_0 = T_p \left( \frac{1 + \frac{k-1}{2} M^2}{1 + (RF)^{\frac{k-1}{2}} M^2} \right) \quad (2.12)$$

where  $T_p$  is the temperature measured by the probe,  $k$  is the specific heat ratio of the working fluid,  $T_0$  is the calculated stagnation temperature,  $M$  is the local Mach number, and  $RF$  is the recovery factor. The probe is mounted to a stepper motor driven traverse to take profiles against the vertical ( $y$ ) coordinate. Probe access ports are located at nine evenly spaced streamwise locations in the spanwise center of the test section from  $x = 11.4$  mm to  $x = 59.4$  mm and at five evenly spaced streamwise locations 10 mm off-center from  $x = 7.2$  mm to  $x = 55.2$  mm, where  $x = 0$  is defined as the trailing edge of the splitter plate. The mainstream stagnation temperature is measured by a fixed probe located in the inlet section just upstream of the contraction and the secondary flow stagnation temperature is measured by a thermocouple mounted within the pin fin array upstream of the test section. Calibration of the secondary stream reference probe gives a recovery factor of 0.93. All temperature probes use standard K-type thermocouples measured via a computer controlled multimeter (Fluke 8842A) over a GPIB interface. The thermocouples are calibrated using a polynomial fit to NIST K-type calibration tables. The constant in the polynomial expression is determined by using a reference ice bath in order to prevent drift.

Static pressure is measured through wall taps located just upstream and downstream of the contraction in the main flow and just upstream of the test section in the secondary flow using a single transducer through an array of solenoid valves. These measurements are then used to calculate the Mach number of the main flow using isentropic relations. Temperature and pressure measurements for a single profile run are taken and recorded by a LabView data acquisition program. For each temperature measurement, 32 samples are taken at a sampling frequency of 80 Hz, while for each

pressure measurement, 100 samples are taken at a frequency of 1 kHz. Each profile is the average of three runs at a single location with the same temperature difference. Two profiles are taken at each location, with a single profile taken with either a 15°C, 20°C, or 30°C stagnation temperature difference between main and secondary flows, and a second profile with both main and secondary flows at room temperature.

The uncertainty of the normalized temperature profiles taken by the air experiment is calculated by first determining the uncertainty of each thermocouple measurement. These uncertainties are composed of repeatability, drift range and imperfect recovery of stagnation temperature, all of which are experimentally determined. Total uncertainty is then calculated using the root-sum of squares technique referenced in Section 2.5.1. The uncertainty of the main flow Mach number is calculated with the same technique using the variance of pressure transducer measurements observed over the course of a profile run. The calculated uncertainties of the normalized temperature and the main flow Mach number are 2.3% and 1.2%, respectively.

## 2.5.2 Results

For the airflow experiments, the main flow Mach number is set to 0.7, giving a main flow velocity of 234 m/s and a Reynolds number of 86,000. The blowing ratio is 0.8. Other experimental parameters are detailed in Table 2.2. Note that the blowing ratio is identical for the two experiments but the Reynolds number of the water experiment ( $Re = 12,000$ ) is a factor of 7 smaller than the airflow experiments. Both Reynolds numbers are in the fully turbulent regimes. Comparison at identical Reynolds numbers would be preferred to obtain dynamic similarity and to leave the Mach number as the only parameter varied between the two experiments. However, the water channel cannot be made significantly larger due to the constraints of the MRI scanner, and it is not feasible to supply a larger volumetric flowrate. This experiment can be seen as a test of the applicability of MRI techniques to the study of high Reynolds number

flows where neither the Mach number nor the Reynolds number can be matched. The particular geometry studied helps reduce Reynolds number sensitivity. The trips reduce Reynolds number effects for the boundary layer on the upper surface of the splitter plate, and the cylinder array in the secondary flow forces that flow to be fully turbulent. Furthermore, the blunt, sharp-edged splitter plate ensures that there is no Reynolds number effect on the flow separation. On the other hand, no effort was made to desensitize the side and top wall boundary layers or the cylinder array to Reynolds number variations.

All the data are presented in a coordinate system with the  $x$ -,  $y$ -, and  $z$ - directions defined as streamwise, wall-normal, and spanwise directions, respectively. The  $x = 0$  coordinate is set to the trailing edge of the splitter plate, with positive  $x$  corresponding to increasing downstream location. The location  $y = 0$  is defined as the bottom wall of the channel, and  $z = 0$  is defined as the centerplane in the spanwise direction.

### **Velocity field obtained by MRV**

MRV measurements were made of the 3D velocity field in the water flow to assess the general flow features of the experimental configuration and to ensure that no unexpected flow structures would affect the mixing measurements. Similar 3D measurements in the compressible air flow would be much more challenging and were not attempted. Figure 2.12 shows streamlines computed from the MRV data set in the centerplane ( $z = 0$ ). The flow behaved as expected, with generally straight streamlines outside of the direct wake of the splitter plate. In this region, there is significant recirculation up to about 2 splitter plate heights downstream of the trailing edge. Where the recirculation region closes, the streamlines dip slightly down as the mainstream mixes with the secondary flow due to the effect of the non-unity blowing ratio. In the mainstream flow, a series of five 0.8mm-thick boundary layer trips create

a fully turbulent boundary layer that is thinnest in the centerplane of the channel. The thickness of the boundary layer is greatest near the sidewall, where both friction on the sidewall and longitudinal vortex structures affect the boundary layer growth.

There is significant mean flow three-dimensionality that is best illustrated by isosurfaces of streamwise vorticity plotted in Figure 2.13. It should be noted that the streamwise vorticity is plotted only below  $y = 12$  mm to show structures emerging from the secondary flow channel. Vorticity is calculated by differentiating the experimental velocity field point-by-point. The streamwise vorticity is normalized by the bulk mainstream velocity of 1.7m/s at  $x = 0$  mm and the splitter plate thickness of 6 mm. The dominant features of the flow are strong longitudinal vortices found along each sidewall. These produce coherent secondary flows within 2 splitter plate heights of each sidewall. The mean flow three-dimensionality is much weaker in the central region. Counter-rotating vortex pairs are seen in the wake of the final row of pin fins. These are noticeably smaller than the longitudinal vorticity structures introduced by the sidewalls and at this isolevel, they die out before the slot jet exit. This was examined by first quantitatively computing the local streamwise vorticity, then computing the root-mean-square (RMS) deviation from the mean, averaged over a given plane of data. The RMS shows the variability of the vorticity due to the experimental noise or weak vortices developed in the upstream channel. The vorticity is calculated for the region  $-10 \text{ mm} \leq z \leq 10 \text{ mm}$  and  $2 \text{ mm} \leq y \leq 4 \text{ mm}$  (this region is pictured in Figure 2.14). This area avoids the regions near the walls which have strong longitudinal vorticity. The RMS streamwise vorticity of this region is found to have a normalized value of 0.14, which is much less than than the vorticity in the sidewall region. The isosurfaces in Figure 2.13 defining the sidewall vortices are plotted at  $\pm 0.5$ , about 4 times the RMS vorticity in the central region. This shows that the tangled vortex structures behind the five rows of pin fins produce relatively weak mean secondary flow. Another factor to consider is the uniformity of the mean streamwise velocity in

the secondary jet flow. Figure 2.15 shows streamwise velocity contours at the plane  $y = 5$  mm, showing that the wakes decay downstream of the final pin fin row, leaving minor velocity variations by the splitter plate trailing edge and almost no measurable wakes beyond  $x = 30$  mm ( $x/h = 5$ ). The spatial RMS variation of the streamwise velocity over the same test region shown in Figure 2.14 is 6% of the bulk secondary flow velocity (1.4 m/s).

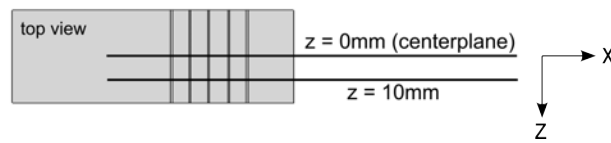


Figure 2.11: Orientation of extracted data

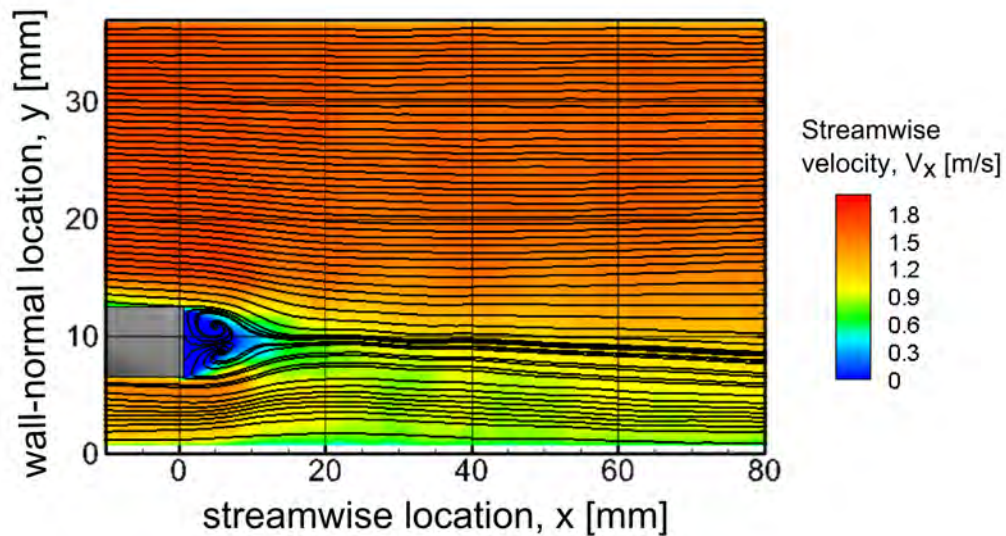


Figure 2.12: Streamlines and velocity contours at spanwise centerplane ( $z = 0$ ). The location of this plane is illustrated in Figure 2.11.

Normalized spanwise vorticity contours on the centerplane (Figure 2.16) illustrate additional features of the velocity field. The spanwise vorticity maps at other spanwise locations are similar, indicating that the three-dimensional features near the sidewalls have relatively weak effects on this dominant vorticity component. The rapid increase

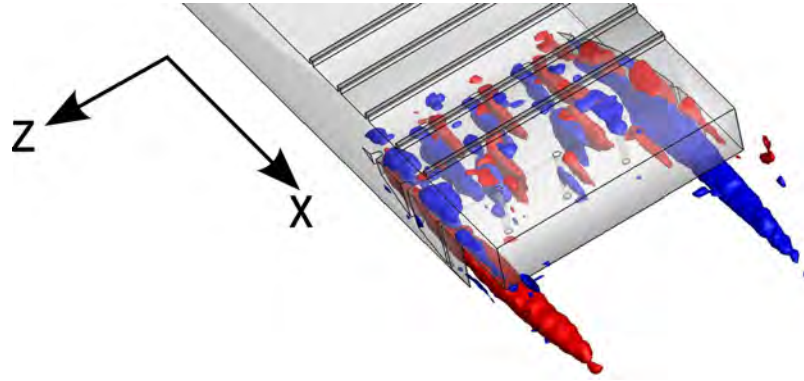


Figure 2.13: Isosurfaces of vorticity, plotted at normalized vorticity levels of  $\pm 0.5$ . Vorticity is normalized by bulk main flow velocity at  $x = 0$  mm and splitter plate height. Isosurfaces of positive vorticity are shown in red, while isosurfaces of negative vorticity are shown in blue.

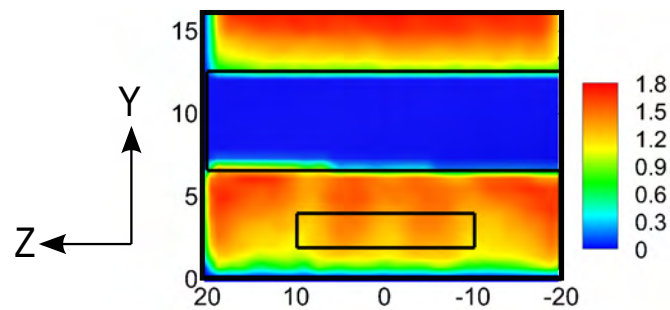


Figure 2.14: Streamwise RMS vorticity and velocity are calculated in the secondary flow at  $x = 0$  mm. A contour plot of streamwise velocity is shown in the  $y-z$  plane at  $x = 0$ , with a box showing the region  $-10 \text{ mm} \leq z \leq 10 \text{ mm}$  and  $2 \text{ mm} \leq y \leq 4 \text{ mm}$  over which the RMS calculations are performed. The end of the splitter plate is shown in gray, with part of the mainstream flow above and secondary flow below.

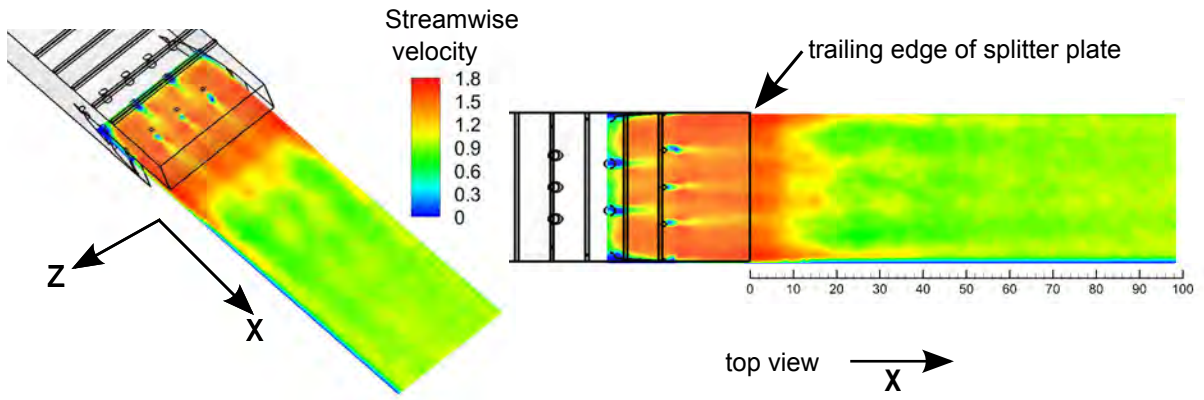


Figure 2.15: Contours of streamwise velocity at  $y = 5$  mm. Note that the three-dimensionality of the flow introduced by the pin fins is diminished in the wake of the trailing edge.

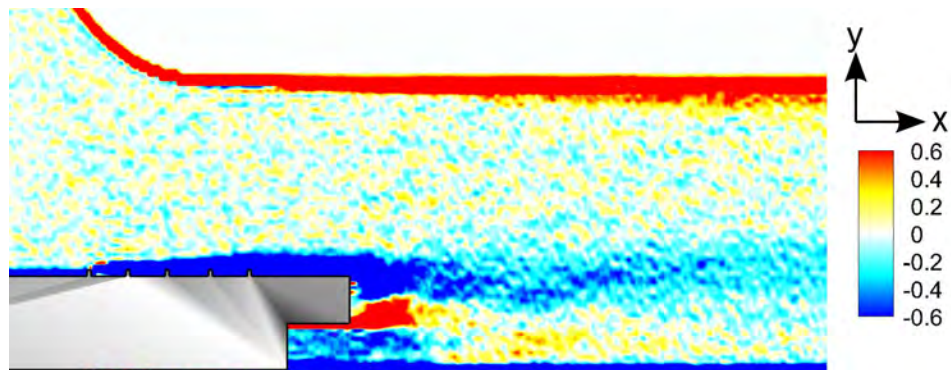


Figure 2.16: Spanwise vorticity contours plotted in the centerplane ( $z = 0$ ). The splitter plate is shown in gray. Large positive vorticity (counter-clockwise rotation) is shown in red, while large negative vorticity (clockwise rotation) is plotted in blue. The vorticity is normalized by a bulk mainstream velocity of 1.7 m/s and a splitter plate height of 6 mm. Noise resulting from the differentiation of the experimental velocity field shows up as small-scale spanwise vorticity variations in the mainstream flow in the region away from the splitter plate.

in the vortical layer thickness on the upper surface of the splitter plate begins at the location of the first trip showing the strong effect of the trips on the boundary layer. Furthermore, the thick splitter plate produces concentrations of both negative and positive vorticity in the near wake. This is characteristic of bluff body wakes and different than simple two-stream mixing layers where there is a single sign of vorticity.

### **Concentration field overview**

The MRC data set was acquired for the same conditions as the velocity data. The overall features of the concentration field are illustrated by a centerplane slice through the MRC data shown in Figure 2.17. Two of the mean flow streamlines from Figure 2.12 are superimposed for reference. This plot was made from raw, unfiltered MRC data. The variations seen, for example, at the edge of the yellow contour, are due to experimental noise. These data are time-averaged, so variations are not indicative of turbulent structures. The mainstream concentration is 0% and the secondary stream concentration is 100% upstream of the splitter plate trailing edge as expected. Fluid is entrained into the separated splitter plate wake from both streams so there is a region of intermediate concentration just downstream of the splitter plate (the same region that contains both large positive and negative spanwise vorticity pictured in Figure 2.16). Moving downstream, the concentration field takes on the appearance of a conventional turbulent mixing layer with the concentration spreading into the mainstream and clean fluid diluting the secondary stream. The three-dimensional features of the concentration field are illustrated in Figure 2.18 which shows a 60% concentration isosurface. Any location inside this isosurface has a concentration of 60% or higher. No smoothing of the measured concentration data was done, so the surface is slightly noisy, but it clearly shows the distortion of the concentration field by the sidewall longitudinal vortices shown in Figure 2.13. The vortices sweep secondary stream fluid upwards along the sidewall and mainstream fluid downward on their

inboard side. Also, secondary stream fluid is entrained into the vortex cores so that the 60% isosurface extends far downstream near the sidewalls.

Three dimensional features also are seen in the isosurface near the center of the channel. These are considerably weaker than the sidewall structures, but they are still easily apparent above the measurement noise. These features are apparently due to flow structures emanating from the cylinder array in the secondary flow feed. These features are better illustrated by a  $y$ - $z$  plane cut through the concentration data at  $x = 38$  mm, as seen in Figure 2.19. These data illustrate detailed information on the concentration field available from MRC. They also point out that it will be critical to ensure that temperature and concentration profiles are compared at the same spanwise positions.

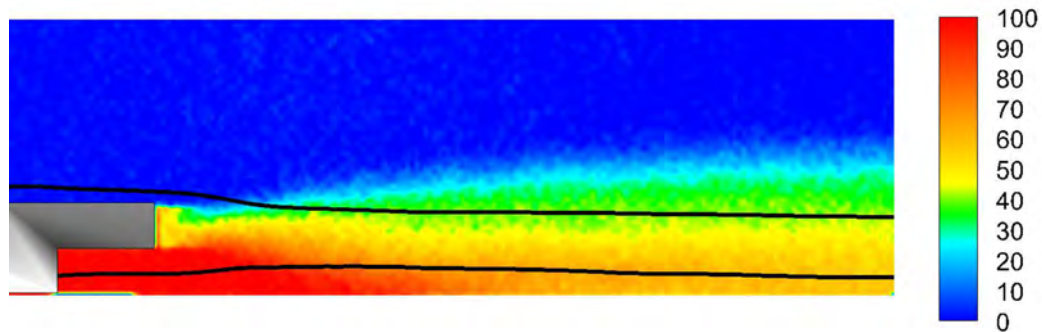


Figure 2.17: Contours of concentration at  $z = 0$  mm. Two mean flow streamlines from the MRV data are plotted for reference to Figure 2.12.

### Energy separation effects on the airflow temperature measurements

The stagnation temperature profiles measured in the airflow apparatus showed non-monotonic variation in the wake of the splitter plate when the temperature difference between the main and secondary streams was small as seen in Figure 2.20. This plot shows data at a single streamwise position, but similar variations were observed at all locations. The profiles are monotonic for larger temperature difference, but

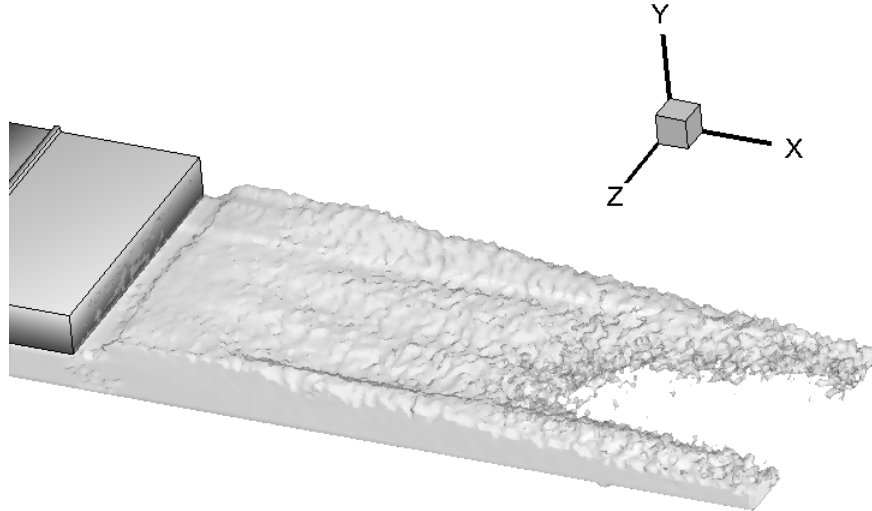


Figure 2.18: 60% isosurface of concentration. Any location inside of this surface has a concentration of 60% or higher.

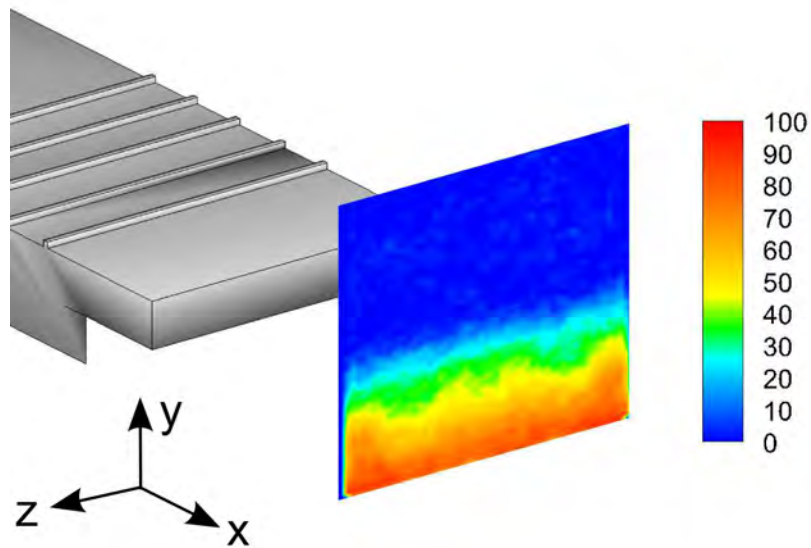


Figure 2.19: Concentration contours in the  $y$ - $z$  plane at  $x = 38$  mm. Note the presence of three-dimensional features on the sidewalls as a result of the sidewall vortices and in the center of the channel as a result of the longitudinal vorticity generated by the last row of pin fins.

there is still a substantial dip near the wake centerline and an increase in stagnation temperature at locations above the wake centerline. This is apparently due to the energy separation effect previously observed in simple wakes. Kurosaka et al. [34] studied the wake of a 2D cylinder both experimentally and numerically and found that hot and cold spots exist side-by-side and are associated with coherent vortex structures. Stagnation pressure and temperature fall as fluid moves toward the vortex center because the fluid is expanding and doing work. Moving away from the vortex center, the pressure recovers and the stagnation temperature increases as work is done on the fluid. This causes a measureable reduction in the mean stagnation temperature near the wake centerline and a small overshoot as the stagnation temperature recovers at the edge of the wake.

In the present case, the energy separation effect is superimposed on the profiles created by turbulent mixing between streams of two different temperatures. Figure 2.20b shows a typical temperature profile measured with the main and secondary streams at the same stagnation temperature. The shear layer structure is somewhat more complicated than the simple cylinder wake experiments by Kurosaka et al., but the same basic behavior is observed. There is a minimum in temperature in the center of the wake surrounded by local maxima above and below. Following the interpretation of Kurosaka et al., the effects of the energy separation should be independent of the temperature difference between the two streams. To check this, temperature profiles are acquired for temperature differences of 0°C, 15°C, and 30°C between the main and secondary streams. Normalized temperature profiles are then calculated as:

$$\theta = \frac{(T_{heated} - T_{unheated}) - T_{\infty,main}}{T_{\infty,secondary} - T_{\infty,main}} \quad (2.13)$$

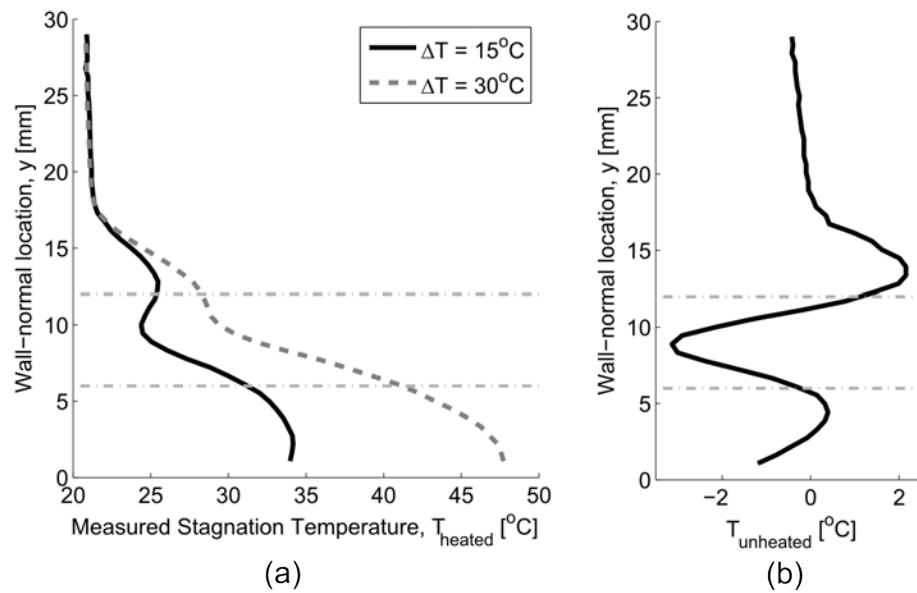


Figure 2.20: Energy separation effect: raw stagnation temperature profiles measured at  $x = 19.4$  mm,  $z = 10$  mm. On the left are the stagnation temperature profiles ( $T_{heated}$ ) measured at two different temperature differences. Note the non-monotonic behavior of the  $\Delta T = 15^\circ\text{C}$  case. In the  $\Delta T = 30^\circ\text{C}$  case, the non-monotonicity of the profile is lessened, which corroborates the hypothesis that this effect is small at large temperature differences (such as those found in real engine environments). On the right is plotted the stagnation temperature profile in the same location with both the main and secondary flows at the same temperature, giving the quantity  $T_{unheated}$ .

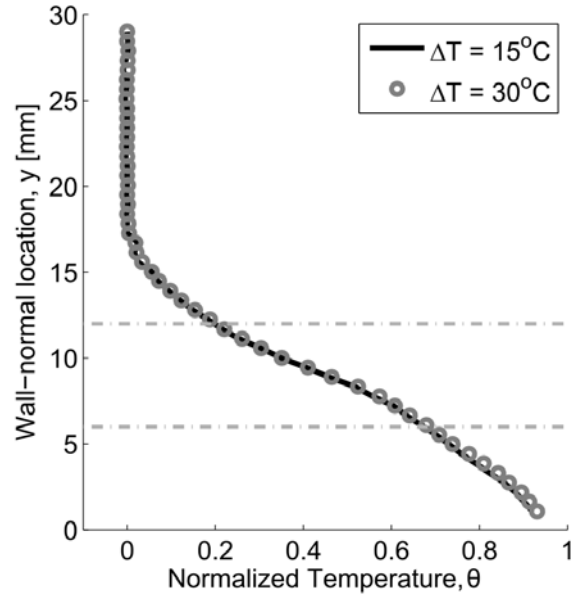


Figure 2.21: Normalized temperature profiles at  $x = 19.4$  mm,  $z = 10$  mm. Note that the difference between the two cases is within the line width of the plot.

Where  $T_{heated}$  is the temperature profile and  $T_{unheated}$  is the temperature profile measured with the main and secondary streams at the same temperature. Figure 2.21 shows that the normalized temperature profiles are nearly identical for both temperature differences measured. The same excellent agreement of the normalized stagnation temperature profiles is found at all streamwise positions lending strong support to the conclusions of Kurosaka et al. Therefore, the normalized temperature profiles should be directly comparable to the MRC concentration profiles.

Although the temperature difference between the two flows is relatively small, the presence of the energy separation effects shows that there does exist a significant density difference.

### Normalized concentration and temperature profile comparison

Temperature profiles are measured at fourteen locations in the test section. At each of these locations, an unheated profile and a heated profile are taken with a 20°C inlet temperature difference. The unheated profile is first subtracted from the heated profile and normalized as seen in Equation 2.13. Concentration profiles are extracted from the full-field MRC data and normalized as detailed in Section 2.5.1. Each voxel in the MRC data has a width of 0.8 mm in the spanwise direction, which is approximately 1/3 the diameter of the temperature probe. Therefore, the MRC profiles are averaged over a 3-voxel width centered on the probe axis for direct comparison to the temperature probe data.

Figure 2.22 plots the normalized temperature and concentration profiles for five streamwise positions in the centerplane of the data. The temperature and concentration profiles both follow monotonic behavior with respect to  $y$ , the wall-normal direction. In the most upstream location ( $x = 11.4$  mm), the concentration and normalized temperature are both close to 100% from  $y = 0$  mm to about  $y = 6$  mm. In the wake of the splitter plate ( $6 \text{ mm} \leq y \leq 12 \text{ mm}$ ), the profiles monotonically decrease to below 3% (measurement uncertainty is 3% or less for both air and water techniques), illustrating that little mixing of the mainstream flow with the secondary flow has occurred at locations greater than  $y = 12$  mm at this streamwise location. Moving downstream, the wake of the splitter plate spreads, causing mixing to occur over a larger wall-normal region with increasing streamwise position. At  $x = 47.4$  mm, the normalized concentration is 68% and the temperature is 71% at the bottom wall ( $y = 0$  mm). Both temperature and concentration monotonically decay to below 3% at  $y = 20$  mm, indicating that at this streamwise location, the turbulent mixing occurs over the range  $0 \text{ mm} \leq y \leq 20 \text{ mm}$ . By the farthest downstream location plotted ( $x = 59.4$  mm), the mixing area has only slightly extended to include the region  $0 \text{ mm} \leq y \leq 22 \text{ mm}$ . From these results, it can be seen that the concentration and

temperature measurements are in very close agreement, indicating that the scalar transport analogy between mass and heat transfer is applicable despite differences in compressibility and Reynolds number. Of particular note is the mixing behavior at the outer edge of the mixing layer, where the profiles are closely matched. This strongly suggests that the large scale turbulence structures are identical in the air and water experiments since they produce the largest outward excursions of secondary fluid.

Figure 2.18 shows that the flow is weakly 3D in the midspan region ( $-15 \text{ mm} \leq z \leq 15 \text{ mm}$ ) due to the effect of the last row of pin fins in the cylinder array located in the secondary flow inlet section. Therefore, it is important to compare data at multiple spanwise positions. Figure 2.23 plots normalized temperatures and concentrations 10mm away from the centerline ( $\Delta z = 10 \text{ mm}$ ). While these profiles are taken at different streamwise positions in comparison to the data presented in Figure 2.22, the general behavior is the same. At the most upstream measurement location ( $x = 7.2 \text{ mm}$ ), the measured concentrations and temperatures are close to 100% for  $0 \text{ mm} \leq y \leq 6 \text{ mm}$  and close to 0% for  $y > 12 \text{ mm}$ , with a monotonic decrease in the measured value with increasing  $y$ -location in the intermediate region. Moving downstream, the mixing region increases in the  $y$ -direction to include  $0 \text{ mm} \leq y \leq 20 \text{ mm}$  by the last measured streamwise position,  $x = 55.2 \text{ mm}$ . Similar to the centerline temperature and concentration comparisons, at each of the streamwise locations, the agreement between the normalized concentration and temperature profiles is excellent, which demonstrates that the scalar transport analogy is applicable.

The correlation coefficient ( $R^2$ ) between the two types of measurements is calculated for each profile location using the relationship in Equation 2.14 and taking the concentration measurements as “observed” data and the temperature measurements as “accepted” data. For each of the 14 profile locations, the correlation coefficient was calculated and found to have a value of  $R^2 = 0.98$  or higher for all of the locations

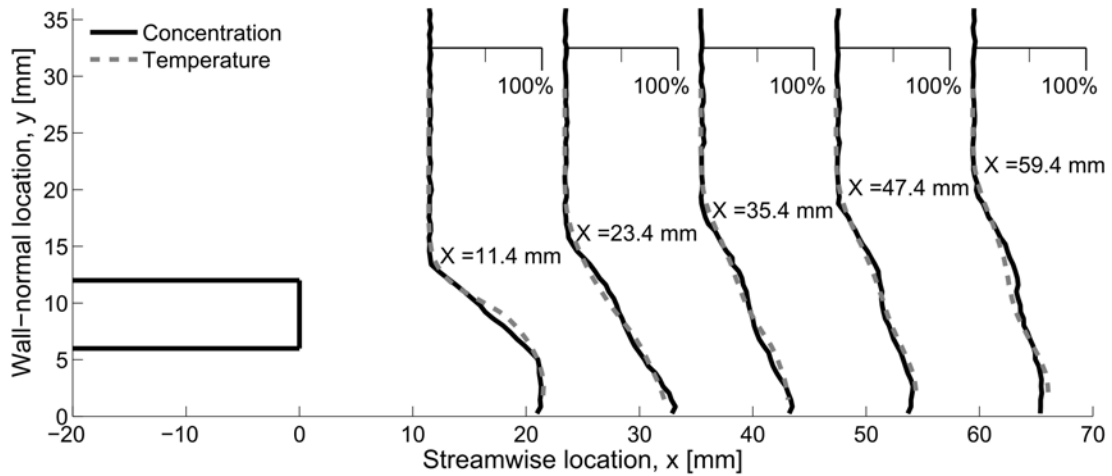


Figure 2.22: Normalized profile comparison:  $x = 11.4$  mm,  $x = 23.4$  mm,  $x = 35.4$  mm,  $x = 47.4$  mm,  $x = 59.4$  mm, centerline ( $z = 0$  mm). Data was gathered at 9 streamwise positions in this spanwise location, but only 5 profiles are plotted here for better visualization. The additional profiles (not shown here) were taken at  $x=17.4$  mm, 29.4 mm, 41.4 mm, and 53.4 mm.

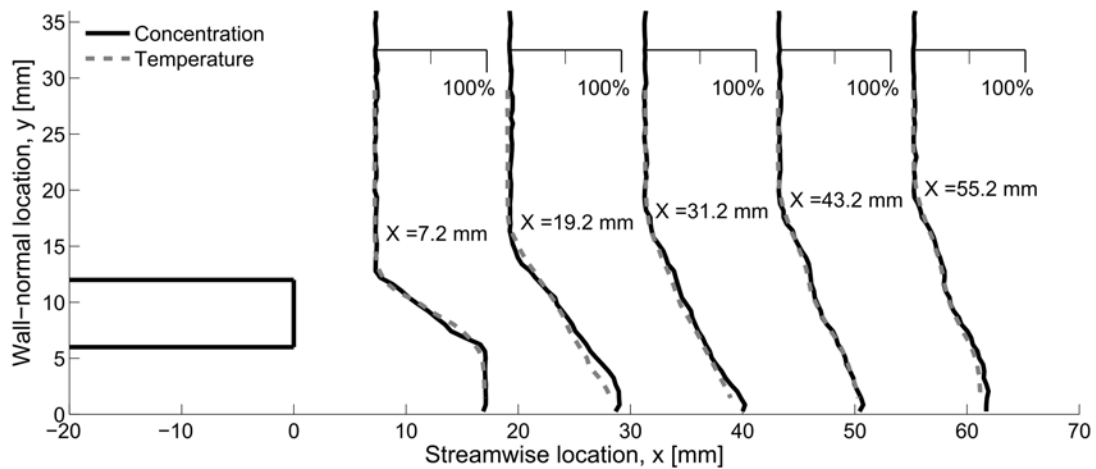


Figure 2.23: Normalized profile comparison:  $x = 7.2$  mm,  $x = 19.2$  mm,  $x = 31.2$  mm,  $x = 43.2$  mm,  $x = 55.2$  mm, off-centerline ( $z = 10$  mm)

(an  $R^2$  value of 1 indicates a perfect fit between two data sets). The mean absolute difference between normalized temperature and normalized concentration is also calculated using Equation 2.15 for the range  $y_1$  to  $y_2$ , where  $y_1$  is the y-location at which 95% concentration is found, and  $y_2$  is the location at which 5% concentration is found for each streamwise position.  $N$  is the total number of data points in this range. The mean absolute difference defined in Equation 2.15 was calculated at each of the fourteen profile locations and the average of the fourteen  $\Delta E$  values was found to be 3.6%. The maximum of this quantity was determined to be  $\Delta E = 5.7\%$ . This is comparable to the combined measurement uncertainty of the two techniques, indicating that the temperature and concentration profiles provide the same information regarding the mixing of the main and secondary flows.

$$R^2 = 1 - \frac{\sum_i (c_i - \theta_i)^2}{\sum_i (c_i - \bar{c})^2} \quad (2.14)$$

$$\Delta E = \frac{1}{N} \sum_i^N |c_i - \theta_i| \quad (2.15)$$

From this comparison, it can be seen that the mechanisms governing turbulent mixing in the compressible air flow and water experiments are fundamentally the same. The only difference that can be seen is that the compressible fluid experiences the energy separation effect which is observable as small differences in the stagnation temperatures of the two streams. At large temperature differences, this effect is dominated by the turbulent mixing and is assumed to be negligible at the large temperature differences experienced in practical high speed mixing applications such as turbomachinery cooling. The power of the MRV/MRC experimental technique is in its fast data acquisition period (less than 1 day) for a fully 3D, 3-component velocity field and concentration map containing over 5 million spatial data points. In

contrast, a set of temperature profiles can be acquired using thermocouple instrumentation in the same time period, but at only about 700 total spatial data points, and velocity field measurements require the fabrication and machining of an entirely independent test section and experimental setup. The excellent agreement between the MRC data and the thermocouple experiments shows that the MRC technique can be used to accurately predict turbulent mixing behavior in compressible flows with the limitations that the turbulent mixing must be strong enough to overwhelm any effects of the molecular diffusion and the flow must be shock free. Care must be taken in setting up any model experiment to avoid the effects of Reynolds number mismatch between the model and full scale. In particular, flows involving laminar/turbulent transition or strong sensitivity to boundary layer growth rates should not be tested at subscale Reynolds number. The present experiment was set up specifically to avoid such sensitivity.

### 2.5.3 Conclusions

Experiments were performed in air and water on two test channels of identical geometries. Turbulent mixing of a passive scalar was measured in both channels using temperature and concentration as the scalars in the air and water experiments, respectively. Stagnation temperature measurements were collected in the air experiments using a stagnation temperature probe, while the velocity and concentration fields were measured in the water experiments using Magnetic Resonance Velocimetry and Concentration experimental techniques. Despite a factor of 7 difference in Reynolds number and a Mach number in the high subsonic regime for the air experiments, the differences observed between the two experiments were found to be within the measurement uncertainties of the experimental methods. From these results, it can be concluded that the MRV/MRC experimental technique can be used to study the same turbulent mixing mechanisms that exist in high subsonic Mach number flows. Any

differences in the raw data gathered from the two experiments is the result of the energy separation effect that is experienced in compressible flows. This effect is caused by flow geometry and conditions, and it is hypothesized that it is independent of the temperature. Experiments at moderate temperatures show a diminishing effect with increasing temperature difference, and at the high temperature differences seen in turbomachinery applications, this effect should be negligible. Therefore, MRV/MRC experimental studies of mixing in turbomachinery applications can be used in lieu of more costly and time intensive compressible air flow experiments to improve turbulent mixing models used in computational fluid dynamics.

Real turbomachinery applications often have a significant density difference between the two flow streams due to large temperature differences. This cannot be replicated in either water flow or low temperature air flow experiments without the use of a second, more dense, fluid. The present experiment has not explored the effects of these density differences on the turbulent mixing or the capability of MRI techniques to capture any such effects.

# Chapter 3

## Double Passage Vane Cascade Experimental Design

*This chapter includes excerpts from a manuscript accepted to the 2014 ASME International Gas Turbine Institute Conference cited as Yapa SD, Elkins CJ, Eaton JK (2014). “Endwall vortex effects on turbulent dispersion of film coolant in a turbine vane cascade”. Proceedings of ASME Turbo Expo 2014 (GT2014-25484).*

This chapter discusses the difficulties in simulating a turbine environment with experiments and walks through the evolution from a real engine environment to double passage vane cascade experiments. The design process of the double passage vane cascade is presented in detail. The specific MRV and MRC experimental equipment and setup are also presented, along with the experimental geometry.

### 3.1 Rotating, Infinite, and Linear Cascades

Traditional experiments on quantitatively measuring velocity and mixing in the wake of the trailing edge of a turbine blade have been done in linear cascades. A cascade is a collection of vanes or blades, arranged in a periodic fashion. These experiments use

pressure probes, thermocouple measurements, and optical methods. The true environment for a blade from a high pressure turbine is in a circular rotating environment (blades are fixed into a rotating hub using dovetail joints). Rotating experiments do exist, such as the Large-Scale Rotating Rig (LSRR) at United Technologies Research Center. The LSRR is a rotating wind tunnel designed to imitate the axial flow found in turbomachinery at a low speed and large scale [16]. However, rotating setups have many limitations in terms of instrumentation, measurement resolution, and the speed of the flow. The design time for these rigs is 3-4 years long, creating a lag between when a need for data is presented and when it is actually collected [33].

The flow around the blades in a turbine could be replicated using an infinite linear cascade, which is a theoretical model in which the blades are arranged in a linear, periodic fashion. Because the cascade is “infinite”, the conditions experienced by each blade are periodic, and behave in the same way as they would around a blade in a circular rotor or stator. Practical experiments approximate an infinite linear cascade using a linear cascade, usually comprised of four or more turbine blades arranged in a periodic configuration (see Figure 3.1). The experiments are performed around the central blade in the linear cascade which is surrounded by “dummy” blades that serve to establish the periodic boundary conditions. Linear cascades allow for well-characterized and defined boundary conditions and can provide better measurement resolution than rotating rigs. The middle vanes or blades of the linear cascade have nearly the same boundary conditions as those in the full circular cascade, allowing for the conclusion that a linear cascade can essentially replicate results from a full circular cascade.

The number of blades used in a linear cascade is limited by the physical size and flowrate requirements of the apparatus. In situations where maximum measurement resolution is required in a limited space, the number of blades in the cascade is reduced. The smallest linear cascade is a so-called double passage cascade, in which

a single vane or blade is placed between two channel walls that have been contoured to replicate the same boundary conditions as would exist in an infinite linear cascade (Figure 3.1). The challenge of the cascade design process then is to find shapes for the outer walls that will cause the flow around the central vane to be the same as if it were in an infinite cascade.

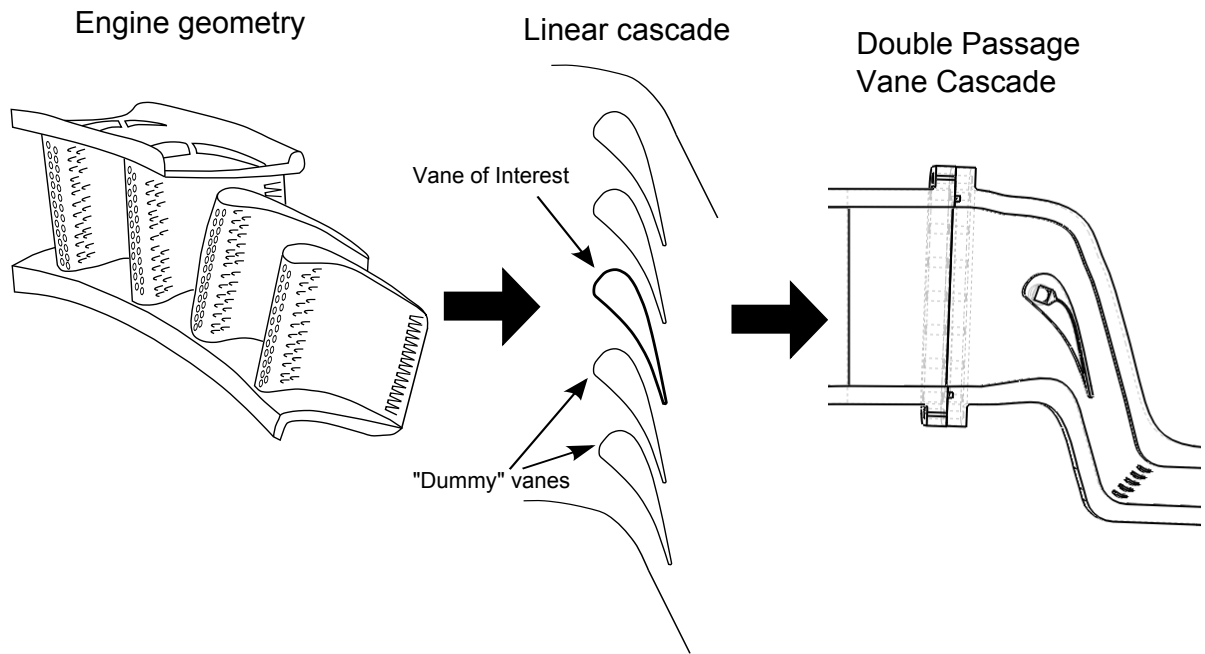


Figure 3.1: Relationship between original engine geometry and double passage vane cascade experimental setup. The evolution from a circular engine geometry to linear cascade to double passage vane cascade is shown. A rotating cascade and an infinite linear cascade have the same boundary conditions. A linear cascade mimics these boundary conditions, but only on a vane located in the middle of the cascade. The other “dummy” vanes are present to create the periodic boundary conditions for the vane of interest. The walls of the double passage channel create a pressure distribution on the surface of the vane that matches the vane pressure distribution in the linear cascade.

## 3.2 Design of Double Passage Vane Cascade Geometry

Arts et al. [1] published linear cascade experimental results for a transonic turbine guide vane performed at the von Karman Institute for Fluid Dynamics (VKI). This same vane shape was selected for the double passage experiments because it has been well studied and has a realistic yet non-proprietary airfoil shape. Furthermore, the flow in the VKI cascade was subsonic so there were no shock waves or other factors that could not be represented in a water flow experiment. The VKI experiments studied the airfoil static pressure distribution and the effect of free-stream turbulence and Reynolds number on surface heat transfer at transonic conditions, but no measurements were taken in the wake or endwall regions.

The goal of the design process was to create a double-passage vane cascade that has the same numerically predicted vane pressure coefficient distribution as would exist in an infinite cascade of such vanes. This required an optimization procedure to select the shape of the outer cascade walls to accurately produce the desired pressure coefficient distribution. The general method for inverse design of a double passage blade cascade for a high pressure turbine was set forth in Laskowski et al. [38]. They used a CFD-based optimization scheme that computed the desired isentropic Mach number distribution on the blade surface for an infinite cascade of such blades. The outer wall shape was parameterized in terms of a set of control parameters, and a cost function based on the difference between the calculated and desired isentropic Mach number distributions was minimized during the optimization process. That cascade was designed to replicate a highly loaded turbine shape in which the Mach number exceeded 1.5. Shock waves were present. A different procedure was required for the present flow in which the entire flow is at a much lower Mach number.

The overall scale of the present experimental apparatus was chosen to maximize

the test section size within the constraint that the entire apparatus must fit into the magnet bore and the test section should fit within the transmit/receive head coil. Furthermore, the main flowrate is limited by the available electrical power for pumps. In consideration of these constraints, the inlet flowrate is set to 180 LPM and the vane chord is 8.84 cm. The blade pitch to chord ratio is set to 0.85 to be consistent with the VKI experiments and the blade span is 5.5 cm.

A two dimensional, infinite cascade CFD simulation was the baseline for the double passage design. This was run using the commercial CFD package FLUENT for the same conditions as the MRI experiments, namely a working fluid of water at room temperature with the flowrate and length scale mentioned above, giving a vane Reynolds number of approximately 80,000. Figure 3.2 helps to illustrate the boundary conditions of the simulation. The vane geometry was imported into the software GAMBIT, commonly used to build and mesh CFD test cases. A velocity of  $\vec{v} = 0.43$  m/s was set as a constant velocity inlet condition and the outlet condition was set to exit to atmospheric pressure. Periodic boundary conditions were set as the top and bottom walls.

The CFD simulation was run at steady-state conditions, with a  $k-\epsilon$  turbulence model with enhanced wall functions. The pressure coefficient distribution determined by the infinite cascade computation agreed well with the pressure measurements from the experiments at VKI [1], conducted in a large, multi-blade cascade, except for a discrepancy near the suction peak of the airfoil (see Figure 3.3). The reason for this difference was not clear. The VKI data did have some noise, although it did not appear large enough to account for the differences. More likely, the differences were due to compressibility effects since the VKI experiments were run at an outlet Mach number of 0.84.

As a first step in the design of the double passage cascade, streamlines were extracted from the infinite cascade solution and became the basis for the channel walls

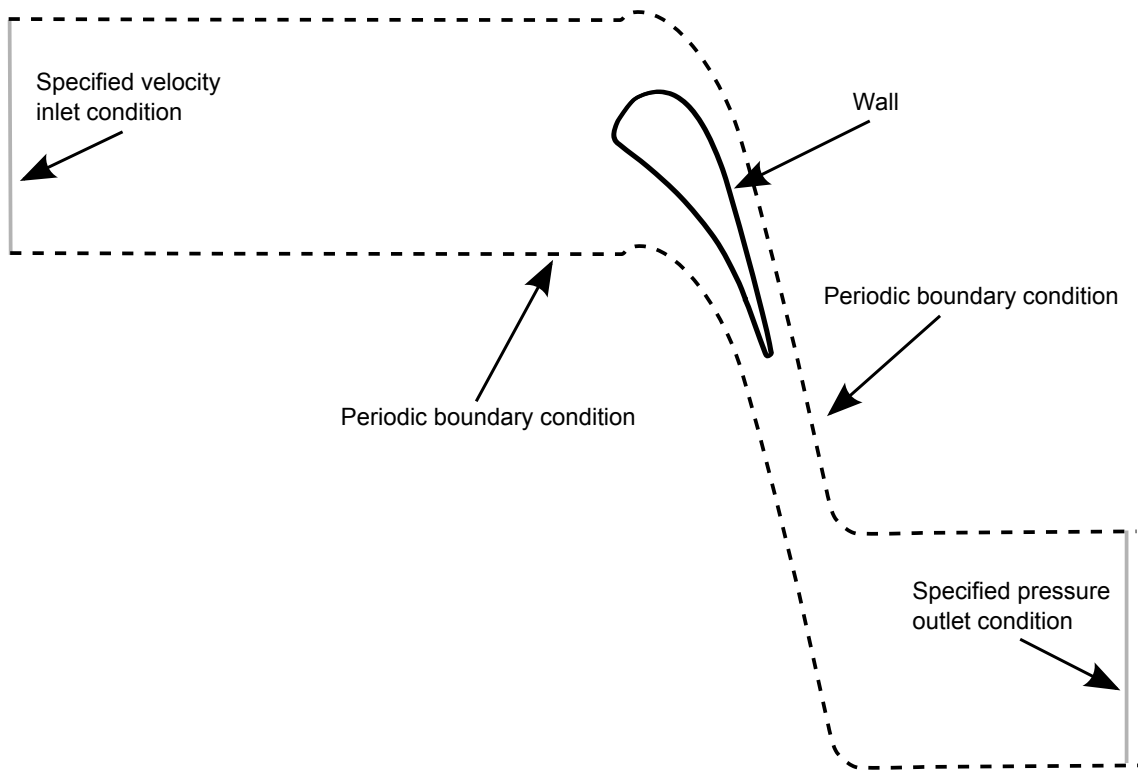


Figure 3.2: Setup of infinite cascade CFD simulation.

of the double-passage vane cascade. These channel walls were then slightly modified to account for displacement thickness since the no-slip condition was enforced when the streamlines were turned into physical walls. A “by-hand” optimization was performed using this channel wall shape as the initial guess. At each step of the optimization procedure, the pressure coefficient distribution on the vane was calculated and compared to the distribution for the infinite cascade until the pressure coefficient distributions plotted in Figure 3.3 were obtained. Good agreement was found between the infinite cascade and the final iteration of the double passage vane cascade. In all, 43 wall configurations were simulated before converging to a shape that gave the correct pressure coefficient distribution. In Figure 3.4, the differences between the channel wall shapes of the first iteration of the double passage cascade and the final iteration are plotted against each other. The first iteration channel walls are shown in yellow and outlined by a black line. The final iteration, iteration #43, is plotted in red and outlined in black. The channel shape slowly evolved over the optimization process, with one of the main changes being the angle at which the inlet flow is directed with respect to the vane leading edge.

It should be noted that the pressure coefficient distribution from the final iteration of the double passage optimization matches the infinite cascade computation, but differs from the previous experimental results (from VKI) near the suction peak. This was expected since the double passage cascade was designed to match the pressure of the infinite cascade distribution. The goal of this design process was not to precisely match the VKI experiments since both the Reynolds and Mach numbers are much different. Also, the precise inlet conditions of the VKI cascade were not matched. However, the general behavior of the flow around the vane should and does match between MRV results and VKI experiments. In any case, the final velocity field of the present experiments will be different from the VKI experiments in the wake due to the addition of pressure side cutback cooling to the vane trailing edge.

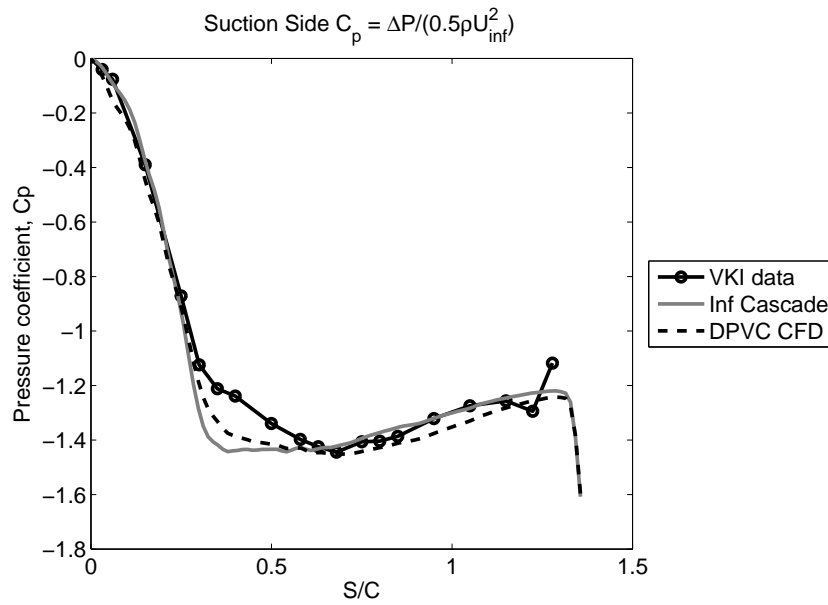
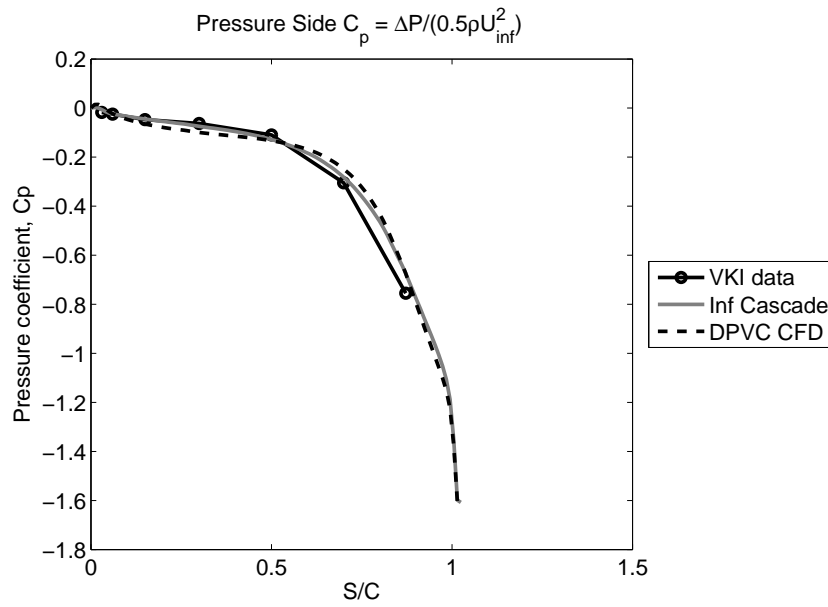


Figure 3.3: Pressure coefficient distribution of vane from FLUENT simulations. Data from linear cascade experiments performed in air at the VKI are also presented. Figure 3.3(a) plots pressure coefficient distribution vs. normalized curvilinear coordinate for the pressure side of the vane. Figure 3.3(b) plots pressure coefficient distribution vs. normalized curvilinear coordinate for the vane suction side. The curvilinear coordinate,  $S$  is normalized by the airfoil chord,  $C$ .

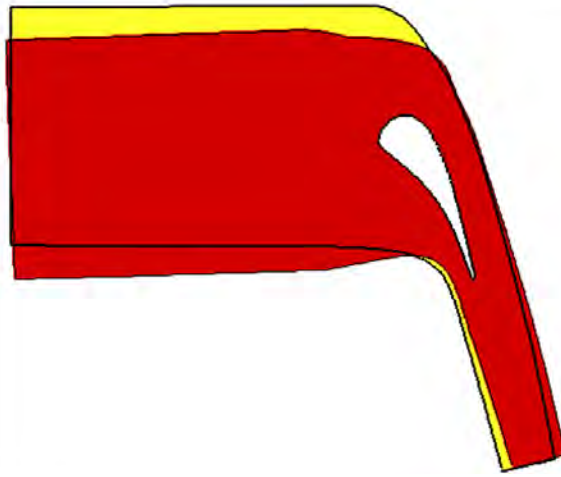


Figure 3.4: Evolution of double passage vane cascade channel walls. The first iteration walls were extracted from streamlines from the infinite cascade (which were then modified to account for the no-slip condition). Over the course of the optimization process, the channel walls evolved from what is plotted in yellow to what is plotted in red (channel iteration #43).

### 3.3 Design of Experimental Setup

The test configuration is built into the dedicated, portable water channel illustrated in Figure 5.1 to facilitate MRI measurements. Flow is pumped from a large reservoir of deaerated water and metered before entering the apparatus from the left via a 1.5-inch hose. Three successive diffusing sections expand the cross section to 153mm x 153mm. Each diffuser includes multiple grids to improve flow uniformity. A 3.3:1 area ratio three-dimensional contraction feeds into the 56mm x 126mm inlet of the double-passage vane cascade test section. Downstream of the vane and wake development section, a set of small vanes turns the flow back to exit from the MRI scanner. A separate pump and flow meter system supplies film cooling flow through a hole in the end of the vane. The experimental test channel is made using a rapid prototyping technique known as stereolithography (SLA). The channel walls determined by the

optimization are exported from FLUENT and used as the basis for the double passage vane cascade built in SolidWorks, a commercially available CAD software. The channel size is limited both by the maximum volume that can be fabricated using SLA (approximately  $240\text{mm} \times 240\text{mm} \times 250\text{mm}$ ) and by the size of the transmit-receive head coil used during data acquisition. The head coil is an annular cylinder approximately 410mm in length with an inner diameter of about 273mm. Additionally, the channel has to fit inside the bore of the magnet, essentially demanding that the channel be more or less straight.

The VKI airfoil used is a cambered vane used in highly loaded transonic environments. The profile of the vane is illustrated in Figure 3.6. The vane has  $77^\circ$  of turning. The manufacturing coordinates of the airfoil are presented in Appendix A. In this appendix,  $x - y$  coordinates, as well as curvilinear and normalized curvilinear coordinates, are provided. Coordinates of the passage walls are also provided in Appendix B. A pressure-side cutback trailing edge film cooling system designed to replicate a realistic film cooling scheme is added to the VKI vane shape. The dimensions of this system are summarized in Table 3.1 and a schematic of the modified vane is presented in Figure 3.7. There are nine rectangular film cooling slots separated by tapered lands. Each slot is 3.4 mm wide and 1.1 mm tall and is located 16.2 mm from the trailing edge. A detail of the cooling slots is shown in Figure 3.8.

Coolant flow enters through the side of the vane through a  $1/2''$  barbed connection and into a plenum that feeds into a thin rectangular channel with dimensions  $47.4\text{mm} \times 1.2\text{mm}$ . This can be seen in Figure 3.7. A pin fin array is placed inside the feed section to the pressure-side cutback cooling downstream of the plenum to make the film coolant flow more uniform and to represent conditions in typical vanes. The pin fin array consists of 6 staggered rows of 1.14mm-diameter pin fins. The pin fins are spaced 2.75mm apart and the separate rows are also spaced 2.75mm apart.

A 2mm-tall boundary layer trip is placed at the suction peak of the airfoil to

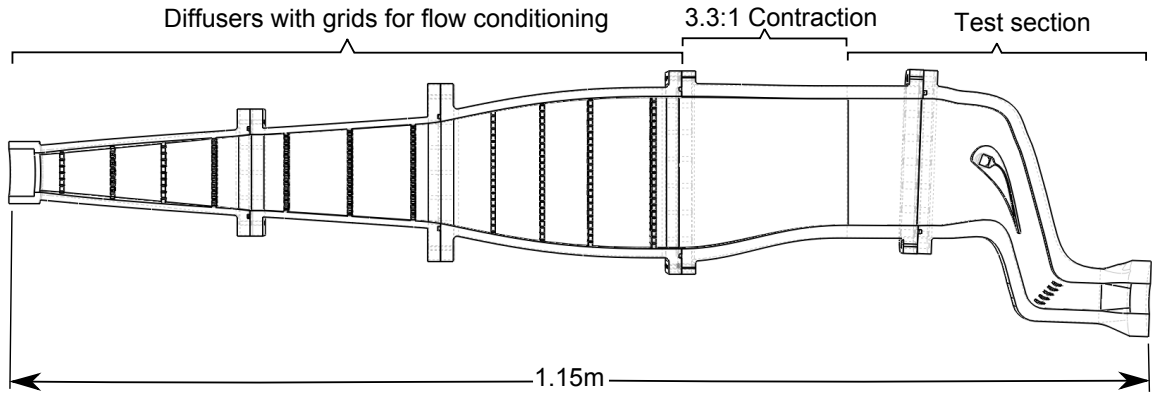


Figure 3.5: Schematic of double passage test channel. A diffusing series of flow conditioning grids connects to a nozzle with a contraction ratio of 3.3:1. The nozzle leads into the test section designed by the double passage optimization. A pressure side cutback cooling system is incorporated into the trailing edge of the vane.

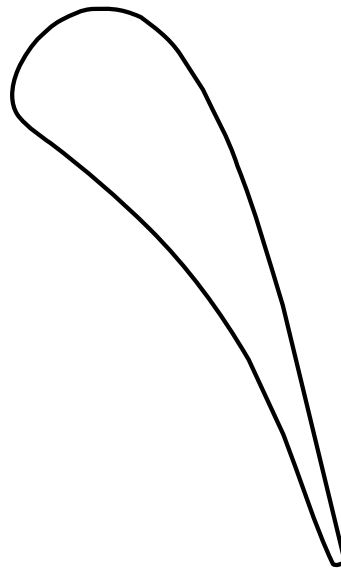


Figure 3.6: Profile of VKI vane used in double passage vane cascade experiments. The chord is 8.84 cm and span of the vane is 5.5 cm. A pressure-side cutback cooling scheme has been implemented on the vane trailing edge.

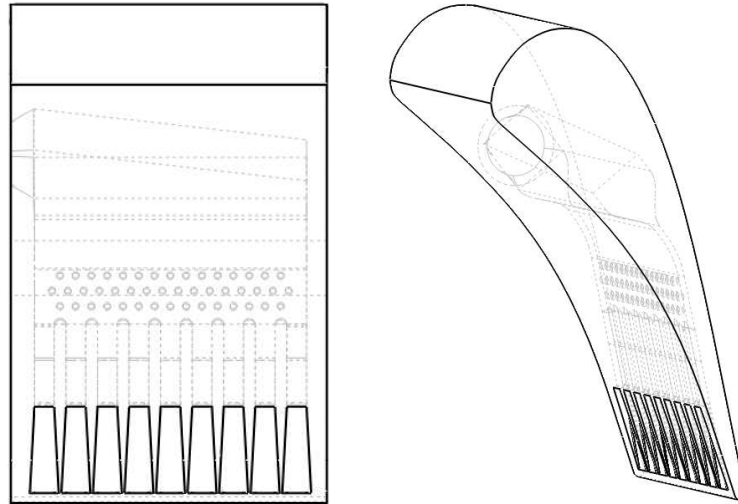


Figure 3.7: Schematic of vane and pressure-side cutback cooling and feed system. The coolant flow feeds in from the side and into a plenum. The flow is then directed through an array of pin fins and then out through pressure-side cutback cooling slots.

Table 3.1: Key airfoil and trailing edge parameters

Feature	Dimension (mm)
Chord length	88.4
Effective pitch	75.0
Span	55.6
Land width	2.06
Slot width	3.43
Slot height	1.14
Lip thickness	0.86
Breakout floor length	16.2

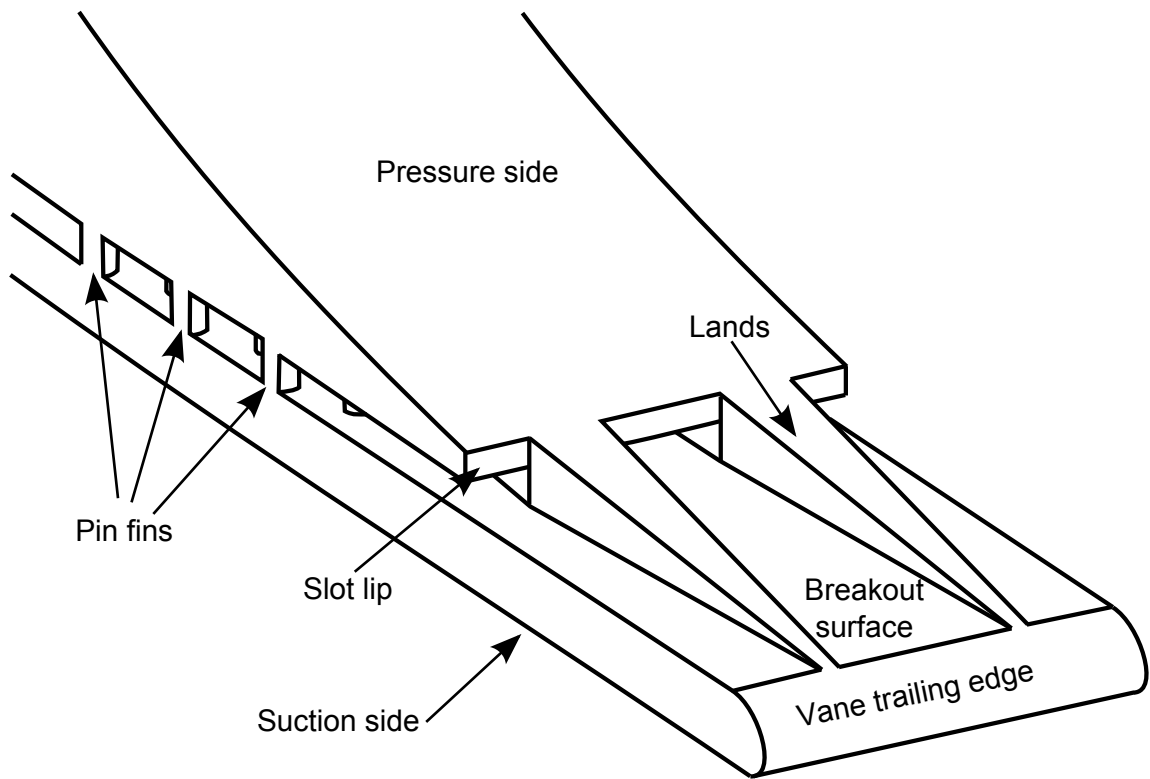


Figure 3.8: Detailed view of pressure side cutback cooling. The cutaway shows the position of the pin fin array

ensure turbulent boundary layers after it was determined that the boundary layer was transitioning from laminar to turbulent on the suction side. Real engine turbine vanes and the VKI experiments have operating Reynolds numbers higher than the ones used in the MRI experiments. The boundary layer trip is used to ensure a turbulent boundary layer to be more representative of these flows. The boundary layer trip and the addition of film cooling are both not present in the VKI experiments, so it is not expected that the experimental results from the MRI-based measurements will be in exact agreement with the VKI experiments.

The experiment is designed to run at a main flow rate of 180 liters per minute with a bulk inlet velocity of 0.43 m/s. The chord Reynolds number based on this flow is 80,000. The coolant flowrate is 1.9 liters per minute, giving a blowing ratio of 1.0. Because both the main flow and the coolant flow have a working fluid of water, the densities of the two flows are the same. The blowing ratio is traditionally defined as the ratio of the coolant momentum flux to the bulk momentum flux, but since the densities of the two fluids are the same, the blowing ratio can be defined as the ratio of the coolant velocity to the main velocity at the introduction of the coolant into the main flow on the pressure-side trailing edge. Flowmeters for the mainstream and coolant supply are continuously monitored and controlled to be within 3% of the nominal flow rate.

### **3.4 Flow loop for MRV**

MRV is run with a working fluid of 0.06M copper sulfate solution in water. A closed loop system is created using a 25 gallon reservoir. Both the main and coolant flows are fed from this reservoir. The main flow uses a Berkeley 1 hp pump (Model #BPDH10-L) in line with a 1.5" diameter Signet Scientific flow meter (Model #MK315-3PO) and flow transmitter (Model #8550) and a 1.5" diaphragm valve. The coolant line

uses a 1/2 hp Little Giant pump (Model #TE-6-MD-HC), a Blue-White Industries flowmeter (Model #RB-375MI-GPM1) and 1/2" diaphragm valve. The main flow line enters the test channel through 1.5" diameter PVC tubing. The coolant flow line uses 1/2" diameter tubing. The flow exits the channel through 1.5" diameter PVC tubing and returns the flow to the copper sulfate reservoir. A schematic of this setup is presented in Figure 3.9 and a photograph of the system set up in a magnet suite is shown in Figure 3.10.

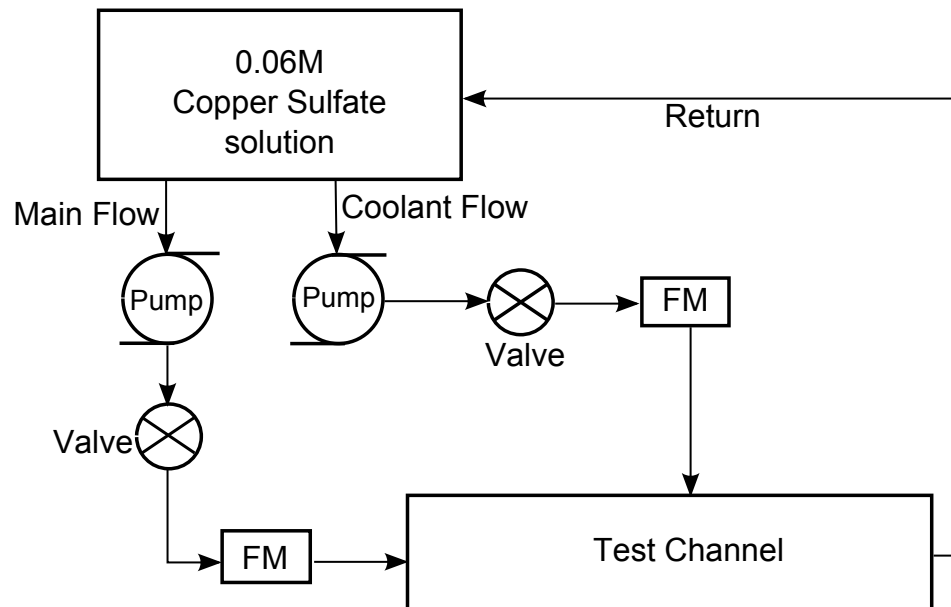


Figure 3.9: Schematic for flow loop for MRV. “FM” depicts the position of a flowmeter inside the flow loop. All equipment depicted in this figure is located inside the magnet room during an MRV scan. A closed loop system is created with 0.06M copper sulfate solution as the working fluid.

### 3.5 Flow loop for MRC

The MRC experimental flow loop uses much of the same equipment as the MRV. The pumps, valves, flowmeters, and tubing used in the MRV setup are all used in the same roles in the MRC setup. In an MRC, four different types of scans are conducted, as



Figure 3.10: 3T1 Magnet Suite at Richard M. Lucas Center for Imaging, Stanford University. The test channel is inside the transmit-receive head coil inside the bore of the magnet. A 25 gallon tank full of 0.06M copper sulfate solution completes a closed loop system of pumps, valves, and flowmeters to recirculate the working fluid for an MRV scan.

was detailed in Chapter 2. The flow loop setup for a “reference” scan is presented in Figure 3.11. Both the main and coolant flows are fed from a 65-gallon reservoir of 0.015M copper sulfate solution (in the compressibility effects experiment detailed in Chapter 2, 0.018M copper sulfate solution is used because a linear calibration regime could be found for 0 to 0.018M copper sulfate solution in that experimental test). The return line from the test channel directs the flow back into the copper sulfate tank.

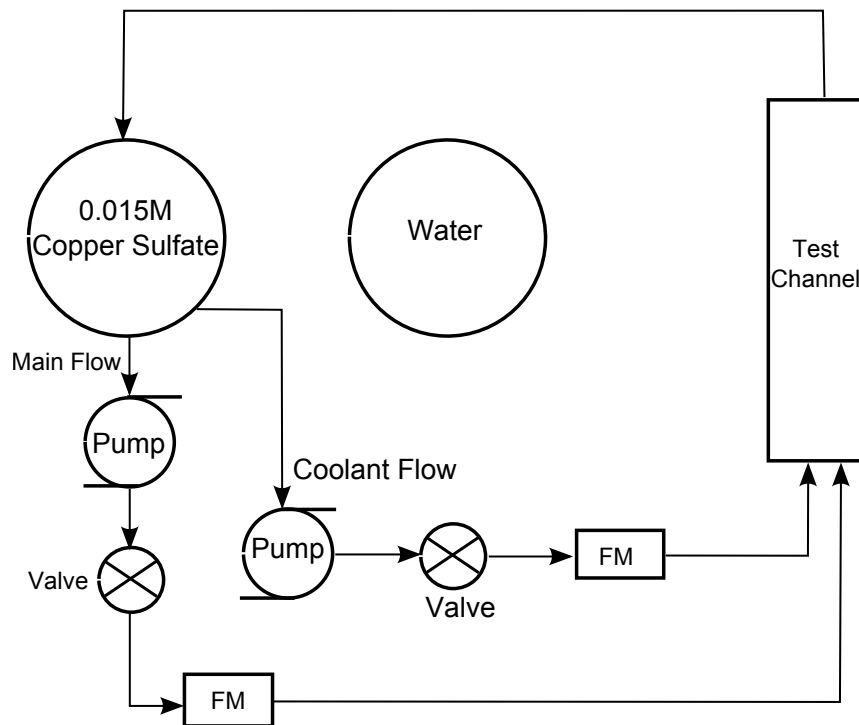


Figure 3.11: Schematic for flow loop for “reference” runs. All of the equipment in this schematic creates a closed loop system inside the magnet room. The test channel sits inside the bore of the magnet.

A “background” run has the same experimental setup as the “reference” runs, with one major difference. The main and coolant flows are fed from a 165-gallon water reservoir, and the return line connects to this same tank, making a closed loop system with water as the working fluid. This schematic is shown in Figure 3.12.

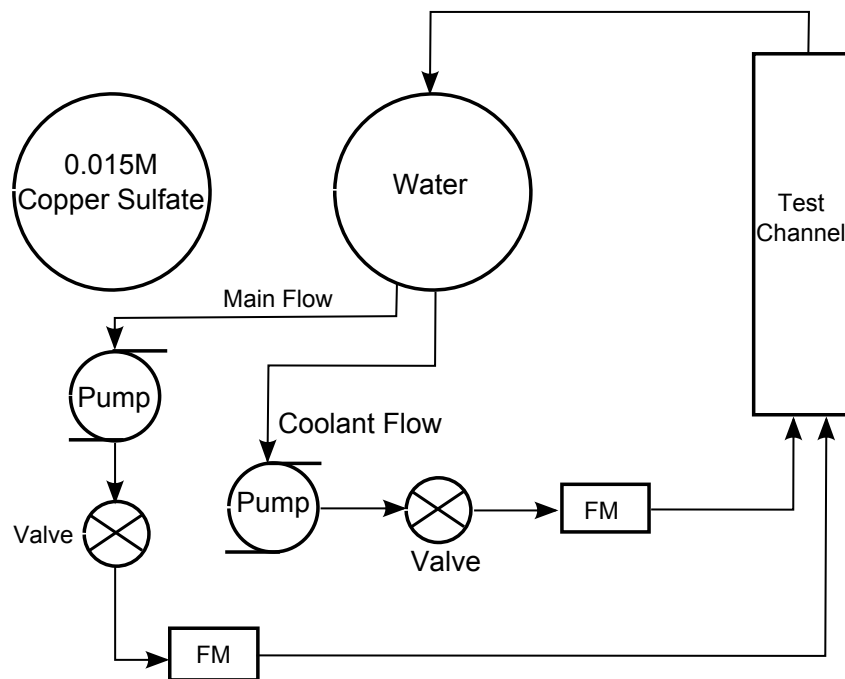


Figure 3.12: Schematic for flow loop for “background” runs. Both the main and coolant flows are fed from the water reservoir.

In an “inverted” run (see Figure 3.13), the main flow is fed from the 0.015M copper sulfate solution, while the coolant flow is fed from the water reservoir. The return line from the test channel is connected to the 0.015M copper sulfate tank. Because the water dilutes the 0.015M copper sulfate solution slightly, a higher concentration 0.08M copper sulfate solution follows a pump, valve, and flowmeter system to the 0.015M copper sulfate reservoir. This flow is carefully metered to ensure that the 0.015M concentration of copper sulfate is maintained in the coolant flow.

The schematic for a “standard” run is presented in Figure 3.14. In a “standard” run, the main flow is fed from a 165 gallon reservoir. This reservoir is connected a large outdoor water reservoir that holds 1650 gallons of fresh water. Clean water from the outdoor reservoir is directed into the 165-gallon tank inside the magnet room. The coolant flow is fed from the 0.015M copper sulfate reservoir. The flow from the exit of the test channel returns to a second 165 gallon reservoir. A pump system directs

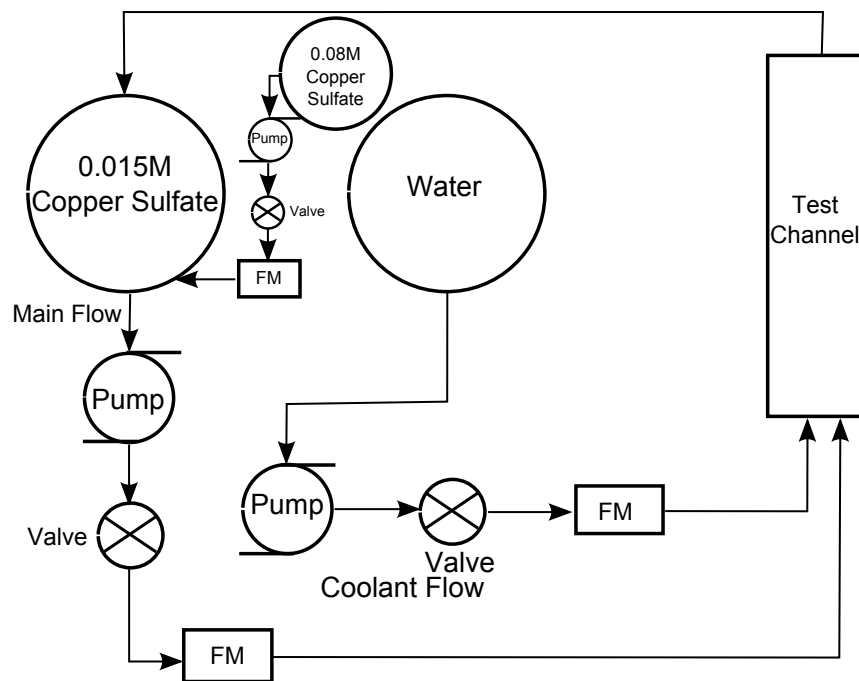


Figure 3.13: Schematic for flow loop for “inverted” runs. Main flow is fed from the 0.015M copper sulfate reservoir, while coolant flow is fed from the water reservoir. A “make-up” line of high concentration (0.08M) copper sulfate is used to maintain 0.015M concentration in the coolant flow.

water from this second reservoir to the outdoor water reservoir. Because of the large capacity of the outdoor reservoir, the contamination of the water (with copper sulfate) remains low and allows for the necessary number of “standard” runs to be completed.

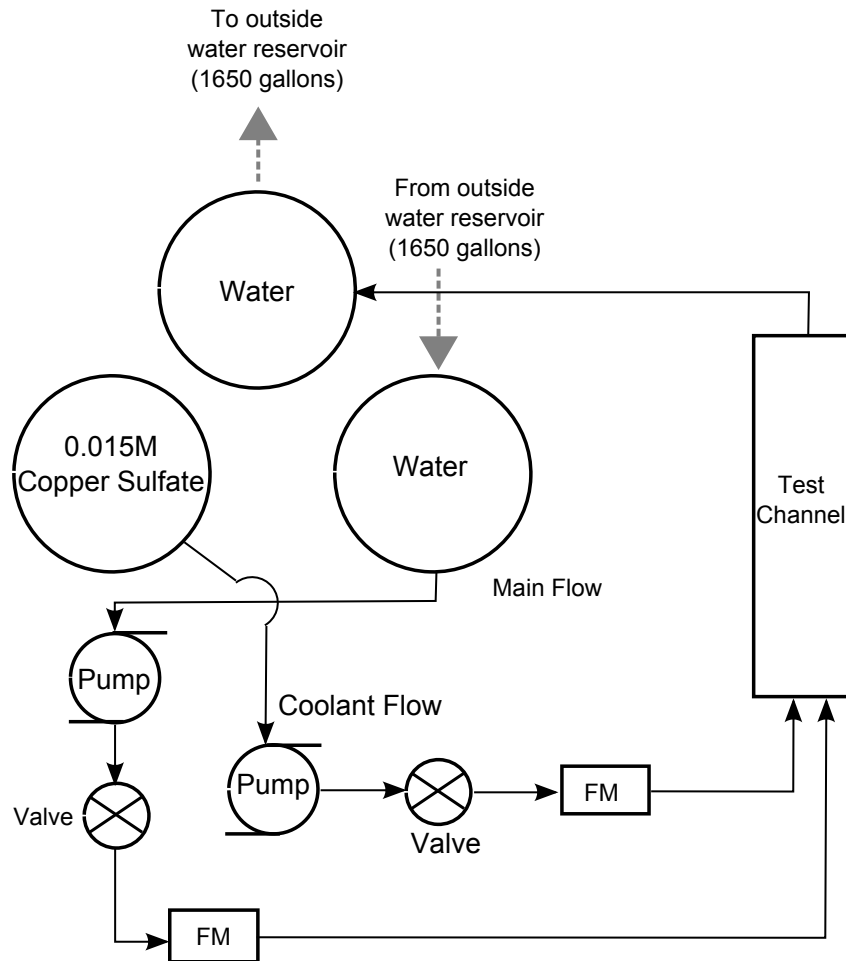


Figure 3.14: Schematic for flow loop for “standard” runs. Main flow is fed from a 165-gallon water tank into which water is pumped from the outside reservoir. Coolant flow is fed from the 0.015M copper sulfate reservoir. The flow exiting the test channel returns to a second water tank from which water is pumped to the large outdoor reservoir. In this way, contamination of the main flow is kept as low as possible over the course of the “standard” runs.

### 3.6 Limitations due to Magnetic Field

The magnetic field of the MRI machine causes many limitations for design and fabrication of the experimental setup. All objects that will be placed in the bore of the magnet for MR measurements must be strictly non-magnetic. This means that many metals are cannot be used and that extreme caution has to be taken with equipment that is not made in-house. The materials that are used for the test channel are predominantly plastic, with neoprene used for o-rings and nylon or brass screws. Some Teflon tape is used for sealing threaded connections. Pumps and flowmeters with metal components are used inside the magnet room, but outside of the bore of the magnet as part of the flow loop. Since the strength of the magnetic field decays as  $r^2$  (where  $r$  is the distance from the center of the magnetic field), the strength of the magnetic field is much weaker than its maximum strength even 3 feet away from the center of the magnet. Therefore, great care is taken to place these pieces of equipment as far away as possible from the center of the magnetic field.

# Chapter 4

## Results from Double Passage Experiments

*This chapter includes excerpts from a manuscript accepted to the 2014 ASME International Gas Turbine Institute Conference cited as Yapa SD, Elkins CJ, Eaton JK (2014). “Endwall vortex effects on turbulent dispersion of film coolant in a turbine vane cascade”. Proceedings of ASME Turbo Expo 2014 (GT2014-25484).*

### 4.1 Development of the Passage Vortex

The secondary flows present in turbine vane cascades have been studied for many years. As was discussed in Chapter 1, it is commonly acknowledged that the presence of the passage vortex, which forms in the corner between the endwall and the suction surface of the airfoil, plays a key role in developing the flow features which contribute to the non-uniform mixing of film cooling near the trailing edge of the vane. Studies performed to date agree that the horseshoe vortex that forms at the intersection of the vane leading edge and endwall creates pressure- and suction-side legs that divide into adjacent passages. The various studies, disagree, however, on the behavior of the

suction-side leg of the horseshoe vortex as it interacts with the passage vortex.

In any case, the strong secondary motion has a significant effect on thermal transport. For example, Kang et al. [30] found using infrared camera measurement techniques that the Stanton number is highest very close to the vane surface on the pressure side, about a quarter of the chord length downstream of the leading edge, where secondary flows force mainstream fluid close to the endwall. On the suction side, the Stanton number is found to be at a minimum where the suction-side leg of the horseshoe vortex meets the passage vortex. The upward turning of the passage vortex as it moves downstream corresponds with a rapid increase in the Stanton number.

The focus of this research is on analyzing the structure and behavior of the endwall vortex, as well as the mixing of coolant from the pressure-side cutback as it interacts with the endwall vortex. The 3D nature of the data allows for calculation and comparison of turbulent diffusion in both the endwall region and in the mid-span, as well as investigation into the impact of the endwall vortex on flow downstream of the turbine vane.

The MRV and MRC data acquisition methods and parameters are detailed in Chapter 2. Following these methods, the MRV uncertainty is determined to be 3.7% for an SNR of 23.7 for the full-field data set. An SNR of 14.9 yields an uncertainty of 4.5% for the high resolution data set. The MRC uncertainty is calculated to be 3.8% using a 95% confidence interval. Both the MRV and MRC data are acquired in such a way that the Cartesian coordinate system was aligned with the direction of the bulk inlet flow. However, the double-passage vane cascade has a turning angle of  $77^\circ$  and a cambered airfoil geometry was used. Because of this, a new streamwise direction ( $x$ ) is defined as parallel to the suction side of the trailing edge and the  $y$ -direction is defined as the direction normal to the surface of the suction side trailing edge. In this new coordinate system, the stagnation point of the vane leading edge is defined

as  $(x, y) = (0, 0)$ . The spanwise direction is defined as the  $z$ -direction, with  $z = 0$  at the center of the span. The measured data set includes all three velocity components on a uniform Cartesian mesh. The data set has been processed in various ways to illustrate the flow features.

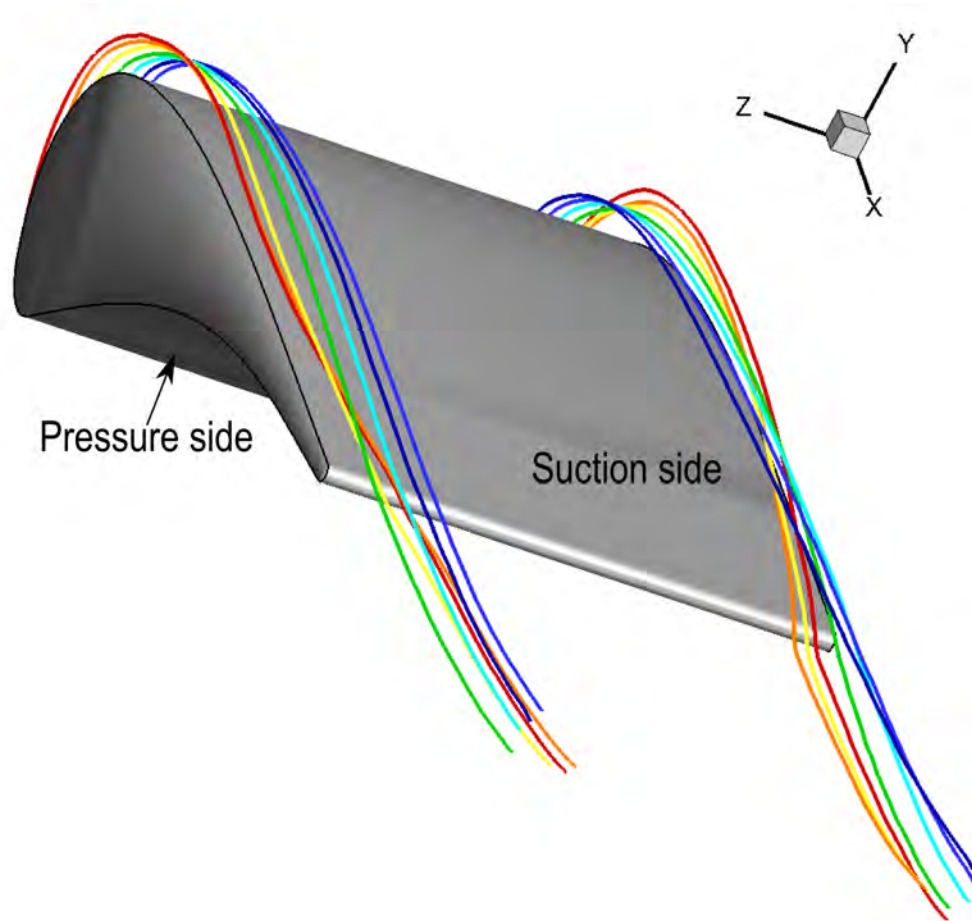
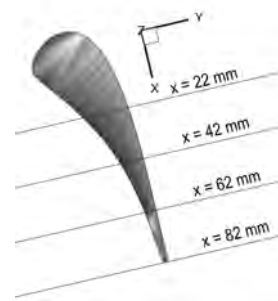


Figure 4.1: Streamlines through the endwall vortex

A set of streamlines is computed using the full-field MRV data beginning along two spanwise line segments upstream of the leading edge of the vane suction side to show the qualitative behavior of the passage vortex. Figure 4.1 shows that the suction leg of the leading edge horseshoe vortex on the left rotates in a counter-clockwise direction

as it evolves into the passage vortex, agreeing with the results of both Sieverding [55] and Langston [36]. The streamlines are equally spaced at the vane leading edge and the colors were chosen to show matching spanwise locations, e.g. red on the left and on the right were computed beginning at  $z = \pm 25.5$  mm. Comparing the trajectories of the red and green streamlines, we see that the vortex completes approximately  $180^\circ$  of rotation as it passes along the length of the vane.

Figure 4.2 shows spanwise slices of streamwise vorticity contours, overlaid by in-plane velocity vectors. Figure 4.2(a) shows the location of each of these planes relative to the vane. At  $x = 22$  mm, there is a layer of streamwise vorticity adjacent to the endwall corresponding to crossflow in the endwall boundary layer which has the same sign as the suction side leg of the horseshoe vortex. The presence of the vane suction surface causes the cross-flow vorticity to roll up into the suction-side leg of the horseshoe vortex, as seen in Figure 4.2(b). Additionally, the pressure side leg of the horseshoe vortex is evident as the strong negative vorticity region (dark green contours) to the right of the red contours along the endwall at about the figure mid-height. Moving downstream, the pressure-side leg of the horseshoe vortex sweeps non-vortical flow towards the endwall, splitting the region of strong longitudinal vorticity in two. At  $x = 42$  mm (Figure 4.2(c)), the cross-flow boundary layer interacts with the vane suction side and rolls up into the strong passage vortex. The pressure-side leg of the horseshoe vortex starts to dissipate and grow larger in size (although weaker in streamwise vorticity magnitude). An additional 20 mm downstream, the passage vortex begins to move on the suction side towards the center of the span under the influence of its image vortex. The passage vortex has grown by nearly 50% in the spanwise direction (Figure 4.2(d)). By the trailing edge ( $x = 82$  mm), the passage vortex has grown to twice as big in the spanwise direction as at  $x = 42$  mm (Figure 4.2(e)), but the vorticity has diffused and the peak secondary velocities have dropped. The remnants of the two legs of the horseshoe vortex are becoming weak features in



(a) Locations of span-wise slices

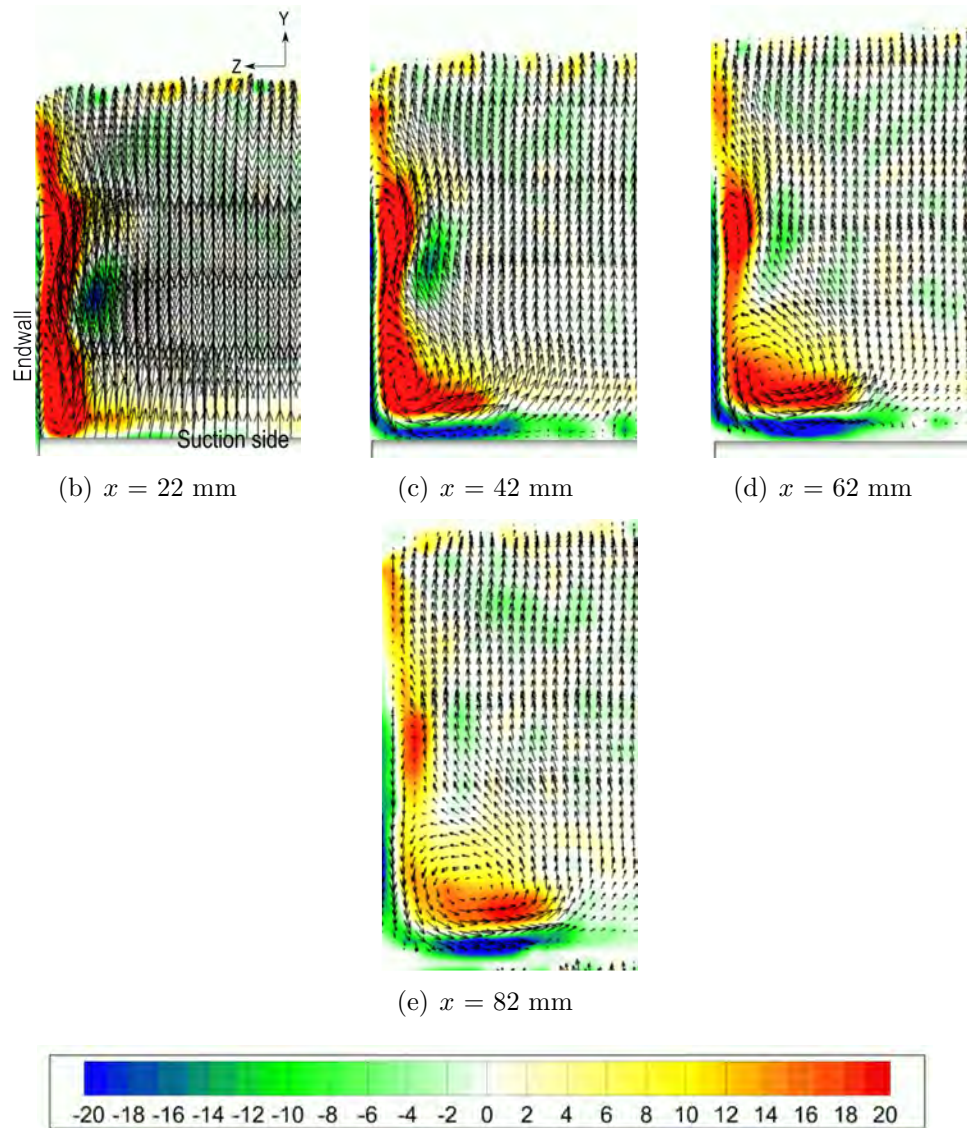


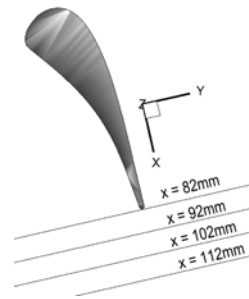
Figure 4.2: Contours of streamwise vorticity, normalized by bulk inlet velocity and vane chord. Span is from  $z = 13$  mm to  $z = 27.7$  mm in the horizontal direction

the flow. Similar plots in the wake of the vane are shown in Figure 4.3. These plots show vorticity and secondary flow features being fed from both the suction and pressure side of the vane. At the trailing edge ( $x=82$  mm), the passage vortex is still the dominant secondary flow feature. However, moving downstream into the vane wake, the passage vortex, the vorticity from the suction-side boundary layer, and the flow from the pressure side of the vane interact, and the passage vortex starts to lose its definitive shape. The peak vorticity decreases as the vortex moves downstream.

## 4.2 Concentration field in the vane wake

Dispersion of the film coolant in the vane wake and the effects of the passage vortex on this diffusion are of particular interest. Figure 4.4 shows the 12% concentration isosurface for the coolant introduced through pressure-side cutback cooling slots. This isosurface illustrates two major observations. The first is that the isosurfaces extend farther downstream in the center region than near the endwalls, indicating that coolant concentration drops more rapidly near the endwalls. Second, that the effect of the lands of the pressure side cutback create spanwise variations in the wake concentration field that persist far downstream of the vane trailing edge. Both of these effects can also be seen in Figure 4.5, which shows contours of concentration normal to the flow at streamwise locations  $x = 90$  mm,  $x = 100$  mm, and  $x = 110$  mm.

Figure 4.6 presents spanwise averaged concentration profiles across the wake at 5 streamwise locations:  $x = 90$  mm,  $x = 100$  mm,  $x = 110$  mm,  $x = 120$  mm, and  $x = 130$  mm. The averaging was done over a spanwise extent corresponding to the middle 5 coolant slots. These profiles clearly show the spreading of the concentration and the development of the wake moving downstream. The profile is quite narrow directly



(a) Locations of spanwise slices

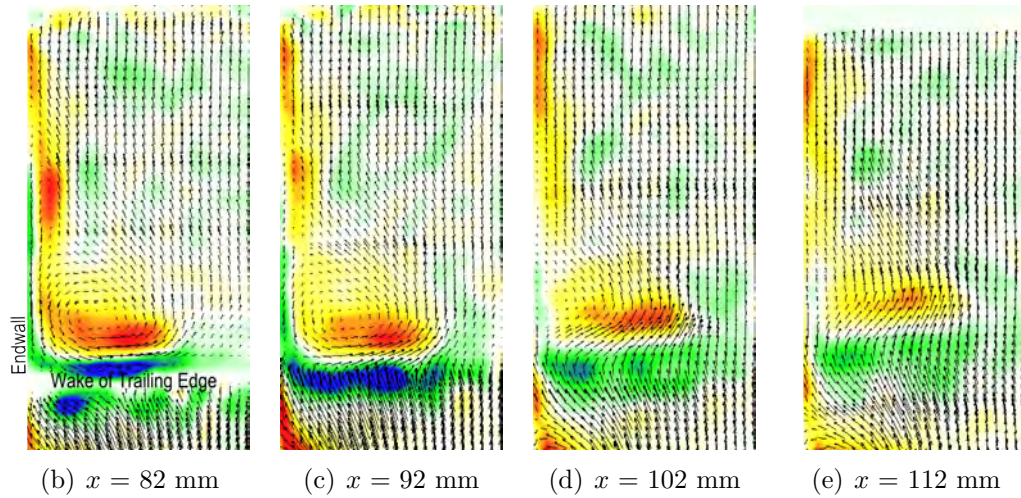


Figure 4.3: Contours of streamwise vorticity in the wake region, normalized by bulk inlet velocity and vane chord. Span is from  $z = 13\text{ mm}$  to  $z = 27.7\text{ mm}$  in the horizontal direction

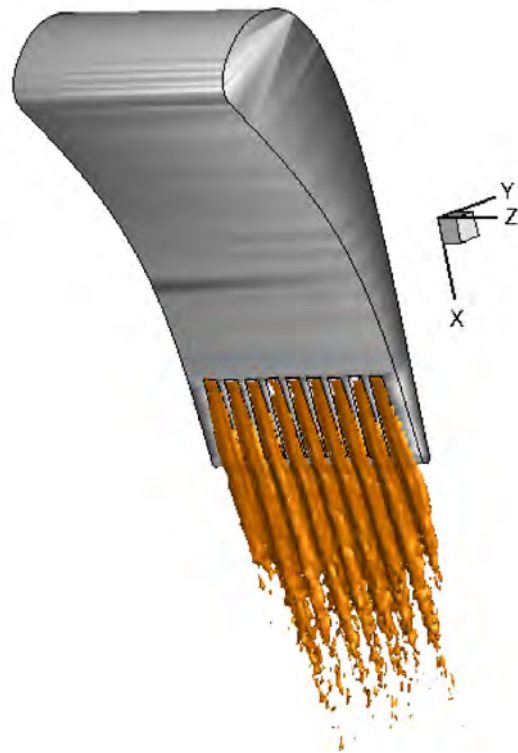


Figure 4.4: Isosurface of 12% coolant concentration

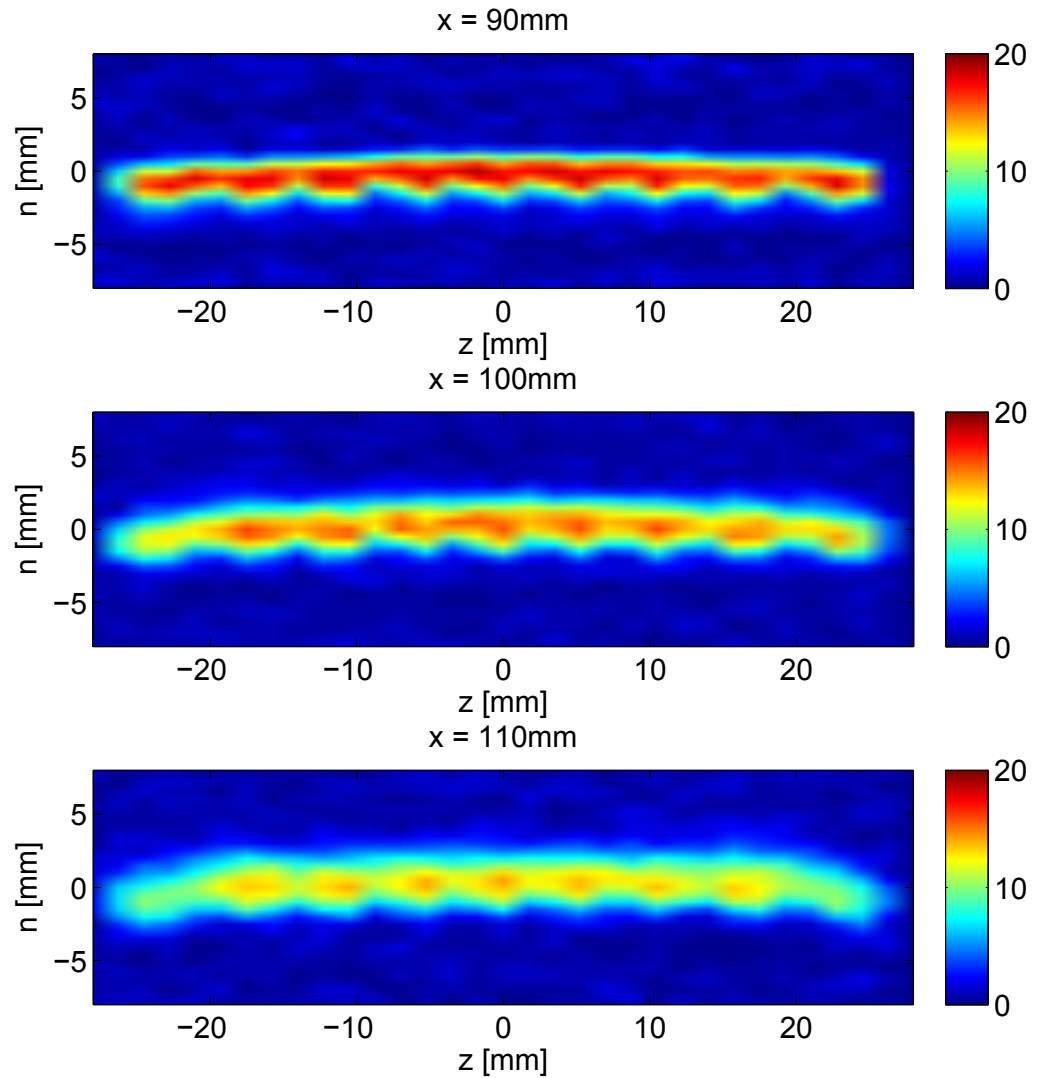


Figure 4.5: Slices of concentration contours showing spanwise variation of concentration in the vane wake. Contour levels are in percentage of the concentration injected at the trailing edge breakout.

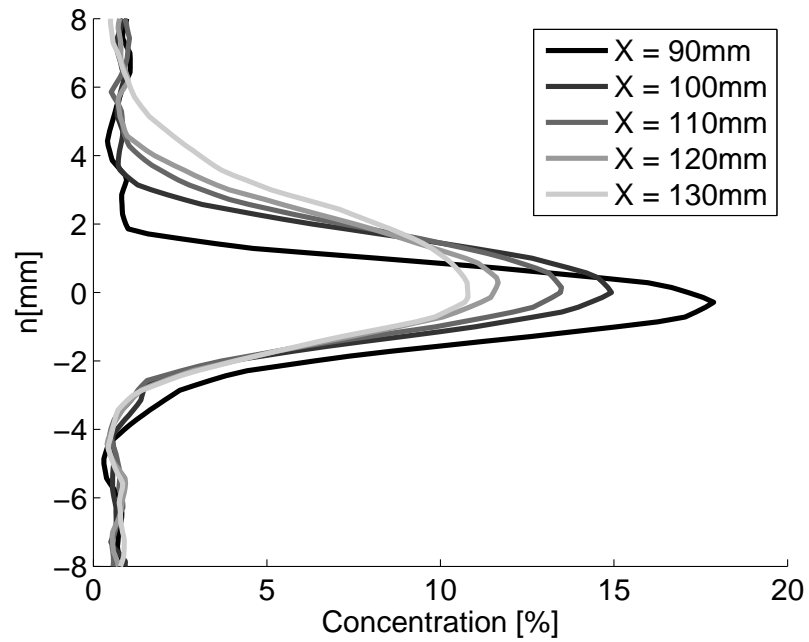


Figure 4.6: Profiles of spanwise-averaged concentration showing variation of concentration in the vane wake normal to the flow direction. Concentration levels are in percentage of the concentration injected at the trailing edge breakout

downstream of the trailing edge. The total width of the concentration peak is just over twice the trailing edge thickness at this point. Interestingly, the peak spreads much more rapidly in the positive  $n$ -direction, towards the suction side of the vane. This must be due to the combined effect of the longitudinal vortices shedding from the slots into the wake as well as the effects of the boundary layer that forms on the suction side of the vane. Ling [39] showed that slowly tapering lands such as those used in the present experiment produce longitudinal vortex pairs that move towards the airfoil suction side by mutual induction in the vane wake. These vortices carry coolant away from the wake center towards the suction side of the vane.

The strong variation of the coolant concentration across the vane wake (in the  $n$ -direction) is not very important for the turbine application. The rotating blades behind the vane row sweep through the wake in this direction so they essentially see the circumferentially averaged temperature. However, spanwise variations in the temperature are important because they create a spanwise variation in the heat load on the turbine blades. This variability is not averaged out by the motion of the turbine blades relative to the nozzle vanes. Figure 4.5 shows that spanwise variations in coolant concentration are significant in the wake and are not entirely washed away by either secondary flows or turbulent diffusion. The contour plot for  $z = 110$  mm in Figure 4.5 shows that there remains significant spanwise variability in the coolant concentration in the central region of the passage. However, the variability decays near the endwalls, most likely due to the effects of the passage vortex. It should be noted though that coolant is not released directly next to the endwall due to the design of the pressure side cutback. As can be seen from Figure 3.7, the breakout surfaces over which coolant is injected into the flow do not extend all the way to the endwall, so this also contributes to the lower concentration near the wall.

To quantify the variability in the central region of the span, the data were averaged in  $n$  across the wake. This averaging was done in a thin layer aligned with the

center of the concentration wake,  $-0.5 < n < 0.5$  mm. Figure 4.7 shows these data plotted vs. the spanwise coordinate  $z$  over the extent of the middle 5 slots. A nearly periodic variation in coolant concentration is observed. The variability is already evident shortly downstream of the trailing edge ( $x = 90$  mm) although the periodic nature of the variation is not immediately apparent. However, by  $x = 100$  mm, a quite periodic variation has emerged with a peak to peak amplitude of more than 5% in concentration. It is interesting to see that this amplitude has grown relative to  $x = 90$  mm. This is most likely caused by the integrated effects of longitudinal vortices trailing downstream from the lands dividing the coolant slots [2]. This effect of intensifying spanwise variation is also apparent in Figure 4.5. A peak to peak concentration variation of 5% may seem small at first glance, until one considers that there can be a mainstream to coolant temperature difference greater than  $600^{\circ}\text{C}$  in high performance engines.

To study the turbulent diffusion of the coolant, streamtubes are calculated at two locations in the vane wake using the measured velocity field. Each streamtube begins as a 6-mm diameter (3 trailing edge thicknesses) circle perpendicular to the  $x$ -coordinate and 8 mm downstream of the trailing edge. The streamtubes are shown in Figure 4.8, with contour slices of measured coolant concentration plotted inside at selected planes. The concentration inside the streamtubes drops rapidly. The starting locations of the streamtubes are detailed in Figure 4.9. The streamtube initiated at the vane midspan (Figure 4.8(a)) remains nearly circular going downstream. By contrast, the streamtube near the endwall (Figure 4.8(b)) is distorted into a kidney shape by the passage vortex. The distortion of the streamtube increases the perimeter surface area exposed to turbulent diffusion. The closed contour at the last measurement plane for the midspan location has a circumference of 17.3 mm, while the contour length at the equivalent streamwise position for the endwall is 21.5 mm. In contrast, the cross-sectional area decreases by 7% between  $x = 90$  mm and  $x = 130$  mm for

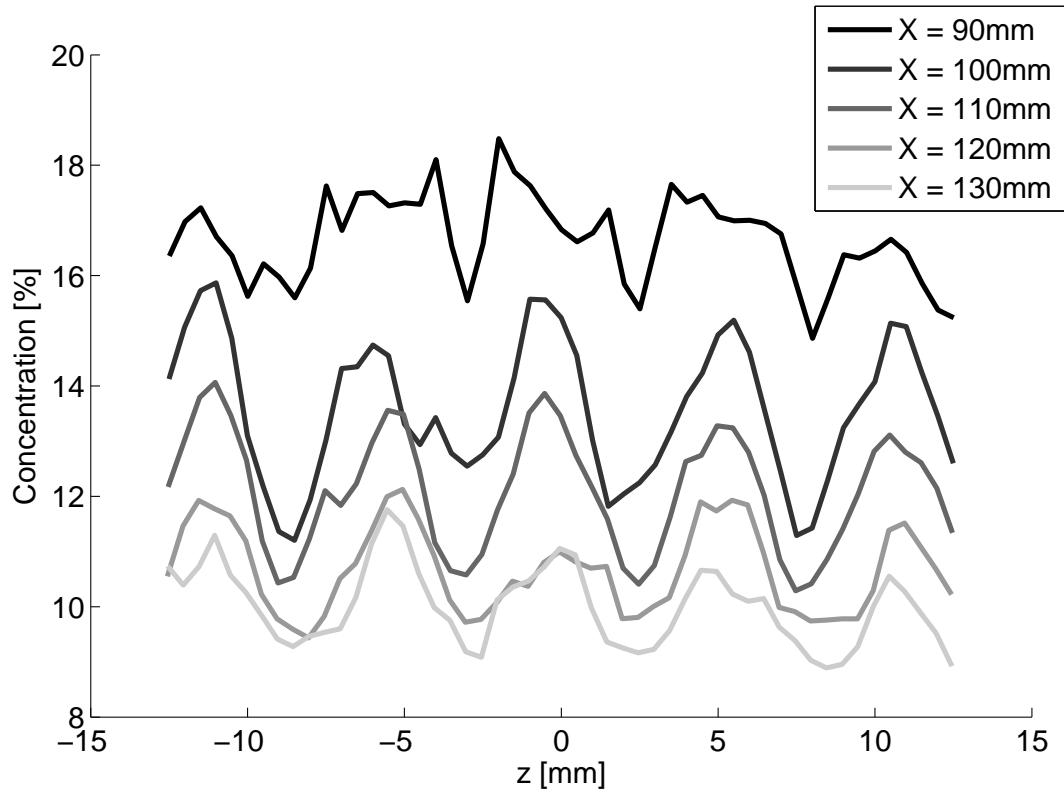


Figure 4.7: Concentration profiles are plotted against the spanwise direction for  $x = 90$  mm,  $x = 100$  mm,  $x = 110$  mm,  $x = 120$  mm, and  $x = 130$  mm . These streamwise locations correspond to  $0.09 \times C$ ,  $0.2 \times C$ ,  $0.3 \times C$ ,  $0.4 \times C$  and  $0.55 \times C$  downstream of the trailing edge, respectively, where  $C$  is the chord length (88 mm). A 1 mm-high region in the normal direction is averaged in the n-direction to get the mean concentration. Concentration levels are in percentage of the concentration injected at the trailing edge breakout

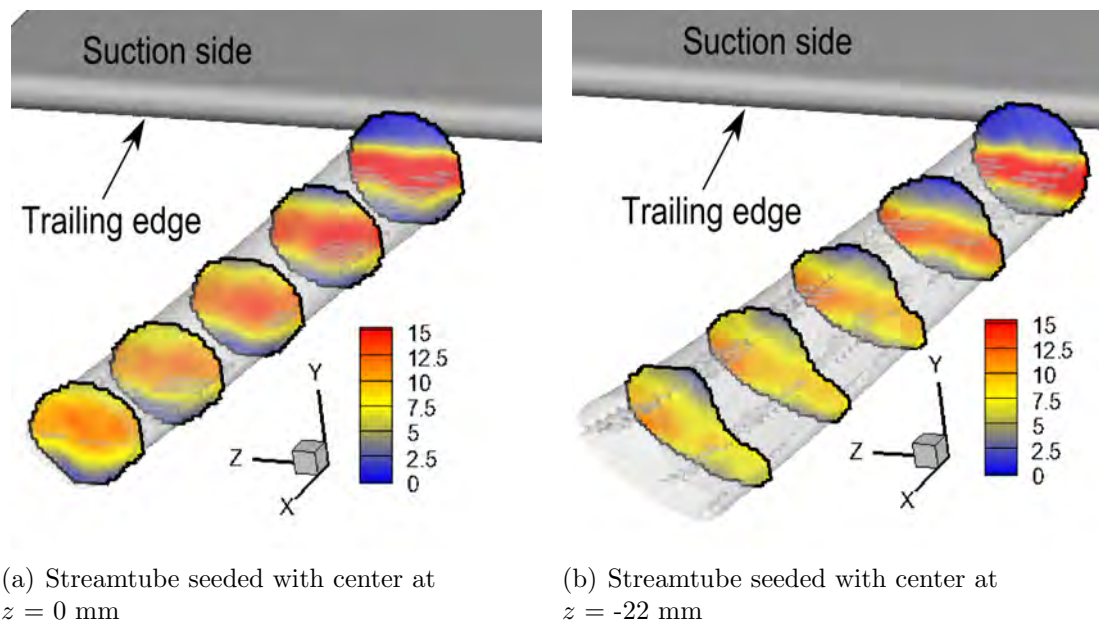


Figure 4.8: Streamtubes with contours of concentration at  $x = 90, 100, 110, 120, 130$  mm

the endwall streamtube, while it decreases by 16% for the center streamtube. This is due to the acceleration of the mean streamwise velocity as the vane wake closes. Figure 4.10 shows the evolution of the perimeter of the streamtube as it moves downstream. The streamtube perimeter is normalized by the perimeter of a circle which has the same local cross-sectional area as the streamtube. The center streamtube maintains a normalized perimeter of about 1, indicating that the streamtube, while decreasing in cross-sectional area, keeps a circular shape. The endwall streamtube, however, has an increasing normalized perimeter with streamwise position, indicating that the streamtube is being distorted out of a circular cross-section (increasing the surface area).

Further investigation into the mixing occurring in the wake can be conducted by observing two quantities in the streamtubes: peak concentration and concentration

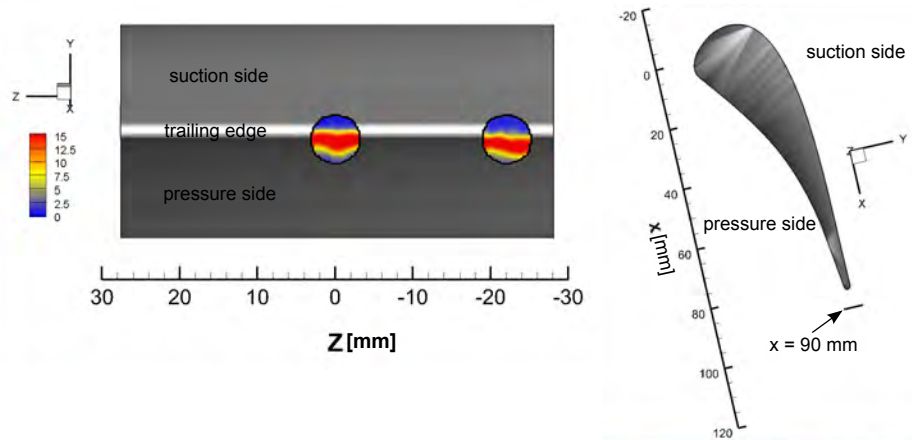


Figure 4.9: Locations of streamtubes. The image on the left shows the spanwise locations of the center and endwall streamtubes, located at  $z = 0$  mm and  $z = -22$  mm. Each streamtube is seeded with a circular cross-section. The viewer is oriented such that they are looking upstream at the trailing edge of the vane with the suction side on top and the pressure on the bottom. The image on the right shows the location of the beginning of the streamtube at  $x = 90$  mm for both streamtubes. The contours plotted are contours of concentration.

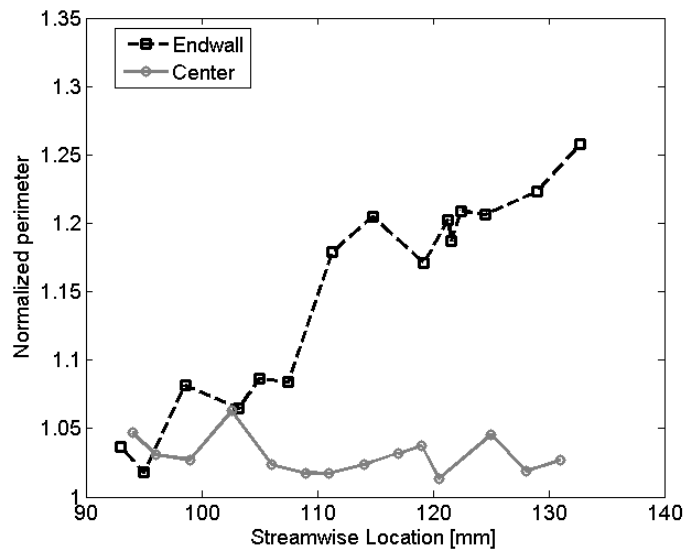


Figure 4.10: Evolution of perimeter of streamtube with streamwise position, normalized by the perimeter of a circle with the same cross-sectional area as the streamtube

transport. The peak concentration inside each streamtube is plotted against streamwise ( $x$ ) location in Figure 4.11. After looking at the MRV velocity field behavior in the center and endwall regions, it was hypothesized that the concentration in the endwall region would fall more rapidly than the concentration in the center region, due to the direct effects of the strong secondary flows in the endwall region. Furthermore, it seemed likely that the secondary flows would cause higher turbulence levels that would affect the mixing in the endwall region. It can be inferred after looking at Figure 4.11 that while the center streamtube starts out with a higher peak concentration value than the endwall region, the rate of peak concentration decrease with  $x$  is essentially the same for both streamtubes. It can also be observed that while the peak, minimum, and average concentrations in each streamtube decrease with increasing downstream position, the difference between the local maximum and minimum concentrations in each streamtube also decreases. This indicates that the concentration in the streamtube becomes more homogeneous as it travels downstream. It should be noted that the coolant in the pressure side cutback is injected at 100% concentration. The strong secondary flows and mixing on the breakout surface cause the coolant concentration to drop rapidly immediately after injection due to the counter-rotating vortex pairs that exist as a result of the lands and breakout surfaces [2, 39]. However, this behavior is not maintained into the wake of the vane.

A different look at the turbulent mixing in the wake can be achieved by determining the transport of concentration through streamtubes. New streamtubes were defined with initial diameters of 3 mm, originating from 2.5 mm downstream of the trailing edge at two spanwise locations:  $z = 0$  (center streamtube) and  $z = -22$  mm (endwall streamtube). A smaller streamtube was used for this analysis because the larger streamtubes presented in Figure 4.8 contained regions with zero concentration above and below the concentrated band of coolant. Substantial turbulent diffusion

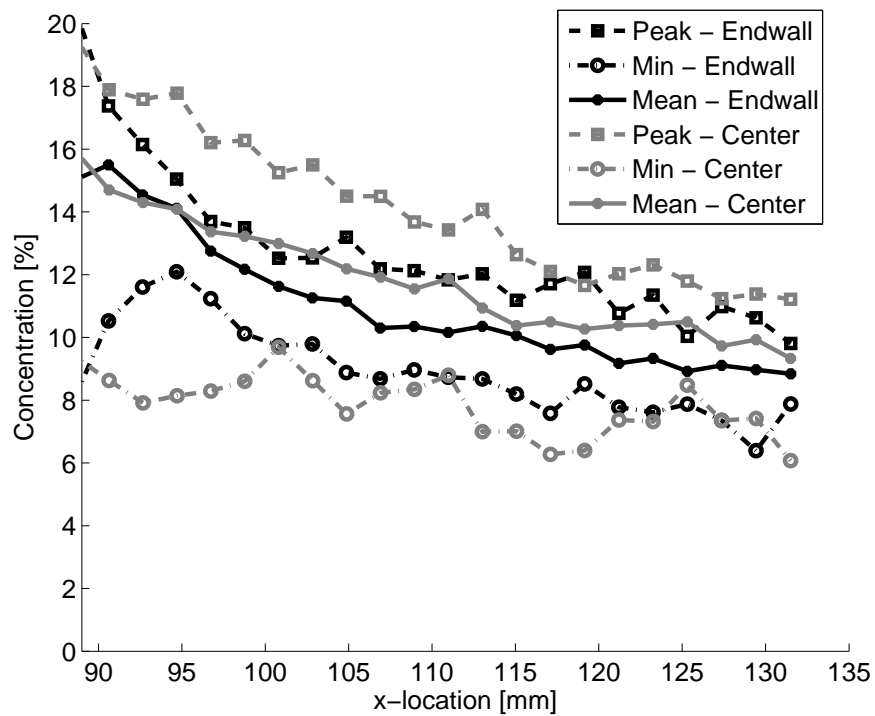


Figure 4.11: Peak, minimum, and average concentration in the center and endwall streamtubes for  $90 < x < 130$ . Planes normal to the direction of flow are extracted and the peak, minimum, and maximum concentrations are found for each location.

into these initially clear regions would not result in any loss of coolant concentration from the streamtube. The Reynolds-averaged advection-diffusion equation is presented in Equation 4.1.

$$\int_A \bar{c}\bar{u} \cdot dA = \int_V \alpha_t \nabla^2 \bar{c} dV \quad (4.1)$$

Another (equivalent) version of Equation 4.1 is presented in Equation 4.2:

$$\frac{d}{dx} \int_A \bar{c}\bar{u} \cdot dA = \alpha_t \int_{A_s} \nabla^2 \bar{c} dA_s \quad (4.2)$$

where  $A$  is the local cross-sectional area of the streamtube,  $c$  is the concentration,  $u$  is the local streamwise velocity,  $\alpha_t$  is the turbulent scalar diffusivity, and  $V$  is the volume of the control volume, and  $A_s$  is the surface area of the control volume. Using control volumes defined by segmenting each streamtube, it is theoretically possible to calculate  $\alpha_t$ , the turbulent diffusivity given that all other quantities in the equation are provided by MRV/MRC experimental data (a three dimensional flow field with a geometrically matched concentration field). However, the integral term on the right hand side of Equation 4.1 involves the integration of experimental data over the control volume,  $V$ . Because this involves the calculation of concentration flux through the streamtube surface, a high degree of uncertainty is introduced through the integration. Previous attempts at calculating the turbulent scalar diffusivity [60] yielded a possible general increase in diffusivity value with downstream location, but the uncertainty in this calculation was so large that this conclusion was suspect. The left hand side of the equation, however, can be obtained simply by multiplying the concentration and local streamwise velocity at planes orthogonal to the streamtube surface. This term is called the concentration transport through the streamtube. The change in concentration transport with increasing downstream location can give an estimate of the relative effects of turbulent mixing on concentration dispersion.

Because the streamtube surfaces are constructed using streamlines, no flow is advected through the surface, and any change in concentration transport is due to turbulent diffusion.

These smaller streamtubes are illustrated in Figure 4.12. Planes orthogonal to the flow direction are extracted at  $x = 90, 100, 110, 120,$  and  $130$  mm and concentration contours are plotted. As can be seen, the shape of the cross-section of the streamtube for both the center and endwall regions is generally the same for both the 6 mm-diameter and 3 mm-diameter streamtubes.

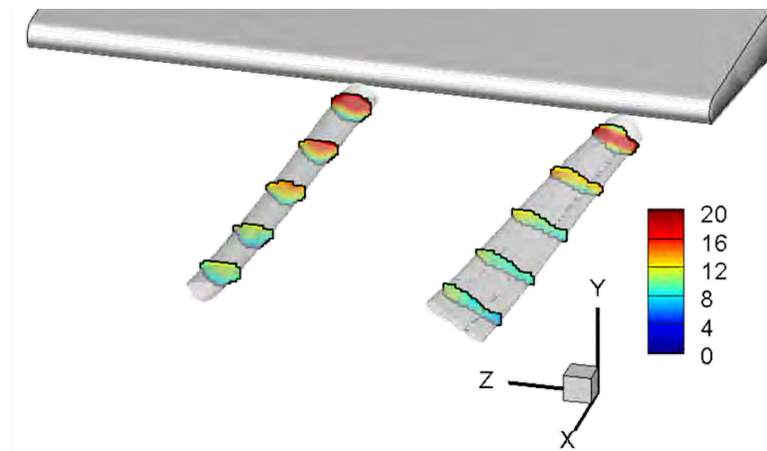


Figure 4.12: Concentration distribution in the small (3 mm-diameter) center and endwall streamtubes for  $x=90$  mm, 100 mm, 110 mm, 120 mm, and 130 mm. Planes normal to the direction of flow are extracted and the contours of concentration are found for each location inside the streamtube.

Figure 4.13 shows concentration transport for each streamtube. Given that the peak concentration in the endwall streamtube is lower than in the center streamtube at the farthest upstream wake location, it is expected that the concentration transport term will be lower in magnitude for the endwall streamtube. A further look at the streamwise velocity field inside the streamtube shows that the endwall streamtube cross-sections have significant velocity non-uniformity inside the streamtube, while

the center streamtube has a generally uniform velocity over the streamtube cross-sections. This is corroborated by Figures 4.8 and 4.10, which show that the endwall streamtube undergoes significantly more distortion than the center streamtube.

The center streamtube starts out at  $x = 90$  mm with a higher concentration transport value both because it has a higher initial concentration than the endwall streamtube and because it has a uniform flow velocity over the streamtube cross-section. The rate of decrease in concentration transport appears to remain constant with increasing  $x$ -coordinate over the entire wake region up to around  $x = 120$  mm. This suggests that the turbulent diffusion rate out of the center streamtube is nearly constant until  $x = 120$  mm. After this point, the concentration transport curve appears to flatten. The reduction in the diffusion rate could be just a consequence of the decreasing concentration within the streamtube. It might also be indicative of a reduction in turbulent activity. Figure 4.14 shows the mean streamwise velocity inside the streamtube for both streamtubes. There is significant acceleration in the wake which would be expected to reduce turbulent mixing.

The above discussion on the behavior of turbulent mixing in the wake using the streamtube analysis must be treated as tentative because of the small number of voxels present inside the 3 mm-diameter streamtubes. The uncertainty associated with these calculations is assumed to be higher than the experimental uncertainty in the concentration measurement.

The endwall streamtube initially has a lower concentration (partially due to the injection boundary condition) and also contains more non-uniformity in the streamwise velocity throughout the streamtube cross-section. Integration of the product of concentration and streamwise velocity over the streamtube cross-sectional area leads to a lower initial concentration transport quantity. This could be due to rapid initial mixing in the near field of the coolant slots and may be strongly affected by the passage vortex. From  $x = 90$  mm to  $x = 100$  mm, the change in concentration transport

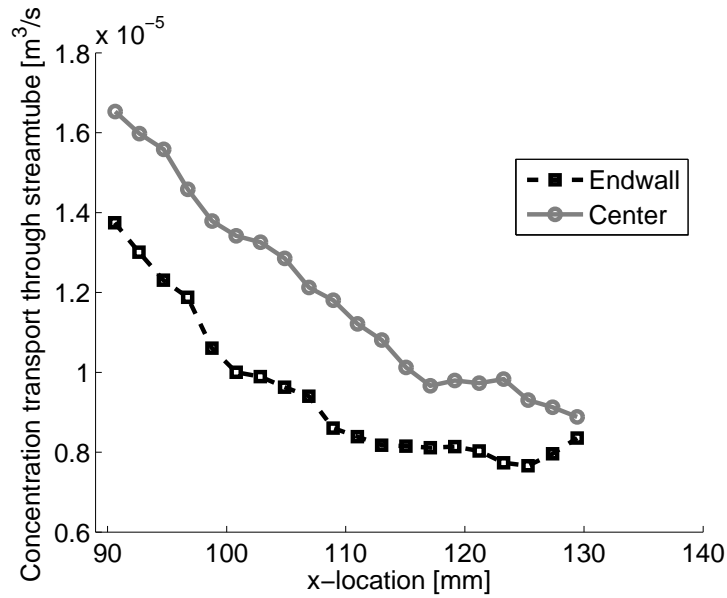


Figure 4.13: Concentration transport in center and endwall streamtubes in the wake of the vane. This quantity is the lefthand side of Equation 4.1. The effect of turbulent diffusion can be estimated by looking at the slope of the concentration transport quantities with respect to  $x$

in the endwall region has a slightly more negative slope than the center region. This indicates that the passage vortex induces slightly more turbulent mixing than in regions that do not feel the effect of the passage vortex. Additionally, the longitudinal vortices from the vane trailing edge that serve as the mixing mechanism for the center streamtube are incorporated into the passage vortex. The loss of these vortices into the endwall region may be associated with the flattening of the concentration transport for  $x > 110\text{mm}$  in the endwall streamtubes. The decreasing levels of vorticity in the flow in the wake were presented in Figure 4.3. The flattening of the concentration transport curve suggests that the passage vortex is no longer influencing turbulent mixing. The vortex is not creating further distortion of the streamtube and very little concentration is being dispersed through the surface of the streamtube.

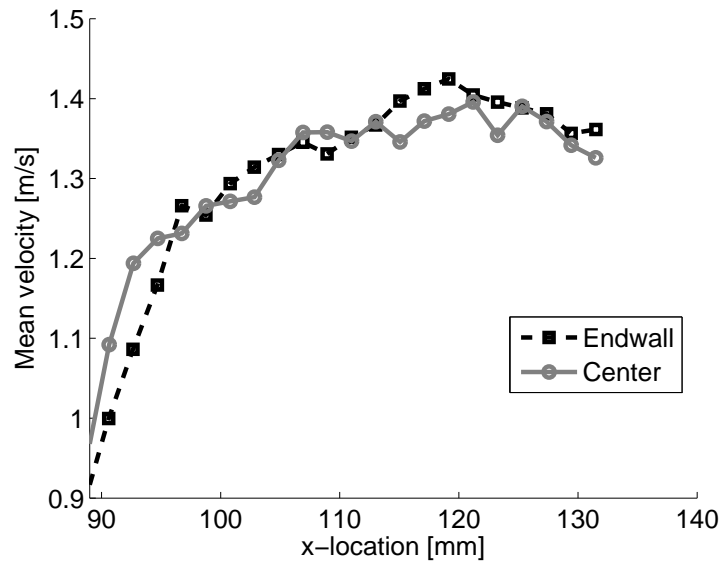


Figure 4.14: Mean streamwise velocity in center and endwall streamtubes in the wake of the vane.

### 4.3 Summary

The nature of the passage vortex present in real 3D turbine flows and its effects on turbulent coolant dispersion, were investigated. The leading edge of the vane suction surface causes transverse vorticity on the endwall to roll up and form the horseshoe vortex. The suction leg of this vortex rolls up longitudinal vorticity on the endwall and grows into the passage vortex. Moving downstream, the pressure-side leg of the horseshoe vortex splits the layer of longitudinal vorticity in two. The passage vortex grows in the spanwise direction and diminishes in magnitude. It also causes the concentration in the endwall region to be less than in the center region of the span (although the concentration is also lower in the endwall region due to the pressure-side cutback geometry). The effect of turbulent scalar diffusion was estimated in the vane wake for both the endwall region and the midspan. This analysis shows that turbulent diffusion is the dominant mixing mechanism for the center region. The

strong secondary flows caused by the passage vortex in the wake cause rapid mixing of film coolant with the main flow in the near wake of the vane. In the far wake, the effects of the passage vortex on mixing in the endwall region are diminished and turbulent diffusion dominates as a mixing method on the same scale as mixing in the center region. Concentration non-uniformities exist in both the normal direction to the vane suction side and spanwise direction throughout the wake, indicating that non-uniform inlet conditions should be applied to thermal analysis of the next row of turbine components. Peak coolant concentrations at the end of the measurement region ( $x = 130$  mm) are still approximately 10% in the endwall region and 12% near the centerspan.

# Chapter 5

## Hot Streaks Generator

## Experiments

*This chapter includes excerpts from a manuscript submitted to the 2015 ASME International Gas Turbine Institute Conference [61] cited as Yapa SD, Elkins CJ, Eaton JK (2015). “Quantitative MRI measurements of Hot Streak Development in a Turbine Vane Cascade”. Proceedings of ASME Turbo Expo 2015 (GT2015-42767).*

### 5.1 Introduction to Hot Streaks Experiments

High pressure turbine design usually assumes a uniform turbine inlet temperature. However, circumferential and radial temperature nonuniformities due to discrete fuel injection in the combustor can strongly impact turbine performance and life. Further nonuniformities may be caused by active film cooling of the combustor walls and the nozzle vanes upstream of the turbine [16, 49, 58]. These temperature nonuniformities exiting the nozzle vane row are known as hot and cold streaks. They impinge on the turbine blades and can damage them due to higher than expected peak temperatures or high metal temperature gradients.

If turbine designers were capable of predicting the strength and locations of the hot streaks, then it would be possible to optimize the high pressure turbine cooling schemes to minimize cooling flowrates while obtaining nearly uniform metal temperatures. This could improve engine efficiency while also increasing life.

A coherent set of temperature profiles representative of the hot and cold streaks exiting the combustor and leading into the high pressure turbine do not exist due to the difficulty of measurements in rotating experiments and full engine tests [49], as well as the proprietary nature of this information. Two-dimensional computational fluid dynamics simulations cannot accurately predict the highly three-dimensional nature of the hot streaks as they move through the turbine vane cascade [16]. Roback and Dring [51, 52] performed some of the first experiments on hot streaks and phantom cooling. Phantom cooling refers to the phenomenon in which coolant accumulates in various regions and creates extra cooling on the rotors downstream of the turbine vane due to the temperature nonuniformities present in the flow. In these experiments, the main objective was to study the heat transfer on the vane surface, and measurements were not taken in the vane wake. Professor David Bogard's research group at University of Texas at Austin has conducted extensive research on the topic of hot streak migration. Jenkins and Bogard [29] found that the peak temperature of the hot streak could be reduced depending on the orientation of the holes in the showerhead film cooling of the turbine vane. Additionally, an increased coolant blowing ratio causes a decrease in maximum temperature downstream of the cooled turbine vane. It was determined that the presence of film cooling significantly diminishes a hot streak impacting the stagnation line of the turbine vane. Jenkins and Bogard [27] determined that the behavior of multiple hot streaks can be represented by superposing the effects of individual hot streaks. They developed a predictive model that was based on re-scaling temperature distributions and applying superposition to predict hot streak peak temperature within  $\pm 20\%$ .

A method of predicting turbine inlet temperature distributions based on more conventional computational fluid dynamics tools would be preferred, but present models for turbulent scalar mixing are unreliable in complex flows such as through the turbine vane row. One area of concern is the dispersion of streaks that do not interact directly with the film cooled vanes. Generally, it is assumed that these streaks are diffused by the high freestream turbulence entering the nozzle row. However, Vicharelli and Eaton [59] showed that turbulence is strongly attenuated by the rapid acceleration through a stationary cascade. The effect of this on thermal streak dispersion is unknown, nor do we know the effect of complex flow structures associated with trailing edge film cooling on hot streaks passing over a vane.

The goal of this research is to provide detailed measurements of thermal streak development through a stationary cascade with geometry relevant to a typical high pressure turbine nozzle row. The experiments use Magnetic Resonance Velocimetry and Concentration (MRV/MRC) experimental techniques to provide full-field three component velocity data with a coordinate-matched scalar concentration map. These experiments are conducted in water flow with a dissolved chemical ( $\text{CuSO}_4$ ) representing temperature via the scalar transport analogy between heat and mass transfer. A streamlined hot streaks generator placed upstream of the cascade produces three streaks of  $\text{CuSO}_4$  solution arranged along the spanwise centerplane. Quantitative data on the mean distortion and turbulent diffusion of the streaks are provided as a result of these measurements.

## 5.2 Experimental Apparatus and Parameters

The experimental setup is built into a dedicated, portable water channel specifically designed for studying cooling in a turbine vane cascade. This test setup is illustrated in Figure 5.1 and is compatible with magnetic resonance-based experimental

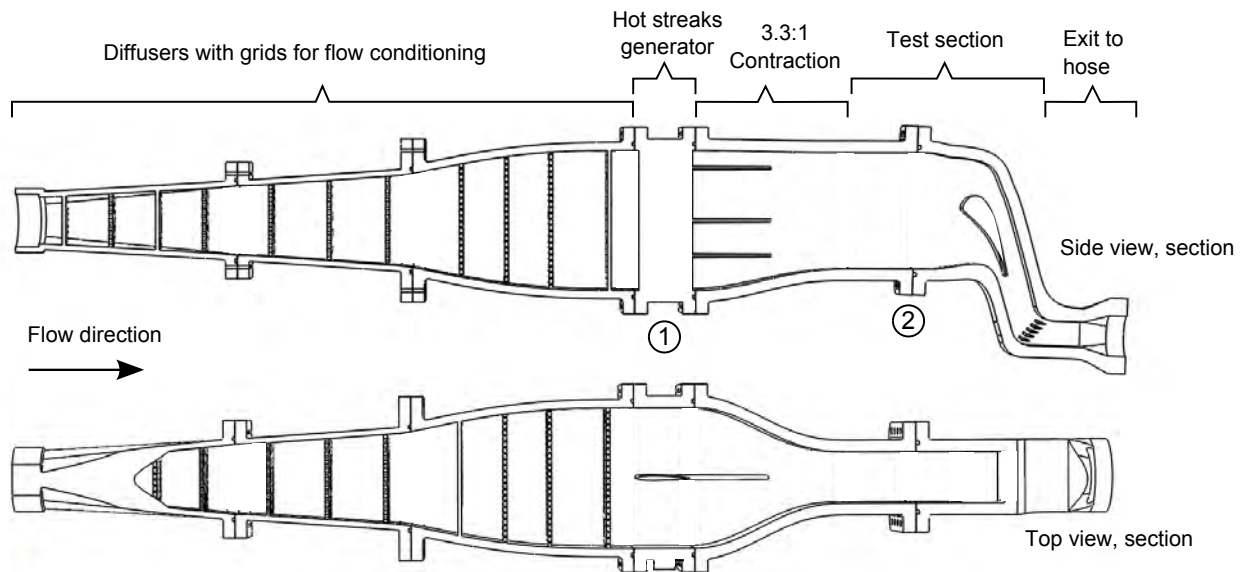


Figure 5.1: Schematic of test channel

techniques. A closed loop system is created in which water is pumped from a large reservoir of deaerated water into the test channel using a 1.5-inch diameter hose. The flow then passes through a series of three diffusers with flow conditioning grids to promote flow uniformity, with a maximum cross-section of 153 mm x 153 mm. The diffusers lead into a constant area section (section 1 in Figure 5.1) in which a NACA 0010 airfoil with a chord length of 57 mm is mounted parallel to the inlet streamwise direction. Its span is perpendicular to the span of the turbine vane in the test section. Three 87 mm long tubes are fixed onto the trailing edge of the injection airfoil at three locations along the span: 38 mm, 76 mm, and 133 mm from the bottom wall of the channel as shown in Figure 5.2. These are connected to an external coolant feed and serve as the hot streaks generator. This injection section leads into a 3.3:1 area contraction ratio nozzle which leads into the 56 mm x 126 mm inlet to the double passage vane cascade test section. The tubes extend 87 mm from the trailing edge of the injection airfoil. These correspond to a suction side injection, a stagnation line injection, and a pressure side injection with respect to the turbine vane. Each hot

streak injector has a 3 mm inner diameter with a tube wall thickness tapering from 0.8mm to to 0.3 mm at the exit.

The experimental design was centered around a main bulk flow rate of 180 liters per minute with a bulk inlet velocity of 0.43 m/s at location 2 in Figure 5.1. Based on this flow, the vane Reynolds number based on the chord is 80,000. A blowing ratio of 1.0 was used, giving a coolant flowrate of 1.9 LPM. Blowing ratio is defined as the coolant momentum flux divided by the main flow momentum flux. Water is used as the working fluid for both flows, so the blowing ratio is simply the coolant velocity divided by the main flow velocity. Flowmeters were continuously monitored and the bulk average flow controlled to maintain the blowing ratio within 3%.

The hot streak generator was designed to have an isokinetic injection. This means that the hot streaks from the three injectors are released at a bulk-averaged injection velocity of 0.24 m/s, which is the same as the average bulk main velocity at the hot streak injection point. A bulk flow of 0.3 liters per minute supplies the three hot streaks, which are individually metered to ensure isokinetic injection. The three dimensional velocity field inside the test section is unchanged from the baseline case (no hot streaks generator present), but the concentration inlet conditions are highly non-uniform. A schematic of the hot streak injectors is presented in Figure 5.2. Preliminary MRV gives a qualitative snapshot into the behavior of the velocity field at various locations. Figure 5.3 shows a slice in the spanwise centerplane ( $z=0$ ) of the streamwise ( $x$ ) velocity. The tubes from the injection airfoil extend into the contracting nozzle. The top, middle, and bottom injectors in this image correspond with the suction side, center, and pressure side hot streaks, respectively. The suction side streak injects solely in the  $x$ -direction, but the center and pressure side hot streaks experience cross-flow velocity due to the contraction in the bottom of the nozzle. This creates extra mixing of the hot streaks with the main flow. This is the main cause of the lower concentration found in the pressure side and center hot

streaks as will be discussed below. At the farthest downstream location shown in Figure 5.3, the hot streak jets create non-uniform velocity distributions in the  $y$ - and  $z$ -directions. However, this downstream location is still very close to the injection point and analysis farther downstream shows that this non-uniformity is not present at the inlet to the test section.

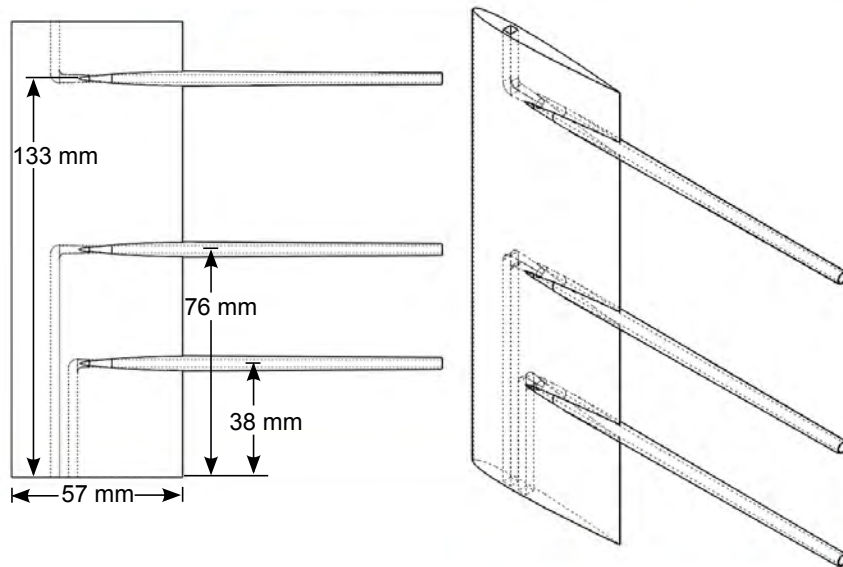


Figure 5.2: Schematic of hot streaks generator - injection airfoil and feed system

Figure 5.4 shows a velocity subtraction field for two different data sets. A spanwise centerplane contour plot has been created for the quantity  $V_{x,old} - V_{x,new}$ .  $V_{x,old}$  is the full field  $x$ -velocity for the double passage vane cascade as it was originally designed.  $V_{x,new}$  is full field  $x$ -velocity data for the test section of the hot streak generator-modified double passage vane cascade. The biggest feature of this subtracted velocity field to note is that the inlet to the test section has virtually no difference between the two data sets. This indicates that the hot streak generators present in the contraction to the test section do not alter the velocity field in any way. The largest differences in velocity are near the vane. These are not due to the velocity fields being different, but more as a result of slight spatial misregistration of the two data sets.

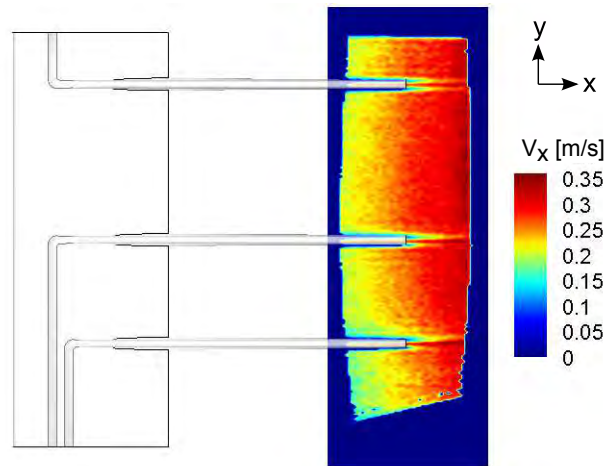


Figure 5.3: Spanwise centerplane slice of streamwise velocity contours with injector airfoil schematic for reference

## 5.3 Magnetic Resonance-based Measurement Technique

A GE 3.0T wholebody MRI scanner with a transmit-receive head coil at the Richard M. Lucas Center for Imaging at Stanford University was used to acquire Magnetic Resonance Velocimetry (MRV) and Magnetic Resonance Concentration (MRC) measurements.

### 5.3.1 Magnetic Resonance Velocimetry

The magnetic resonance velocimetry techniques used in the experiments presented in this chapter are detailed in Chapter 2. The same MRV parameters used in the double passage vane cascade experiments also are used for the hot streaks generator experiments. Just like in the double passage experiments, low and high resolution data sets were acquired to look at the full velocity field in the test section and to explore

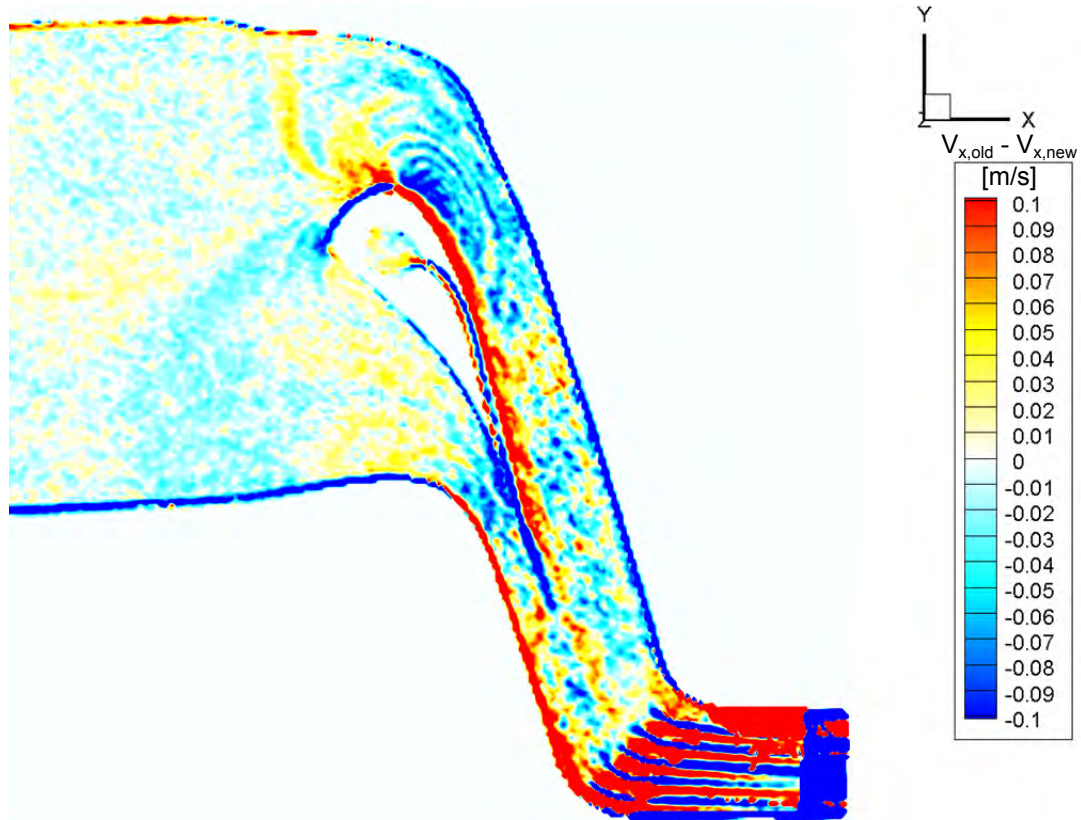


Figure 5.4: Spanwise centerplane slice of  $V_x$  velocity contours comparing test section velocity fields with and without hot streak injectors. The quantity plotted is  $V_{x,old} - V_{x,new}$ , where  $V_{x,old}$  is the  $x$ -velocity field without hot streak generators upstream of the test section and  $V_{x,new}$  is the  $x$ -velocity field with the hot streak injection airfoil and tubes placed upstream of the test section. Note that the peak velocities in this direction around the suction side are approximately 2.1 m/s. The main differences in the subtraction result from spatial misregistration of the two data sets.

detailed behavior in the wake of the trailing edge, respectively. In the fullfield data, an uncertainty of 3.6% was determined from an SNR of 17.7. In the high resolution data, an uncertainty of 3.4% was determined from an SNR of 22.1.

### 5.3.2 Magnetic Resonance Concentration

Benson et al. [3, 4, 5] and Benson [2] developed magnetic resonance concentration (MRC), an experimental technique that can measure three-dimensional scalar concentration of a contaminant (or coolant) on a three dimensional Cartesian grid. MRC experiments generally use a coolant working fluid of 0.015M copper sulfate solution in deaerated water. This is because a linear relationship between coolant concentration and MR signal magnitude exists for the concentration range 0-0.015M. However, preliminary MRC results found that a hot streak injection concentration of 0.015M led to extremely low concentrations in the test section. To counteract this, the working fluid was changed to a higher concentration of up to 0.23M copper sulfate concentration. However, this concentrated solution had a higher density than water, and experienced buoyancy effects as the hot streak traveled through the channel. Ethanol added to the copper sulfate solution matches the density of the copper sulfate solution to the main working fluid of water, eliminating buoyancy effects. Two sets of experiments were performed. In one set of experiments (hereafter called the low concentration data set), 0.02M neutrally buoyant copper sulfate solution was used in the hot streaks flow, while deaerated water was used as the working fluid in the pressure side cutback cooling and main flow. In the second set of experiments (high concentration data set), 0.08M copper sulfate solution was used in the hot streaks flow, and water was used in the coolant and main flows. The different behaviors of the three hot streaks dictated the need for two data sets. The suction side hot streak is a coherent stream of fluid that maintains its circular cross section as it passes into the test section inlet. The center and pressure side hot streaks, however, experience components of flow

perpendicular to the direction of injection due to the nozzle contraction, causing the hot streaks to mix out more quickly than the suction side hot streak. The low concentration experiments are necessary to study the suction side hot streak, while the high concentration experiments are needed to study the center and pressure side hot streaks. In the high concentration experiments, the concentration values measured in the upstream part of the test section in the suction side hot streak are outside of the linear calibration curve. Because of this, quantitative analysis of the suction side hot streak using the high concentration data is only applied in the wake of the airfoil (by this point, the concentration has diminished enough that it falls into the linear calibration regime). All upstream and full field analysis of the suction side hot streak is conducted using the low concentration data.

In these experiments, four different types of scans were conducted. These scans are known as Reference, Background, Standard (low) and Standard (high), and are described as follows:

1. Reference: 20 scans where both coolant and main flows consist of neutrally buoyant 0.015M copper sulfate, no flow through hot streaks generator
2. Background: 12 scans where both coolant and main flows consist of deaerated water, no flow through hot streaks generator
3. Standard, low concentration: 21 scans with hot streaks flows of neutrally buoyant 0.02M copper sulfate solution, main and coolant flows are deaerated water
4. Standard, high concentration: 21 scans with hot streaks flows of neutrally buoyant 0.08M copper sulfate solution, main and coolant flows are deaerated water

The SNR of the final, processed data increases with increasing number of scans. A separate calibration process is used which determines the number of individual scans needed to achieve the target SNR. The number of scans that can be achieved is limited

by both time and the amount of main flow contamination that can be sustained over the course of the data acquisition to maintain good data quality.

Two reference vials, one containing 0.015M neutrally buoyant copper sulfate solution and one containing water, are placed outside of the channel for all scans. These are used in the data processing to normalize the signal magnitude to 100% concentration at 0.015M. During data processing, each of the background scans is normalized by scaling factors determined from each individual scan and averaged to create a single averaged background scan. The same process is applied to the reference scans. Each standard run is background subtracted. In previous MRC experiments, the standard runs are normalized by the averaged reference data. However, in this case, it is hard to find an area of flow in the standard runs that is guaranteed to have 0% or 100% concentration, which are needed for the normalization process. Because of this, the two reference vials are used as a benchmark in the normalization process. The last step in the processing sequence is to normalize the concentration to be 100% in the copper sulfate vial and 0% in the water vial. All of the normalized standard runs are combined into one final averaged concentration data set. All concentrations presented in the results are expressed as a percentage of 0.015M copper sulfate solution in a solvent consisting of water and ethanol unless otherwise noted.

Variances for each scan type are calculated using a 95% confidence interval from a Student t-distribution. The variances are combined to find total point-by-point concentration uncertainty using the root-sum of squares technique as seen in Equation 5.1. The MRC uncertainty from this equation was found to be 2%.

$$\mu_c = \sqrt{\left(\mu_S \frac{\partial c}{\partial S}\right)^2 + \left(\mu_B \frac{\partial c}{\partial B}\right)^2 + \left(\mu_R \frac{\partial c}{\partial R}\right)^2} \quad (5.1)$$

An extra uncertainty is present in these experiments that is not present in most other MRC experiments. This is because the hot streak generator MRC experiments

use reference vials as part of the normalization process. There is some variation in the signal magnitude inside the reference vials. Depending on the region of interest chosen inside the reference vial, the normalized concentration value could change slightly. Using various regions of interest in the reference vials and reprocessing the data allowed for the conclusion that the selection of region of interest introduces an additional 4% uncertainty into the concentration measurements. Combining the MRC uncertainty from Equation 5.1 with this added uncertainty in a root-sum of squares method gives a total MRC uncertainty of 5%. The finite scan time (the period of time over which the flow is averaged), turbulent flow, and partial volume effects all contribute to MRC uncertainty.

## 5.4 Results

A straightforward way to understand the general, qualitative behavior of the hot streaks as they travel through the test section is by looking at concentration isosurfaces. Figure 5.5 shows concentration isosurfaces for each streak providing an overview of the streak positions and development around the vane. Prior to calculating the isosurface position, the data were normalized to the peak concentration in each streak at the inlet plane (the far left of the figure). Note that the suction side streak is narrower because the flow near the streak injector was steadier, most likely due to the lack of cross flow effects that are observed at the suction side streak “injection point”. The effect of the contraction leading into the injection section contributes to an additional cross-flow velocity which decreases the concentration of the pressure-side and center hot streaks at the inlet to the test section. The cross-flow results from the asymmetry of the contraction bending the streamlines at the locations of the lower injection sites. Figures 5.6-5.8 show 10% concentration isosurfaces for each of the hot streaks in the high concentration injection case: suction-side, center,

and pressure-side. This concentration is 10% of the reference value of 0.015M. An important observation is that the hot streaks do not mix with each other, even at the farthest downstream measurement locations. This means that in a real engine configuration, the temperature distribution of the flow that encounters the rotors downstream of the turbine nozzle vanes will certainly not be uniform. This is an important observation as uniform inlet temperature conditions often are assumed for turbine blade cooling design purposes.



Figure 5.5: Isosurfaces of 20% normalized concentration (concentration is normalized with respect to inlet concentration). The suction side hot streak is acquired from the low concentration data set, while the center and pressure side hot streaks are acquired from the high concentration data set.

Using the three-dimensional velocity field, a set of streamlines is calculated starting from points located at equal spacing around the circumference of a 12 mm diameter circle centered at the spanwise centerplane. These streamlines encompass the 10% concentration isosurface of the streak at inflow. These streamlines are then used as a basis to form the surface of a streamtube for each of the hot streaks.

Three views are presented of the suction side hot streak inside the suction side streamtube in Figure 5.6. The center and pressure side hot streaks with corresponding streamtubes are presented in Figures 5.7 and 5.8, respectively. Each of the streamtubes starts with a circular cross-section and becomes thinner in the pitchwise direction as the flow accelerates through the test section. There appears to be very little change in spanwise width of the streamtubes. The concentration isosurfaces are plotted in blue, while the streamtubes are plotted in gray. It is interesting to note that the concentration streaks remain inside the streamtubes as they pass through the cascade (although a different choice of streamtube would not necessarily contain the entire hot streak at the inlet and therefore would not contain the hot streak as it travels through the cascade). This is not a given, and different behavior has been observed in complex flows where the turbulent diffusivity is highly non-uniform or anisotropic.

The distortion of each streamtube is also indicated by a calculation of the normalized perimeter of the streamtube. The normalized perimeter analysis was first introduced by Yapa et al. [60] and is used to measure the degree to which the streamtube was convoluted by secondary flows. The normalized perimeter is defined by Equation 5.2:

$$P_{\text{norm}}(x) = \frac{P_{\text{streamtube}}(x)}{2\sqrt{\pi A_{\text{streamtube}}(x)}} \quad (5.2)$$

where  $P_{\text{norm}}$  is the normalized local perimeter,  $P_{\text{streamtube}}$  is the local perimeter of

the streamtube in planes orthogonal to the streamtube surface, and  $A_{\text{streamtube}}(x)$  is the cross-sectional area of the streamtube in the direction normal to the streamtube. By this definition, a value of  $P_{\text{norm}} = 1$  indicates that a circular cross-section is maintained, while any value above 1 indicates distortion of the streamtube due to the velocity field.

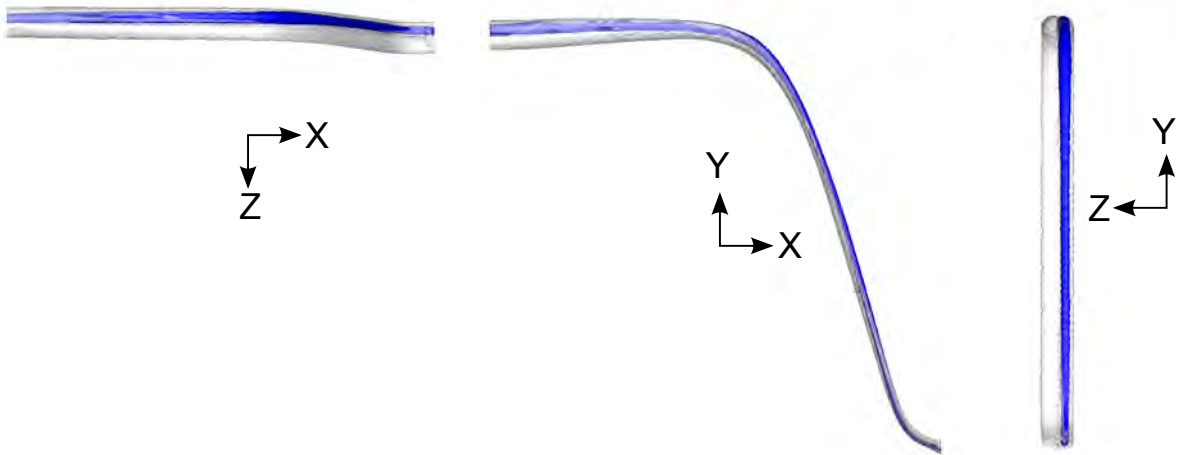


Figure 5.6: Isosurfaces of 10% concentration (blue) inside suction-side streamtube (gray) seeded with circular cross-section in three orientations

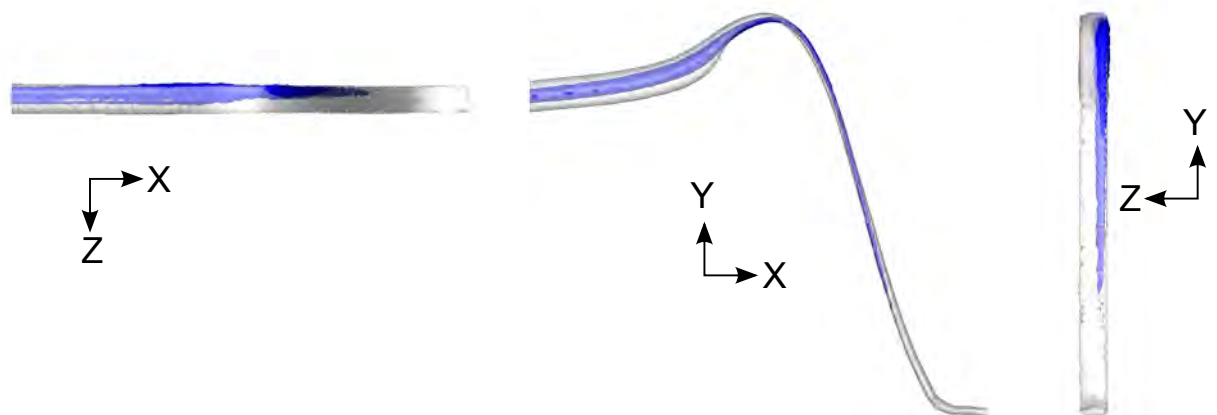


Figure 5.7: Isosurfaces of 10% concentration (blue) inside center region streamtube (gray) seeded with circular cross-section in three orientations

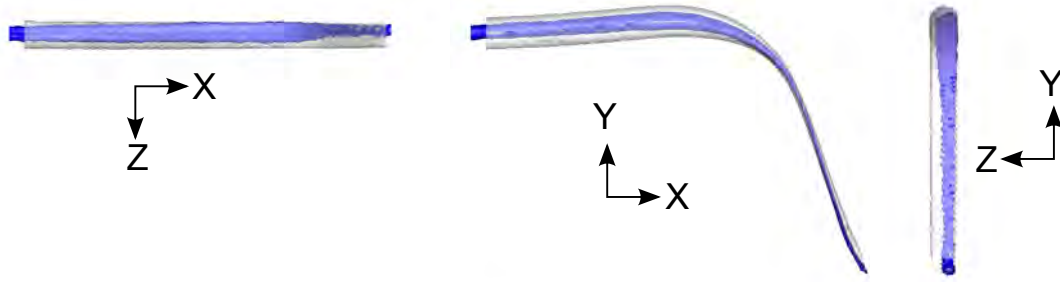
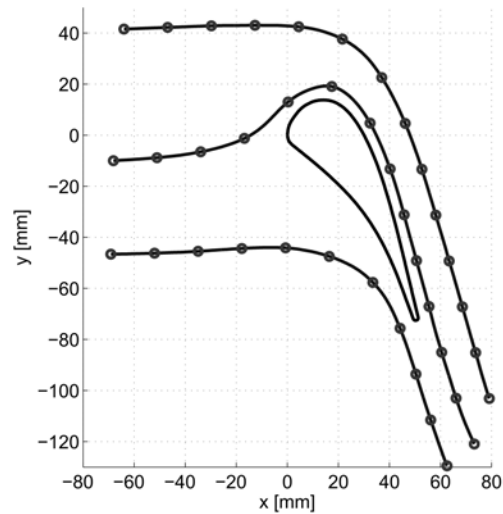


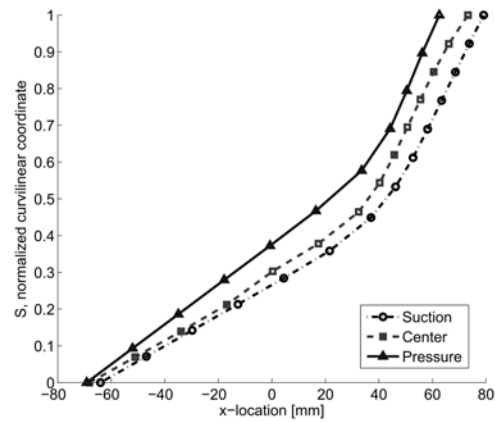
Figure 5.8: Isosurfaces of 10% concentration (blue) inside pressure-side streamtube (gray) seeded with circular cross-section in three orientations

The normalized curvilinear coordinate,  $S$ , is determined by calculating the distance traveled along the streamline, then dividing by the distance from the farthest upstream to the farthest downstream data point. This is illustrated in Figure 5.9. In many of the results figures presented below, data have been extracted in planes orthogonal to the streamtube. The locations of these planes are indicated with circles in Figure 5.9(a). The normalized curvilinear coordinate is plotted against the inlet streamwise location,  $x$ , for each of the hot streaks in Figure 5.9(b).

Normalized streamtube perimeters for each of the streaks are plotted against the normalized curvilinear coordinate ( $S$ ) in Figure 5.10. Each of the streamtubes maintains a normalized perimeter of about 1 from  $0 \leq S \leq 0.3$ , then the streamtubes start to experience distortion and the value of the normalized perimeter increases. Some portions of the streamtube have a normalized perimeter of below 1.0. This error is due to the fact that the streamtubes are calculated by integrating experimental data. In the pressure side and center hot streak streamtubes, the streamtubes maintain circular cross sections from  $0 \leq S \leq 0.3$ . For  $S > 0.3$ , the acceleration of the velocity field as the channel narrows causes the streamtube to flatten in one direction while maintaining the same width in the spanwise direction. The suction side streamtube flattens out almost immediately after introduction into the test section and continues



(a) Coordinates of streamlines and vane geometry. Dots on streamlines indicate locations where data are extracted on normal planes



(b) Relationship between  $x$  and  $S$

Figure 5.9: Geometry of vane, streamlines, and extraction planes

to grow away from a circular cross-section, which is corroborated by the increasing normalized streamtube perimeter shown in Figure 5.10.

The cross-sectional areas of the streamtube, found in planes orthogonal to the streamtube are plotted as a function of local streamwise velocity in Figure 5.11.

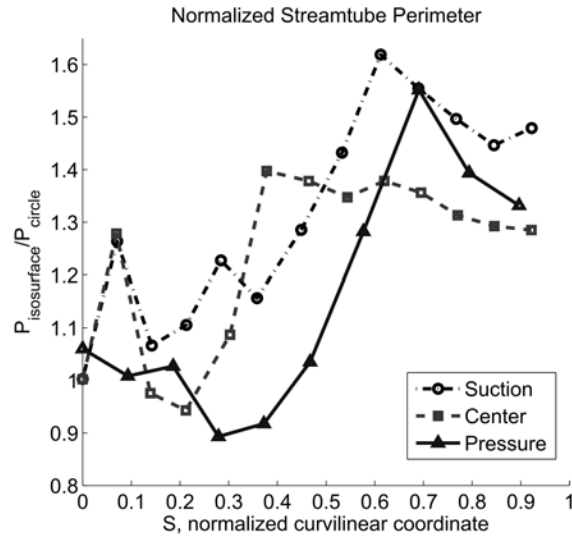


Figure 5.10: Normalized perimeter of streamtubes

Each streamtube starts with a cross-sectional area of 113 square mm ( $A_o$ ) at an inlet velocity of approximately 0.4 m/s ( $V_{inlet}$ ). As the local streamwise velocity increases, the area of the streamtube decreases as  $1/V_{local}$ , where  $V_{local}$  is the local streamwise velocity. This is required to satisfy continuity and the close agreement indicates that the streamtube calculations using the measured velocity field are reasonably accurate. The solid line plotted in Figure 5.11 is the theoretical relationship between the local streamwise velocity and the volumetric flow rate,  $A_o \times V_{inlet}$ .

The mean streamwise velocity in each streamtube is presented against the x-coordinate (5.12(a)) and the normalized curvilinear coordinate (5.12(b)). These plots show that the flow is accelerating slowly in all three hot streaks until it encounters the leading edge of the vane (at  $x = 0$  mm) and then rapidly speeds up. The flow starts to decelerate at the vane trailing edge but remains fairly uniform across the channel in the vane wake.

Contours of concentration in slices orthogonal to the streamtube for each hot streak are plotted in Figures 5.13, 5.14, and 5.15. Six slices are shown for the suction

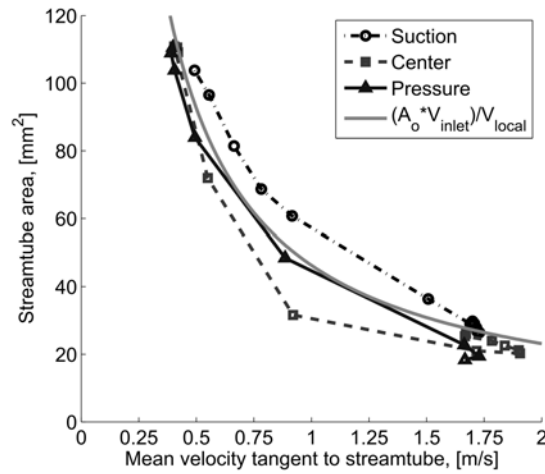
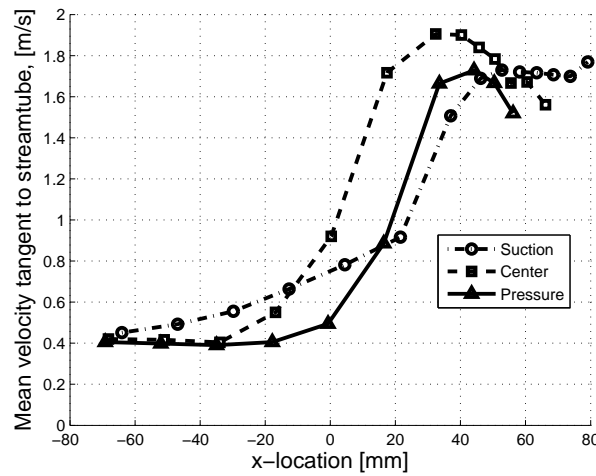


Figure 5.11: Streamtube cross-sectional area as a function of local streamwise velocity.

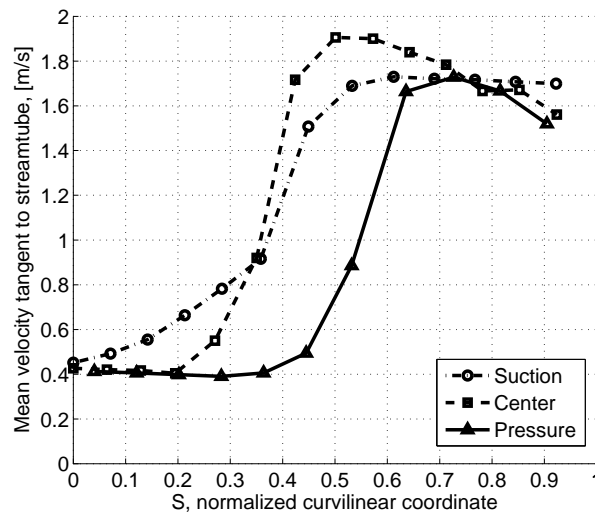
side and center cases illustrating the evolution of the streak from the inlet to the wake of the vane, and five slices are shown for the pressure side case (the pressure side streak does not extend as far in the  $x$ -direction as the other two streaks).

Figure 5.13 shows slices orthogonal to the suction side hot streak. At  $x=-64$  mm, this hot streak has a nearly circular cross-section due to the lack of cross-flow velocity affecting the hot streak between the injection point and the test section inlet. At  $x=4$  mm, the cross-section of the hot streak has started to flatten in the normal ( $n$ ) direction. The spanwise width of the hot streak has remained the same, with some spreading of the concentration in this direction. The behavior of the streak in the normal direction is very similar to the behavior of the streamtube in this location. At  $x=37$  mm, the concentration decreases rapidly from the previous upstream locations. Although the concentration is decreasing rapidly, the hot streak maintains a nominally circular cross-section. As will be discussed later in this chapter, this is not the case for the other two hot streaks.

Examining Figure 5.14, it can be seen that the center hot streak is somewhat distorted as it enters the cascade at  $x = -68$  mm. Turbulent dispersion causes the



(a) Mean streamwise velocity in each streamtube vs. x-coordinate



(b) Mean streamwise velocity in each streamtube vs. normalized curvilinear coordinate, S

Figure 5.12: Mean streamwise velocity in each streamtube vs. x-coordinate and normalized curvilinear coordinate. The flow accelerates slowly in the inlet section, then accelerates rapidly as it encounters the vane, followed by deceleration in the vane wake.

streak to diffuse primarily in the z-direction. This counteracts the effect of the flow acceleration which is narrowing the streamtube in the normal direction. The streak

behaves in the same manner as the streamtube at this location. This center streak interacts with the turbulent boundary layer on the suction surface which enhances the dispersion. Despite the dispersion by both the freestream and boundary layer turbulence, there is still a significant concentration nonuniformity by the most downstream position pictured ( $x = 66$  mm), which is approximately 35 mm downstream of the vane trailing edge.

Similar to the center hot streak, the pressure side hot streak is also distorted as it enters the test section due to the cross-flow velocity present at the injection point, as discussed previously. Contours of concentration slices extracted in orthogonal planes to the pressure side hot streak are plotted in Figure 5.15. Like the suction streak, the pressure side streak experiences minimal spreading in the spanwise direction until the flow encounters acceleration as a result of the presence of the vane leading edge. Downstream of this point,  $x=0$  mm, the hot streak shrinks in the normal direction and spreads out in the spanwise direction, again primarily due to spanwise diffusion. The concentration in the hot streak continues to diminish with increasing downstream position.

Table 5.1: Hot streaks concentration inlet conditions. Low concentration data are used for the suction side hot streak and high concentration data for the pressure side and center hot streaks. The concentration is expressed in terms of N% of 0.015M copper sulfate solution in water and ethanol, where 0.015M is the reference concentration value used for calibration.

Position of streak	Mean inlet concentration	Location
Suction side	76%	$-74\text{mm} < x < -69\text{mm}$
Center	49%	$-74\text{mm} < x < -69\text{mm}$
Pressure side	34%	$-74\text{mm} < x < -69\text{mm}$

A detailed comparison of the concentration behaviors of the three hot streaks can be performed using a normalized peak concentration measurement. The variation of normalized peak concentration in each streamwise location for each case is presented

in Figure 5.16. Each case is normalized by the mean of the maximum concentration found in each of the six slices at the farthest upstream locations for each individual hot streak ( $-74 \text{ mm} < x < -69 \text{ mm}$ ). It should be noted that this analysis is performed using low concentration data for the suction side hot streak and high concentration data for the pressure side and center hot streaks, due to the difference in hot streak concentration among the three streaks due to the inlet conditions as discussed previously. This average peak concentration at the inlet is recorded in Table 5.1. Using this normalization, the decrease in peak concentration as the streak travels through the channel can be compared between hot streaks, even though the original inlet concentrations are not matched. The center and suction side normalized concentrations decrease monotonically from 100% at  $S = 0$  down to about 15%-20% at  $S = 1$ . It is somewhat surprising that the suction side peak concentration decreases more rapidly in the test section than the center streak since the latter interacts with the turbulent boundary layer on the vane. Note though that the unsteadiness of the streak, perhaps induced by the boundary layer on the outer wall of the cascade would produce an identical signature in the mean concentration distribution. The pressure side hot streak experiences a slower decrease through the test section in normalized concentration as it passes under the vane. This decrease is maintained throughout the channel, such that the normalized concentration in this region is still 30% at  $S = 1$ . One factor to consider is that the path length of this streak is shorter than the other two. Probably it is more important that this streak is farthest from the tunnel walls, and doesn't interact with the vane. As mentioned in the introduction, Vicharelli and Eaton [59] showed that freestream turbulence was strongly suppressed in a similar cascade. Previous work (Yapa et al.[60]) has shown that pressure side cutback cooling produces strong vortices in the vane wake which would be expected to mix the center streak with both mainstream flow and the trailing edge coolant. Interestingly, the pressure side hot streak does not appear to be impacted by the strong vortices in this

region.

Table 5.2: Hot streaks concentration inlet conditions for the low concentration data set. The concentration is expressed in terms of N% of 0.015M copper sulfate solution in water and ethanol, which is the reference concentration value used for calibration. The mean inlet concentration for each streak is calculated by averaging the peak concentrations of the six axial slices in the range  $-74 \text{ mm} < x < -69 \text{ mm}$ .

LOW CONCENTRATION			
Hot streak	Suction	Center	Pressure
Mean inlet concentration	76%	19%	13%

Table 5.3: Hot streaks concentration inlet conditions for the high concentration data set. The concentration is expressed in terms of N% of 0.015M copper sulfate solution in water and ethanol, which is the reference concentration value used for calibration. The mean inlet concentration for each streak is calculated by averaging the peak concentrations of the six axial slices in the range  $-74 \text{ mm} < x < -69 \text{ mm}$ . As stated previously, the calibration curve between signal magnitude and copper sulfate concentration is linear in the 0-0.015M concentration range. The mean inlet concentration value for the suction side hot streak is estimated by comparing the inlet concentrations of the high and low concentration data sets for the center and pressure hot streaks and determining what scaling factor exists between the measured concentration fields. This scaling factor is then applied to the low concentration data set to estimate the high concentration suction side hot streak inlet concentration as a percentage of 0.015M.

HIGH CONCENTRATION			
Hot streak	Suction (estimated)	Center	Pressure
Mean inlet concentration	194%	49%	34%

Dispersion of the hot streaks in the vane wake is expected to be important for several reasons. First, wake turbulence is generally more energetic and of larger scale than the boundary layer turbulence because the normal constraint is alleviated. Also, the complex vortex structures formed around the film-cooled trailing edge and the jets emerging from the individual film cooling slots can enhance mixing in the wake. Finally, this last stage of mixing is what finally determines the inlet temperature profile entering the turbine rotor.

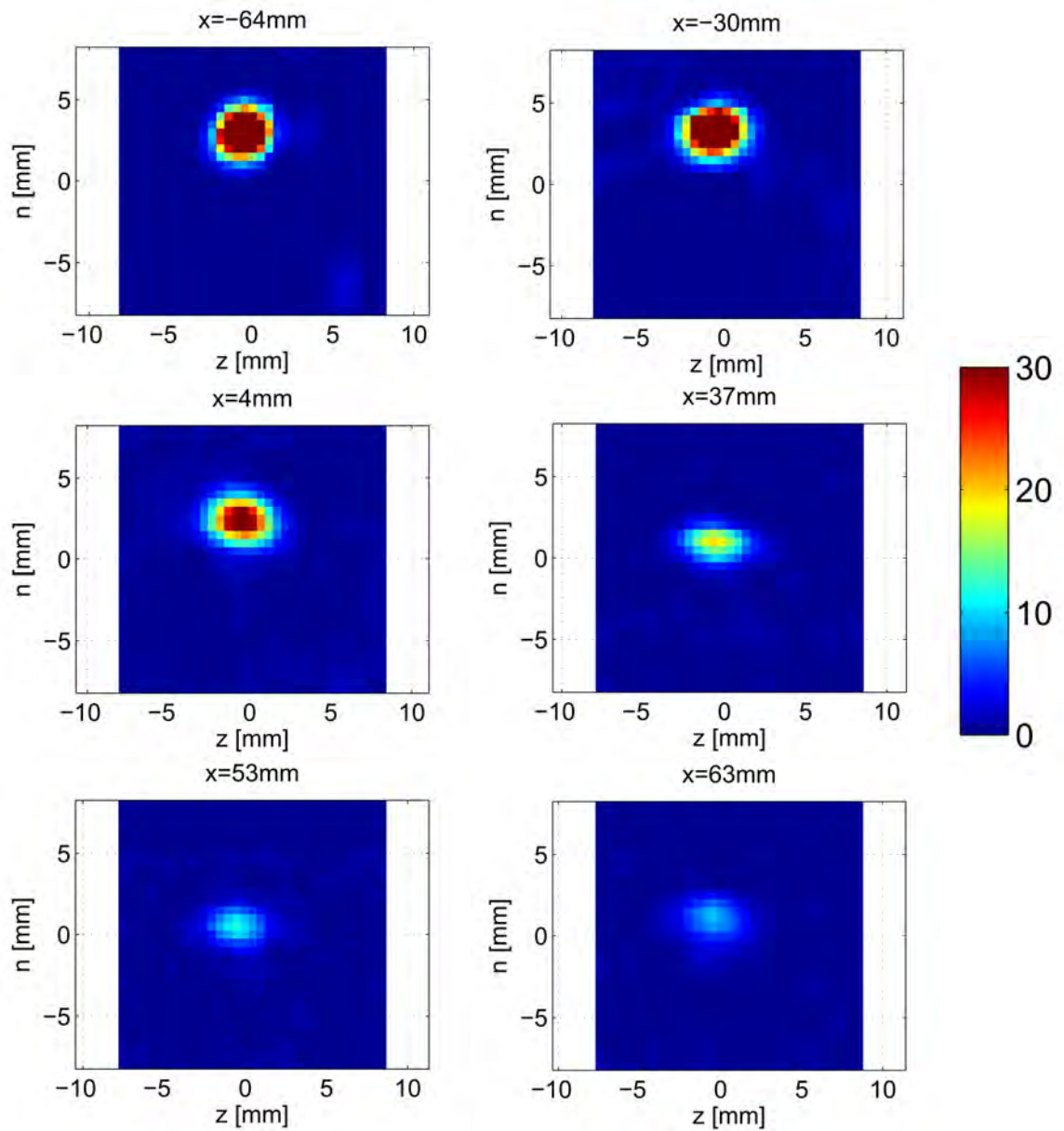


Figure 5.13: Contours of concentration in suction side hot streak, in slices normal to the flow velocity at various  $x$ -locations.  $Z$  is the spanwise direction and  $n$  is the coordinate normal to both the streamline and the vane surface. Data from low concentration data set.

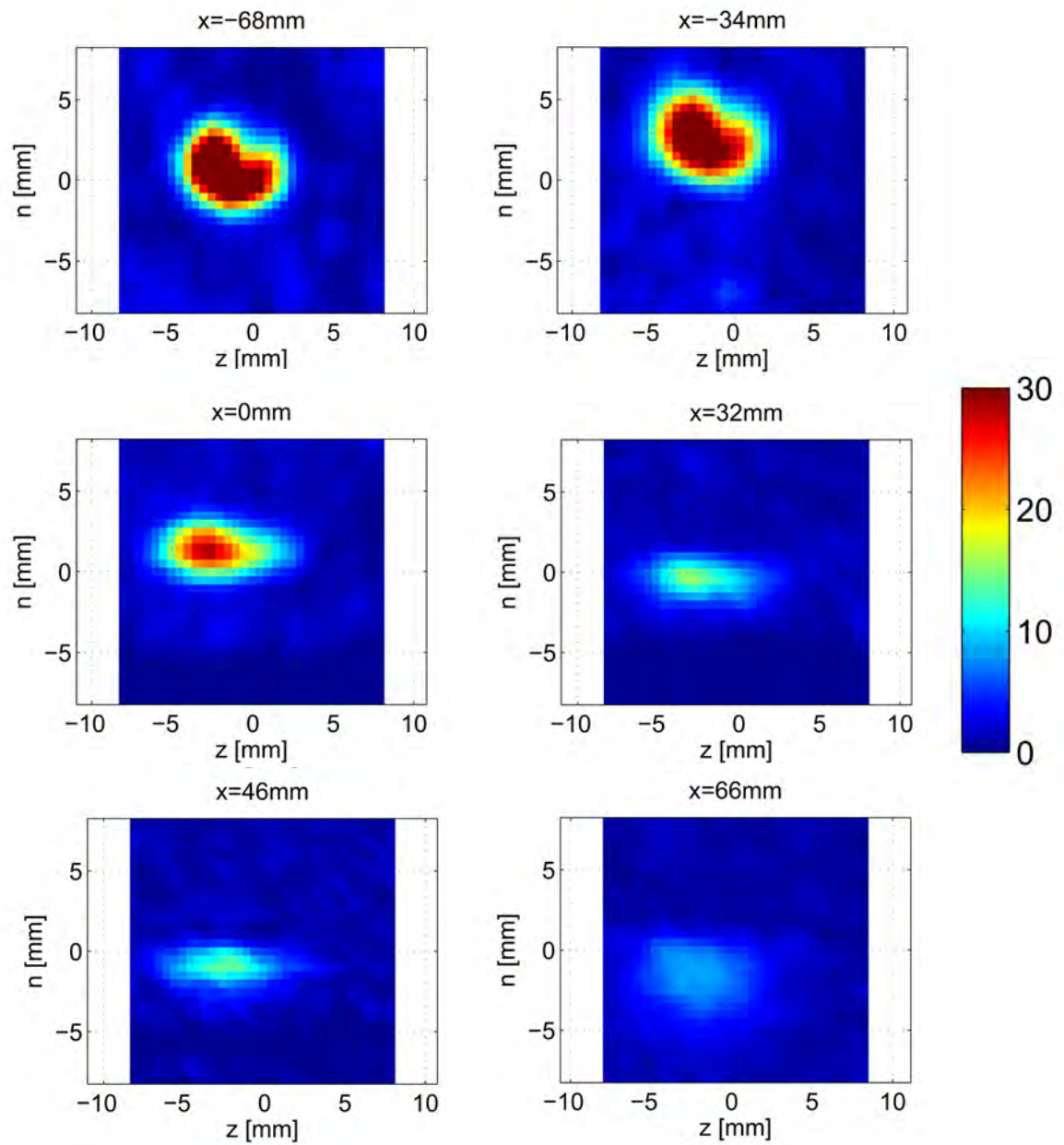


Figure 5.14: Contours of concentration in center hot streak, in slices normal to the flow velocity at various  $x$ -locations.  $Z$  is the spanwise direction and  $n$  is the coordinate normal to both the streamline and the vane surface. Data from high concentration data set.

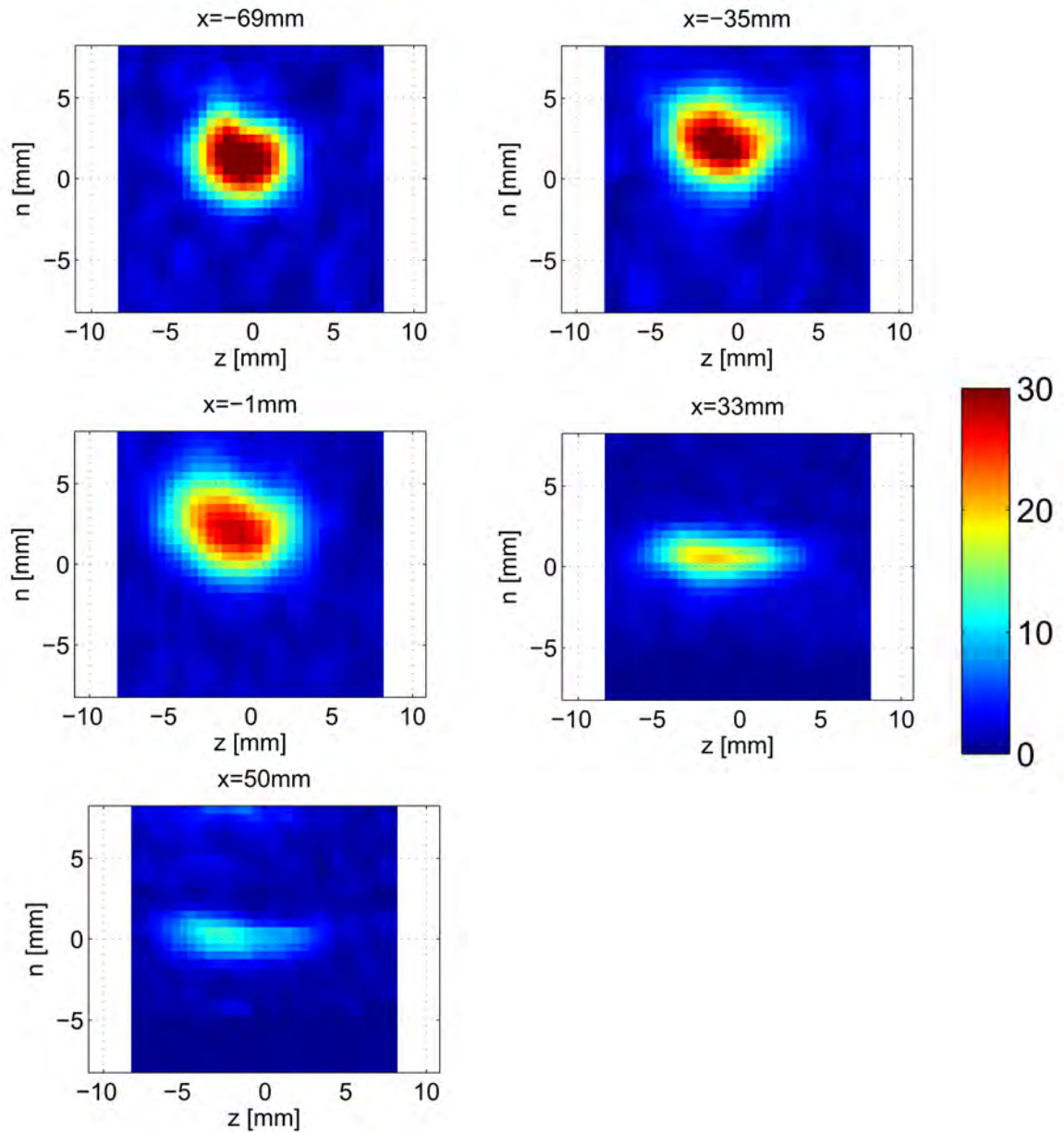


Figure 5.15: Contours of concentration in pressure side hot streak, in slices normal to the flow velocity at various  $x$ -locations.  $Z$  is the spanwise direction and  $n$  is the coordinate normal to both the streamline and the vane surface. Data from high concentration data set.

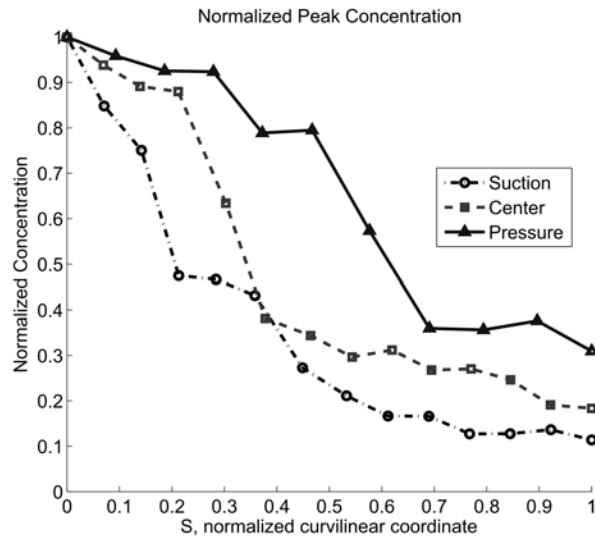


Figure 5.16: Normalized peak concentration vs downstream location

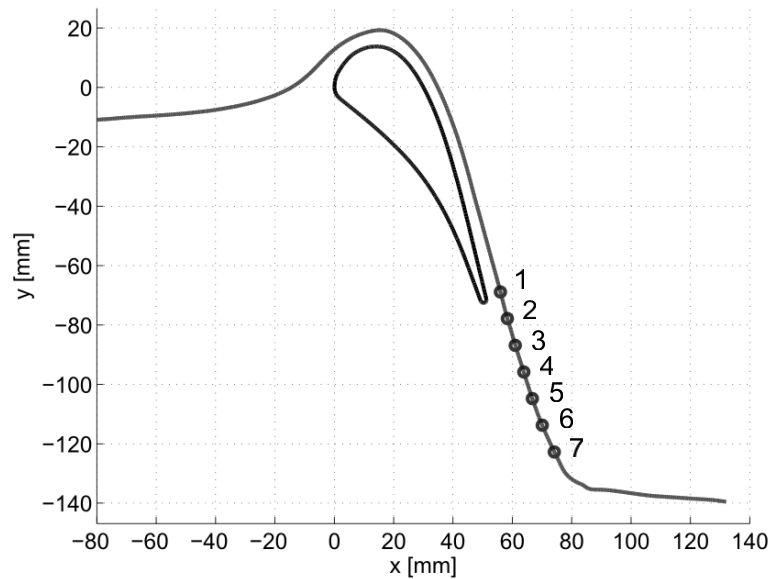


Figure 5.17: Locations of slices of contours of concentration plotted in Figures 5.18 and 5.21. Concentration profiles extracted from locations 2, 4, and 6 are plotted in Figures 5.20 and 5.22.

The wake data are analyzed on planes normal to the center streamtube at the locations indicated in Figure 5.17. Concentration contours from the high concentration

experiments are plotted in Figure 5.18 for planes normal to the center streamtube. There are large differences in concentration between the three streaks. This is due partially to the fact that the concentrations differed markedly at the inlet to the test section, at  $x \cong -69$  mm. To help make sense of the following discussion, Tables 5.2 and 5.3 show the streak-specific averages of the peak concentration values measured for each streak at the six axial slices in the range  $-74 \text{ mm} < x < -69 \text{ mm}$  for both data sets. The inlet plane for the normalized concentration values is defined as  $x = -69$  mm. The value for the suction side streak from the high concentration data set is inferred by comparing the high concentration data set to the low concentration data set for the other two streaks, because the high concentration MRC measurements for the suction side streak are greater than the maximum concentration value in the calibration between MR signal magnitude and concentration. The low concentration center hot streak mean inlet concentration is a factor of approximately 2.5 lower than the high concentration mean inlet concentration. The same observation can be made about the pressure side hot streak mean inlet concentration. Therefore, the low concentration suction side hot streak inlet concentration presented in Table 5.2 is multiplied by a factor of approximately 2.5 to get the high concentration suction side hot streak concentration presented in Table 5.3. This is probably due to the fact that the copper sulfate solution is made using anhydrous copper sulfate crystals, which are added to deaerated water. Before the copper sulfate solution is used in an MRC however, it is filtered multiple times and any copper sulfate crystals that did not fully dissolve are removed from the solution. This means that the actual concentration of the copper sulfate solution is less than the nominal concentration (e.g. 0.015M, 0.02M, 0.08M) and the measured signal magnitudes in the MRC reflect this difference.

The pressure gradient normal to the streamwise direction is very small, and is assumed to be negligible through the course of these experiments. This assumption is corroborated by calculating the average velocity direction of over 1000 streamlines in

the wake. The differences in velocity direction between the streamlines and the center streamline plotted in Figure 5.17 in the near wake region (Locations 2 and 3) are less than  $10^\circ$  for all of the streamlines calculated, indicating that the mean streamwise velocity is well-aligned and that any pressure gradient in the normal direction is minimal.

Looking at Figure 5.18, the suction side hot streak has a high concentration core at slice location 1 and maintains the highest concentration throughout the wake. This streak also maintains a nearly circular shape to the end of the measurement domain. By contrast, the center streak diffuses much more rapidly. At location 1, the central core of this streak is flattened, but there appears to be strong diffusion in the negative  $n$ -direction resulting in a diffuse and nearly circular streak by location 7. The pronounced distortion of the hot streak cross-section at the inlet has essentially been removed by the beginning of the wake section. Instead, the center hot streak resembles an ellipse. The pressure side streak is highly flattened at location 1 and maintains that shape to the end of the test section. The pressure side hot streak appears to maintain most of its concentration, indicating that the turbulent diffusion in the  $n$ -direction is weak.

Figure 5.19 shows the same contours plotted in Figure 5.18 at downstream locations 1 and 4 with in-plane velocity vectors plotted on top of the concentration contours. Location 1 (left) is in the direct wake of the trailing edge of the vane. Location 4 (right) is in the mid-wake region. It can be observed that the velocity deficit caused by the presence of the vane at Location 1 has disappeared by Location 4. The normal velocity in this plane increases in the positive  $n$ -direction, contributing to the spreading of the center hot streak. The velocity remains generally in the same direction and of the same magnitude near the suction side hot streak (top of the figure). On the pressure side, the flow appears to be accelerating in the normal direction between Locations 1 and 4 but there is very little change in the way of

spanwise velocity. The lack of any coherent vorticity structures is likely responsible for the maintenance of the coherence of the pressure-side hot streak.

Concentration profiles for downstream locations 2,4, and 6 are plotted for multiple spanwise locations in Figure 5.20. These concentration profiles both show quantitative differences between concentrations in each of the streaks as well as the spanwise variation. The profile at  $z=-3$  mm cuts through the center of each streak. Each streak appears to have a roughly Gaussian distribution in the normal direction. The profiles are centered at  $z = -3$  mm due to issues in manufacturing the hot streak generator. The cantilevered nature of the hot streak injectors allows for little remedy if the injectors are aligned slightly off-center (which is what happened in this case). These plots corroborate the conclusion reached by examining Figure 5.18. The central peak drops more rapidly than either the suction or pressure side peak. In fact, the peak value in the pressure side streak has no significant drop through the wake.

Concentration contours from the low concentration experiments are presented in Figure 5.21. The low concentration data set does not give quantitative data in the wake region for either the center or pressure-side hot streaks because the measured concentration is small and close to the MRC measurement uncertainty. It does, however, help confirm that the scaling factor used to estimate the mean inlet concentration for the suction side hot streak in the high concentration data set is correct. The concentration profiles in Figure 5.22 show that the low concentration data has about 2.5 times less concentration than the high concentration data set. The low and high concentration data both show that the hot streak concentration is highest in the suction side hot streak and lowest in the center hot streak. This conclusion is in direct agreement with the peak concentration analysis presented earlier. Viewing the low concentration data in this way essentially ensures that the data are repeatable and also that the calibration used is valid for the ranges of concentration in which it has been applied.

The concentration transport in the streamtube (hereafter referred to simply as concentration transport) for each streak is evaluated at five locations in the wake for each streak. A streamline is calculated at the center of each streak starting at the inlet to the test section. This is done to ensure that concentration transport quantities are calculated on planes orthogonal to the local flow direction. The streamtubes used in this analysis are the same as those presented previously.

Figure 5.23(a) shows the three streamlines and the five slices orthogonal to the flow direction in each of the hot streaks. A curvilinear coordinate for the wake for each hot streak was calculated using the most upstream location in the streak streamline as  $S_{\text{wake}} = 0$ . The relationship between  $x$ -coordinate and  $S_{\text{wake}}$  is plotted in Figure 5.23(b).

The concentration transport at each of the slices in Figure 5.23(a) is determined by calculating the product of concentration and local streamwise velocity and integrating this quantity over the cross-sectional area of the streak-specific streamtube. This quantity is normalized by the peak concentration transport value to facilitate comparison between streaks. The concentration transport indicates the amount of concentration that is advected by the flow in the streamtube. Because the concentration transport is integrated over the area of the streamtube, there should be no advection through the surface of the streamtube. Therefore, any difference between concentration transport quantities at increasing downstream locations in a streamtube is due to turbulent diffusion through the streamtube surface. An estimate of the effect of turbulent diffusion on the hot streak concentration can be determined by calculating the slope of the concentration transport vs. the wake curvilinear coordinate. The concentration transport has the largest negative slope from  $S_{\text{wake}}=0$  mm to  $S_{\text{wake}} = 30$  mm (about halfway through the wake region). The effect of turbulent diffusion for all three hot streaks is small or possibly zero for  $S_{\text{wake}} > 30$  mm. This is probably due to the lessened effect of the pressure-side cutback cooling

on the turbulent mixing in the far wake region. The suction side hot streak also decreases in concentration in the wake region, but the mixing mechanism for this region is still not fully determined. Since the freestream turbulence has been suppressed due to the acceleration of the flow, the mixing of the hot streaks with the main flow is lessened after the effects of the pressure side cutback become weaker with increasing downstream location.

## 5.5 Summary

The take-away message from the data and analysis presented in this chapter is that the hot streaks impacting a film cooled vane maintain non-zero concentration and coherent structure over the entire test section. In particular, Figures 5.6-5.8, 5.16, 5.18-5.22, and 5.24 show that the flow exiting the vane cascade has a distinctly non-uniform concentration distribution. This means that the uniform inlet temperature distributions used in designing turbine blades not necessarily correct, and that designers are creating film-cooled turbine blades which probably experience different heat loads than are currently specified during the design process. It is clear that traveling through a vane cascade is not enough to break up the coherent behavior of the hot streaks. In the future, computational fluid dynamics tests can be performed for this geometry to validate the turbulent mixing models used in the Reynolds-averaged Navier Stokes solvers commonly utilized in commercially available CFD solvers. More experimental and numerical investigation is merited to further inform the design process.

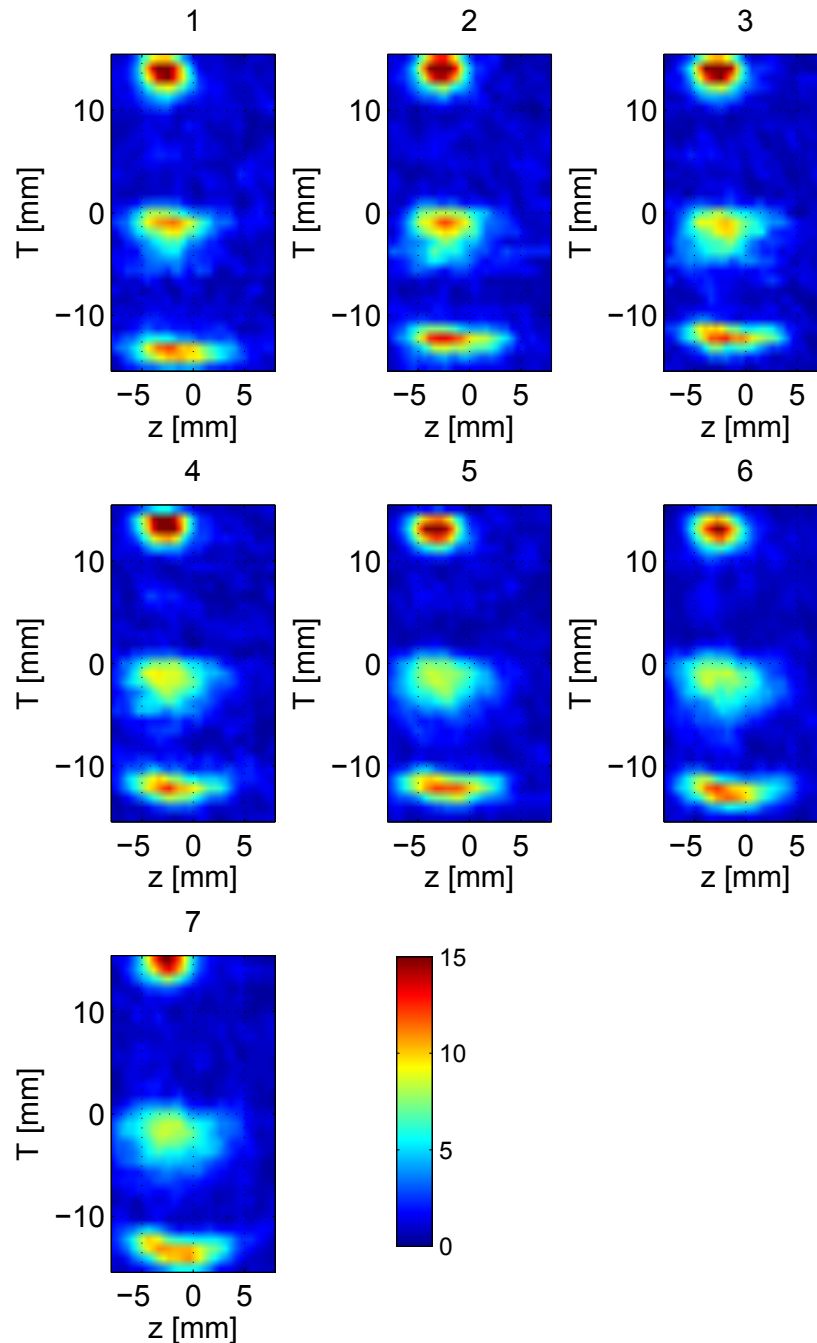


Figure 5.18: Contours of concentration in the wake of the vane trailing edge at locations illustrated in Figure 5.17. Contours of concentration are from the high concentration data set. Contours of concentration are from the low concentration data set. The locations of the contour slices 1-7 correspond to the locations detailed in Figure 5.17.

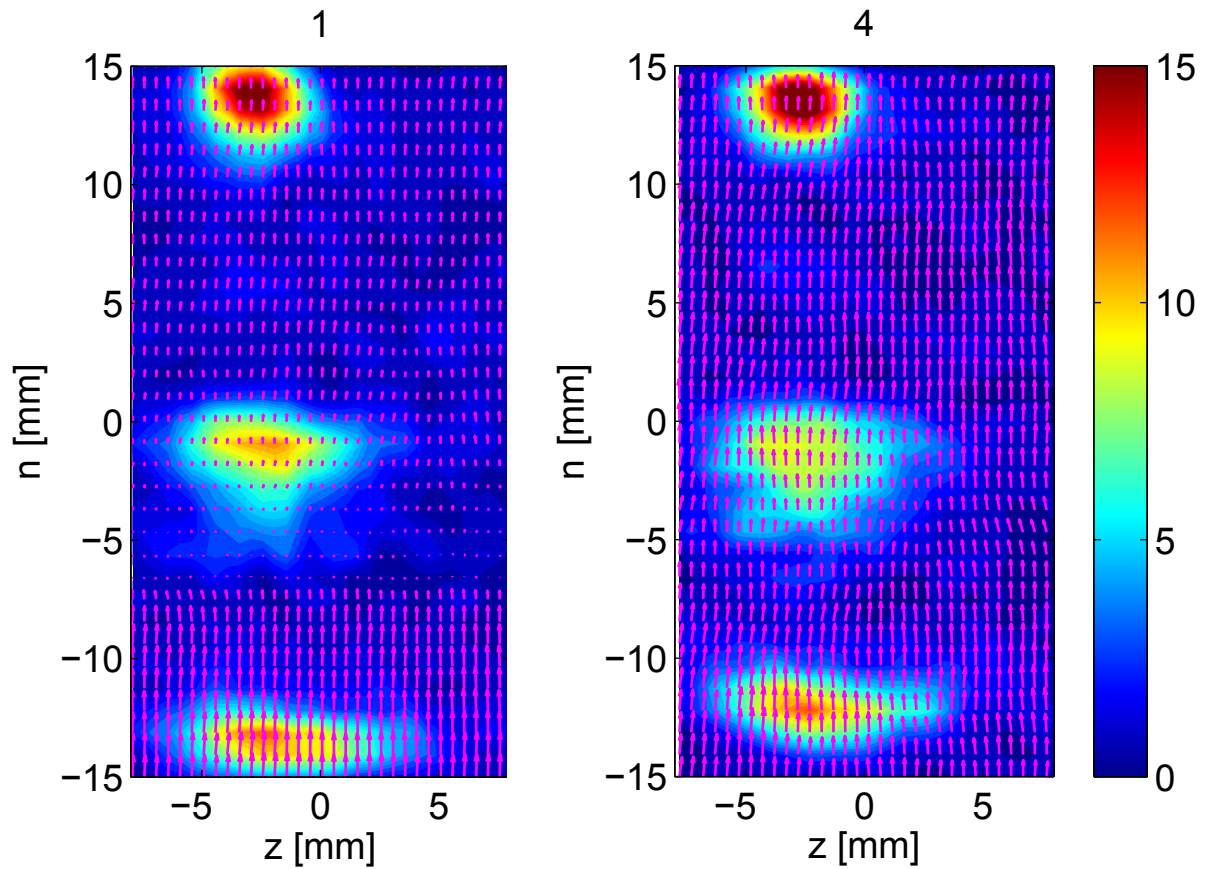


Figure 5.19: Contours of concentration in the wake of the vane trailing edge at Locations 1 and 4 as illustrated in Figure 5.17. Vectors of in-plane velocity are plotted for each extracted plane of data. These vectors show small velocities in the direct wake of the trailing edge of the vane (Location 1). The velocity deficit in the wake is filled and there appears to be little distortion of the flow in Location 4.

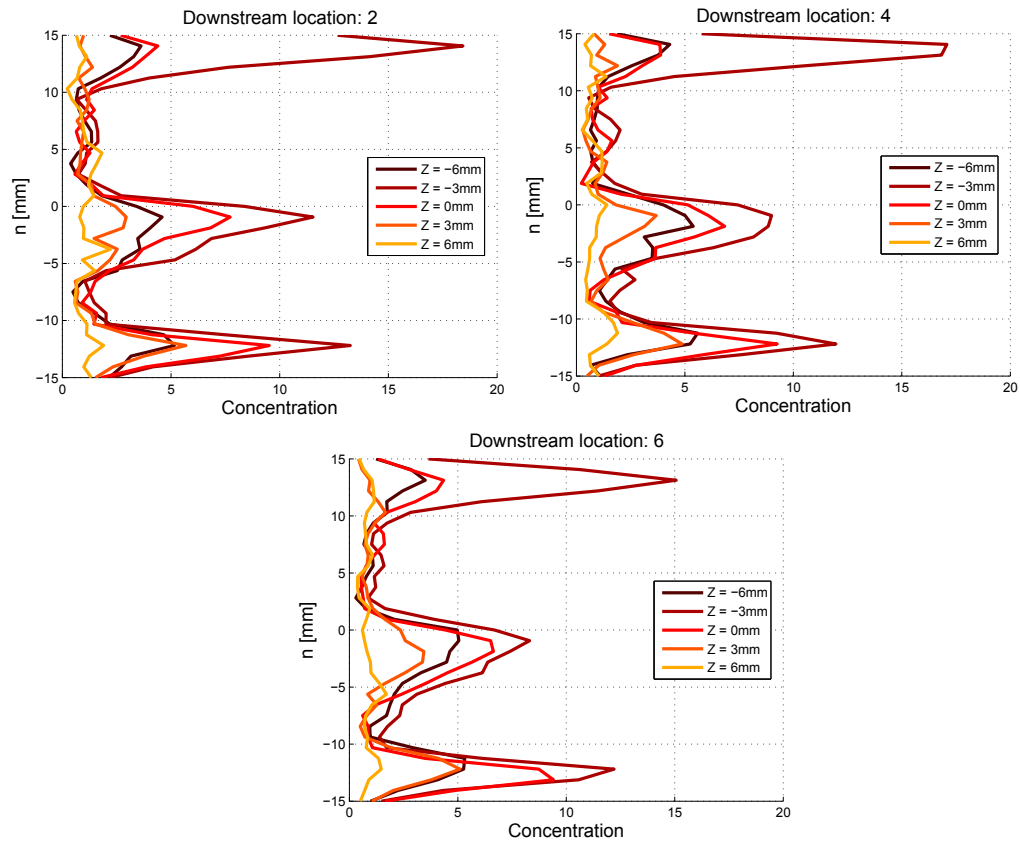


Figure 5.20: Profiles of concentration at spanwise locations  $z = -6$ ,  $z = -3$ ,  $z = 0$ ,  $z = 3$ ,  $z = 6$  mm at downstream locations 2,4, and 6 from Figure 5.17. Data presented is from the high concentration data set. The upper peak for each trace corresponds to the suction side streak, the middle peak to the center streak, and the lower peak to the pressure side streak.

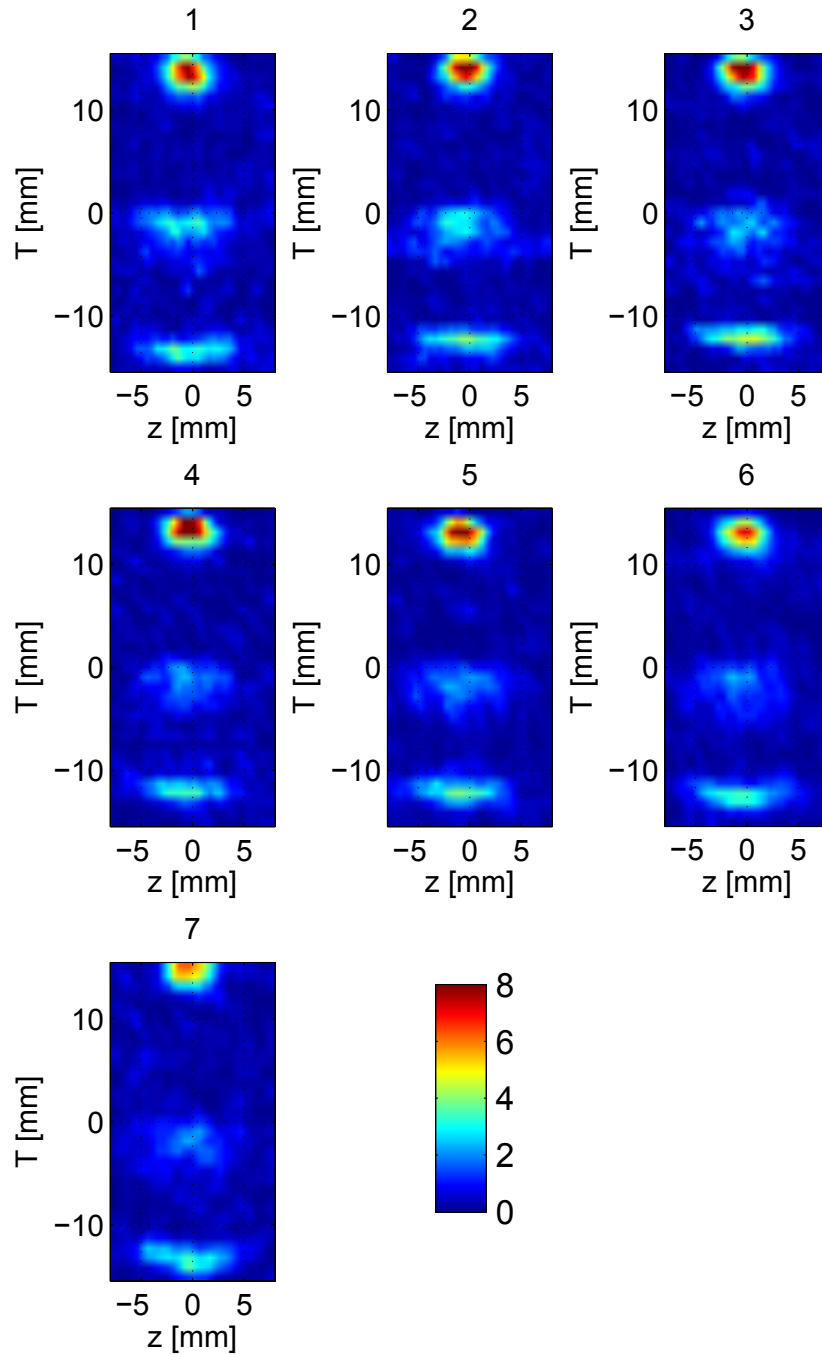


Figure 5.21: Contours of concentration in the wake of the vane trailing edge at locations illustrated in Figure 5.17. Contours of concentration are from the low concentration data set. The locations of the contour slices 1-7 correspond to the locations detailed in Figure 5.17.

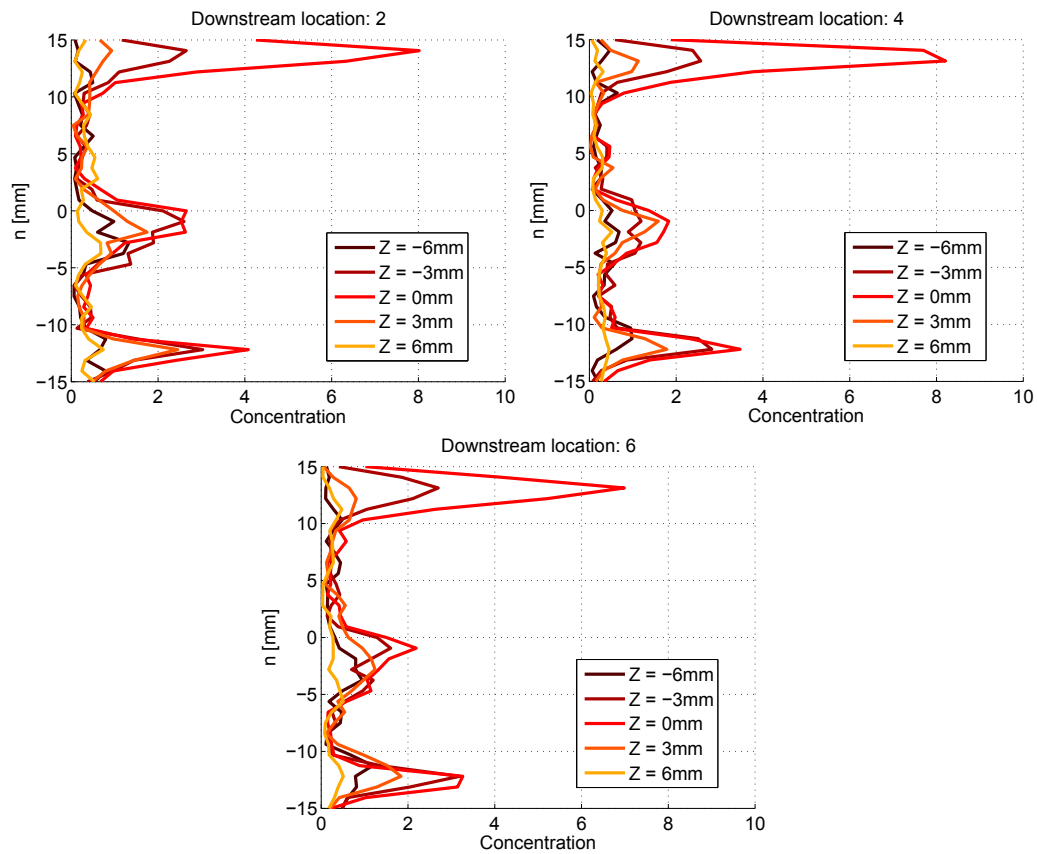
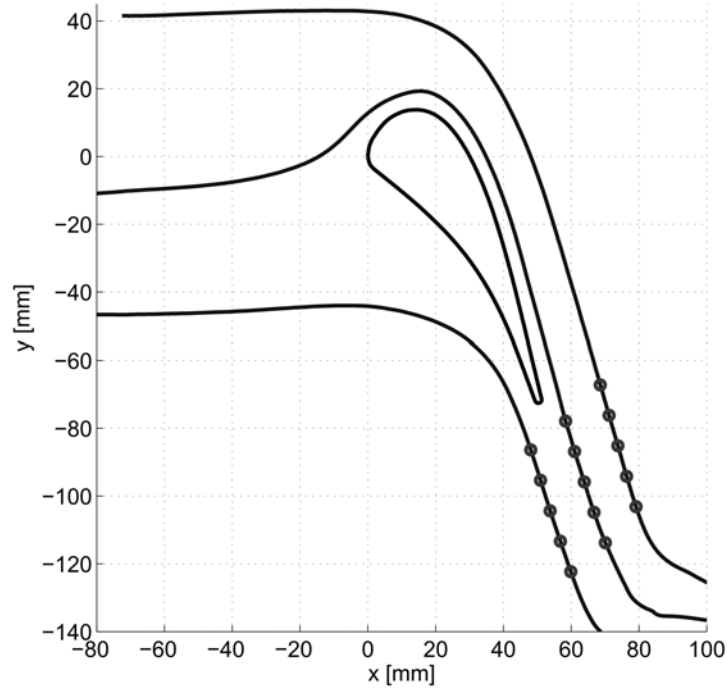
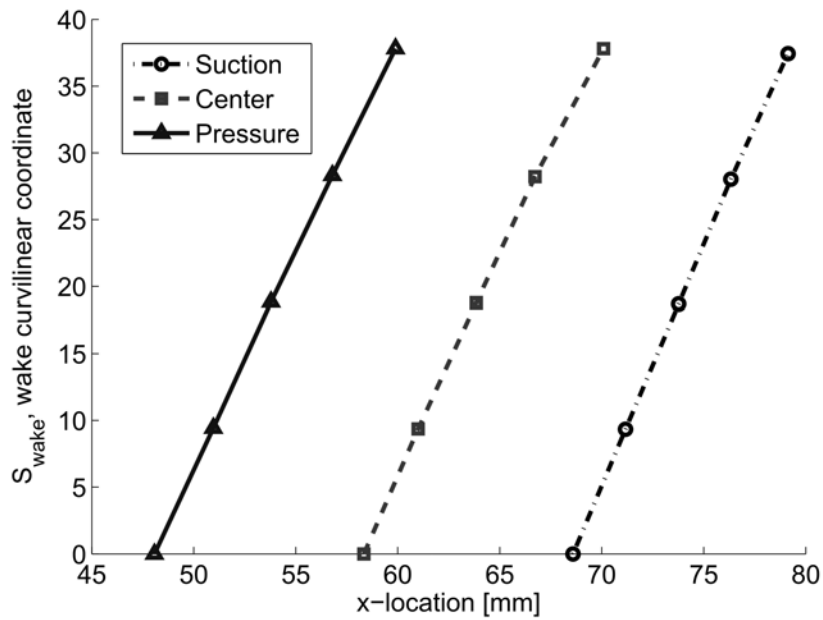


Figure 5.22: Profiles of concentration at spanwise locations  $z = -6, z = -3, z = 0, z = 3, z = 6$  mm at downstream locations 2,4, and 6 from Figure 5.17. Data presented is from the low concentration data set. Note that the x-axis is in the range 0 to 10%, half of the x-axis plotted in Figure 5.20 for the high concentration data set profiles.

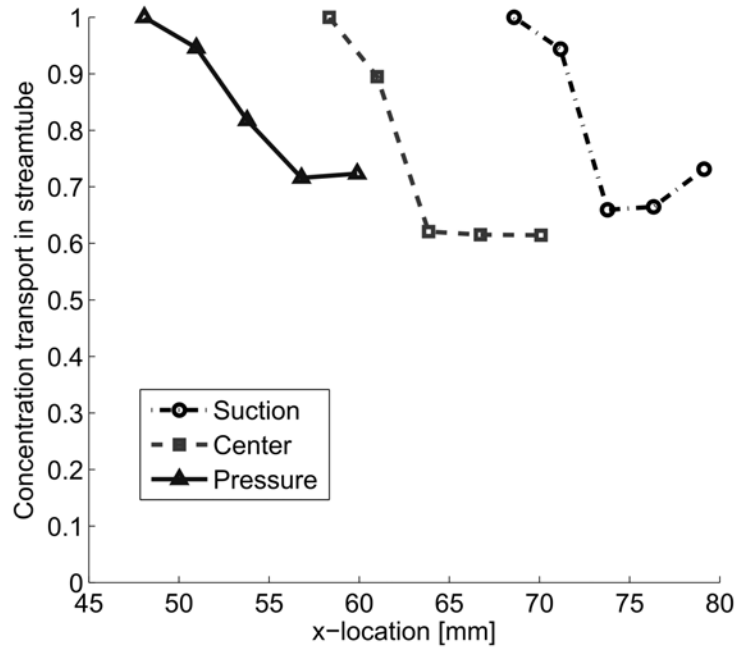


(a) Coordinates of streamlines and vane geometry with locations of slices in the wake

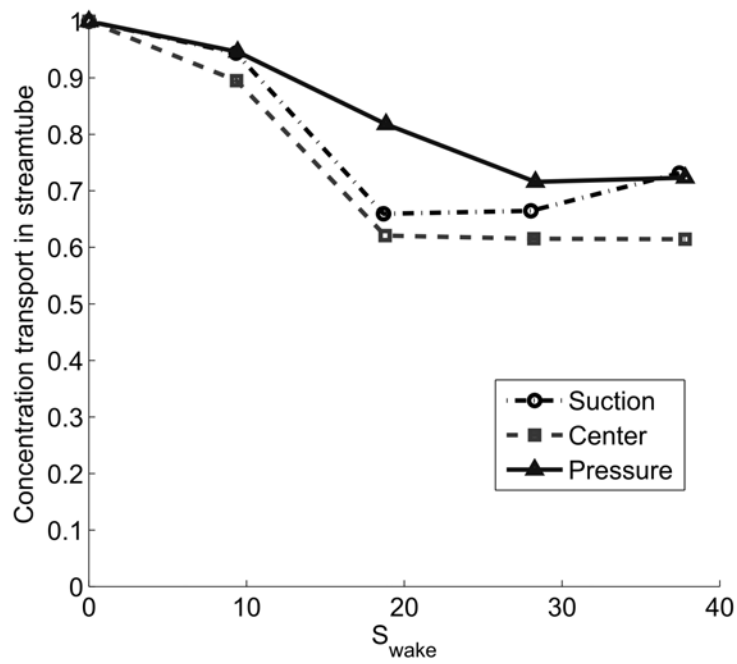


(b) Relationship between  $x$  and  $S_{wake}$

Figure 5.23: Geometry of vane, streamlines, and extraction planes in the wake of the vane trailing edge



(a)



(b)

Figure 5.24: Normalized concentration transport

# Chapter 6

## Conclusions and Recommendations

### 6.1 Compressibility Effects Experiment

A validation experiment was performed to establish the legitimacy of using the MRV/MRC experimental method to predict the performance of turbine vane film cooling. Traditionally, film cooling effectiveness has been measured using thermal techniques, which are difficult to set up and often are complicated by the effects of thermal conduction or transient effects. Furthermore, thermal experiments usually provide only surface measurements which are not sufficient to understand complex turbulent mixing flows. The perceived disadvantages of MRV/MRC are that they use water as the working fluid and require application of the scalar transport analogy between heat and a dilute contaminant. In contrast to thermal measurements, MRV/MRC experiments can be rapidly acquired, provide three-dimensional data, and have clearly defined no-penetration boundary conditions.

The Reynolds-averaged advection diffusion equation for transport of a passive scalar and the turbulent thermal energy transport equations assume the same form assuming that turbulent diffusion overwhelms molecular diffusion. Based on this reasoning, the scalar transport analogy can be utilized to predict temperature fields

based on concentration measurements in an identical geometry. To test the applicability of this approach to subsonic compressible flows, temperature measurements are performed in a mixing layer developing downstream of a blunt splitter plate at high subsonic Mach number ( $Ma = 0.7$ ). MRV/MRC experiments are performed in a test section with an identical geometry and a working fluid of water. In the temperature experiments, cool air ( $T_o = 300K$ ) is used as the mainstream flow and warm air ( $T_o = 320K$ ) is used as the secondary flow. In the water experiments, the mainstream flow is water and the secondary flow is copper sulfate solution. The concentration of the copper sulfate solution is measured in the MRV/MRC experiments and compared to the normalized temperature in the air experiments to test the validity of using concentration data to predict temperature behavior.

Prior to the present experiments, it was hypothesized that although high subsonic Mach number flows are compressible, the turbulent mixing mechanisms are unaffected by compressibility unless shocks are present. This hypothesis had not been tested in complex, 3D flows relevant to film cooling. The present experiments support this hypothesis by showing that water-based MRC can accurately and precisely predict the temperature distribution in the air experiments to within the measured uncertainty of the present measurements (a few percent), once the energy separation effect has been taken into account.

Further work is currently being performed to compare experimental velocity fields. Progress is under way to use PIV to measure the velocity field in the air experiments, and these data will be compared to the three-dimensional velocity field that has already been acquired by MRV. Additionally, it should be noted that the geometry of this experiment was intentionally chosen to be Reynolds-number independent. It would be useful to develop an experiment to directly test the sensitivity of mean concentration distributions to varying Reynolds number.

## 6.2 Double Passage Vane Cascade Experiments

### 6.2.1 Endwall vortex studies

The double passage vane cascade experiments, while intended primarily to study turbulent dispersion of coolant in a vane wake, unexpectedly allowed for an additional, insightful study into the development and effect of a passage vortex. Downstream of the vane trailing edge, the passage vortex both grows in the spanwise direction and decreases in peak vorticity magnitude. Detailed information about the three-dimensional behavior of the velocity in the presence of a strong vortex is available as a result of these experiments, adding to what was previously available in the literature.

### 6.2.2 Coolant dispersion in the vane wake

Turbulent dispersion of the film coolant in the vane wake is very important because it determines the variability of flow temperature entering the rotating turbine stage. The mean concentration distribution downstream of the central part of the vane span has a peak coolant concentration around 18% just downstream of the vane trailing edge decaying to about 10% at the test section exit (about 0.55 vane chords downstream of the trailing edge). The concentration wake dispersion is higher towards the vane suction side due to the effect of longitudinal vortex pairs developed at the trailing edge cutback and carrying into the wake.

The spanwise variability of the coolant concentration is presented using contour plots, which show that the coolant is segregated into high and low concentration regions as a result of the geometry of the pressure-side cutback. The wake structure is spanwise periodic over the central 55% of the span (5 slot pitches) with the spatial period corresponding to the slot spacing. Quantitative data show that the peak to peak variations of coolant concentration are as much as 5%. In the endwall region,

both the maximum concentration and the spanwise variability in the concentration are strongly reduced due to the presence of the passage vortex. The spanwise concentration is also less near the endwall due to the lack of coolant injection in this region as a result of the pressure-side cutback geometry.

In the endwall region, rapid mixing is present in the near wake. This mixing probably also occurs on the vane surface where the coolant is introduced into the flow. Streamtubes are used to illustrate the turning features of the flow and to assess the turbulent mixing occurring in the flow. The smaller size streamtubes are used to estimate turbulent dispersion by calculating the product of concentration and streamwise velocity for slices normal to the flow direction. The change in concentration transport with respect to the streamwise location for the center streamtube is roughly constant over the majority of the vane wake, indicating that turbulent mixing due to the longitudinal vortices from the cutback geometry has the same effect on the concentration decrease throughout the wake. In the endwall region, however, it appears that the concentration is dropping slightly more rapidly as a result of large scale vorticity dynamics induced by the passage vortex in the near wake. The longitudinal vortices present in the center region as a result of the cutback geometry are incorporated into the larger, stronger passage vortex in the endwall region. In the mid- to far-wake (0.25 to 0.55 vane chords downstream of the trailing edge), the endwall region assumes the same behavior as in the central streamtube, as indicated by the similar rate of decrease in concentration transport in these regions.

Future work could involve adapting the double passage vane cascade test section to study showerhead film cooling and possibly MRV/MRC experiments can be performed to see the combined effect of showerhead and pressure-side cutback cooling on coolant distribution in the vane wake.

The biggest limitation in the present experiments is size. The number of voxels containing non-zero concentration data is quite small, leading to a higher than

predicted uncertainty in the calculation of the concentration transport (and other quantities). Because of this lack of resolution, the conclusions drawn on turbulent wake mixing are tentative and merit further study. In the future, it might be interesting to try these experiments on a much bigger scale. In addition to the tentative conclusions drawn here, further insight into the behavior of turbulent mixing for these flows will definitely be helpful to turbine designers.

An extension of the MRC method involving high concentration copper sulfate coolant was developed to study mixing phenomena in flow regions far downstream of the injection point. This requires the addition of alcohol to the copper sulfate solution to minimize buoyancy effects. Modified calibration and post processing techniques allow measurement uncertainty of less than 1% of the injected concentration. This means that concentrations as low as 5% of the injected concentration can be measured without excessive noise. This method was applied to both the vane wake coolant dispersion experiments and the hot streak generator experiments. Prior to the development of this technique, concentration measurements were limited to regions close to the coolant injection point. The new technique also allows for study of truly passive scalars, as the velocity field has had time to swallow the flow disturbances caused by coolant injection.

### 6.2.3 Hot streaks experiments

The behavior of hot streaks originating in the combustor and their impact on turbine vanes and blades was investigated using a simplified geometry with discrete streaks injected in the inlet of a double passage vane cascade. As shown by Yapa et al. [62], the scalar transport analogy between concentration and temperature can be used to apply the results from the MRV/MRC experiments to hot streak dispersion in full-scale turbines. Assuming that the turbulent diffusivity overwhelms molecular diffusivity, the transport equations for thermal energy and a passive scalar simplify

to the same form, with turbulent Prandtl number considered equal to the turbulent Schmidt number and, thus, temperature directly represented by concentration. In this way, the conclusions from the MRV/MRC results using copper sulfate as a passive scalar can be used quantitatively to estimate temperature distributions in a real engine configuration. The test geometry was the same pressure-side cutback cooled high pressure turbine vane. Three hot streaks were released upstream of the vane on the spanwise centerline and aligned to pass over the suction-side, center, and pressure-side of the vane. Streamtubes and concentration isosurfaces and contours were calculated from the three-dimensional experimental data, and it was found that the streamtubes experience significant distortion from their original circular cross-sections as they travel through the test section. Concentration isosurfaces experience similar distortion effects, and the peak concentration in a streamtube decreases by as much as 90% (in the suction side hot streak). The pressure side hot streak experiences the smallest drop in peak concentration, while the peak concentration in the center hot streak diminishes somewhat more than this due to its interaction with the pressure side cutback cooling. However, it is important to note that coherent hot streaks still exist at the exit of the test section, and that non-uniform concentration conditions exist at all streamwise locations in the test section. This suggests that turbulence suppression by strong acceleration plays a significant role in maintaining the streaks. The concluding message from these experiments is that the temperature distribution of the gases impacting the blades downstream of the turbine vanes remains significantly non-uniform.

The hot streaks experiments were informative, but have much room for future improvements. As in the endwall vortex study, size remains a constraint in the double passage vane cascade experiments. The large degree of turning in this cascade and the size limitations present in the MRI setup restrict the maximum size of the vane to be studied. Given that the one dimensional side length of a voxel is around 0.5mm, an

injection diameter of 3 mm-diameter hot streaks gives a starting injection diameter only 6 voxels across at its maximum width. In the future, a new experimental setup that has larger hot streaks and/or a larger vane size would be very beneficial to extracting extra information from this experiment. Additionally, the interaction of the hot streak with the passage vortex might yield very interesting results that can be used to further inform turbine designers. This experiment could be performed readily as the current hot streak generator setup can be used to explore the behavior of hot streaks located at various spanwise positions.

Overall, both the film coolant dispersion studies and the hot streaks experiments show that very significant temperature variations remain in the vane wake. Accounting for these variations in turbine design would allow improved cooling system performance and increase overall engine efficiency.

# Appendix A

## Coordinates for VKI vane

The manufacturing coordinates of the airfoil are presented.  $x - y$  coordinates, as well as curvilinear ( $s$ ) and normalized curvilinear coordinates ( $s/C$ ), where  $C$ , are provided.

Suction Side				Pressure Side			
x[mm]	y[mm]	s[mm]	s/C	x[mm]	y[mm]	s[mm]	s/C
0.245888	2.099081	2.112973	0.023902	0.257002	-1.26834	-1.29473	-0.01465
0.257002	2.158817	2.174098	0.024594	0.490388	-2.04351	-2.10325	-0.02379
0.515393	3.263231	3.309074	0.037433	0.515393	-2.10186	-2.16715	-0.02452
0.772395	3.95922	4.050907	0.045825	0.772395	-2.58113	-2.71033	-0.03066
1.030786	4.581582	4.724669	0.053446	1.030786	-2.89787	-3.12014	-0.0353
1.0933	4.713556	4.870535	0.055097	1.287788	-3.1646	-3.48967	-0.03948
1.287788	5.08725	5.291463	0.059858	1.54618	-3.42716	-3.8592	-0.04366
1.54618	5.531794	5.805467	0.065673	1.803182	-3.67999	-4.219	-0.04773
1.803182	5.927716	6.277795	0.071016	2.061573	-3.90365	-4.56074	-0.05159
2.061573	6.318082	6.745955	0.076312	2.293569	-4.09536	-4.8622	-0.055
2.318575	6.70289	7.208559	0.081545	2.318575	-4.1162	-4.89415	-0.05536

Suction Side				Pressure Side			
x[mm]	y[mm]	s[mm]	s/C	x[mm]	y[mm]	s[mm]	s/C
2.576966	7.083531	7.668384	0.086746	2.576966	-4.32319	-5.22478	-0.0591
2.833968	7.454447	8.119874	0.091854	2.833968	-4.52879	-5.55402	-0.06283
2.961774	7.630876	8.337978	0.094321	3.092359	-4.733	-5.88326	-0.06655
3.092359	7.804526	8.554694	0.096773	3.349361	-4.93722	-6.2125	-0.07028
3.349361	8.139323	8.97701	0.10155	3.607752	-5.14421	-6.54313	-0.07402
3.607752	8.467174	9.39516	0.10628	3.864754	-5.3512	-6.87376	-0.07776
3.864754	8.788079	9.806363	0.110932	4.123146	-5.55819	-7.20439	-0.0815
4.123146	9.097871	10.20923	0.115489	4.380148	-5.76518	-7.53363	-0.08522
4.380148	9.397938	10.60376	0.119952	4.638539	-5.97217	-7.86565	-0.08898
4.638539	9.684113	10.98996	0.124321	4.895541	-6.17916	-8.19489	-0.0927
4.895541	9.955007	11.36366	0.128548	5.006677	-6.26668	-8.33659	-0.09431
5.153932	10.21201	11.72763	0.132665	5.153932	-6.38476	-8.52552	-0.09644
5.410934	10.45234	12.07909	0.136641	5.410934	-6.59314	-8.85615	-0.10018
5.669325	10.68017	12.42362	0.140539	5.669325	-6.80013	-9.18678	-0.10392
5.926327	10.8955	12.7598	0.144342	5.926327	-7.00712	-9.51741	-0.10766
6.173605	11.08721	13.07237	0.147878	6.184718	-7.2155	-9.84943	-0.11142
6.184718	11.09554	13.08626	0.148035	6.44172	-7.4225	-10.1801	-0.11516
6.44172	11.28308	13.40439	0.151633	6.698722	-7.63088	-10.5107	-0.1189
6.698722	11.46229	13.71696	0.155169	6.957114	-7.83926	-10.8427	-0.12266
6.957114	11.63038	14.02536	0.158658	7.214116	-8.04764	-11.1733	-0.1264
7.214116	11.78875	14.32821	0.162084	7.472507	-8.2574	-11.5054	-0.13015
7.472507	11.93878	14.62689	0.165463	7.729509	-8.46578	-11.8374	-0.13391
7.729509	12.08326	14.9214	0.168794	7.9879	-8.67555	-12.1694	-0.13766
7.9879	12.22218	15.21452	0.17211	8.244902	-8.88532	-12.5014	-0.14142
8.244902	12.35693	15.50486	0.175394	8.503293	-9.09509	-12.8334	-0.14517

Suction Side				Pressure Side			
x[mm]	y[mm]	s[mm]	s/C	x[mm]	y[mm]	s[mm]	s/C
8.503293	12.48474	15.79243	0.178647	8.760295	-9.30625	-13.1668	-0.14895
8.760295	12.60977	16.0786	0.181885	9.018686	-9.51741	-13.5002	-0.15272
9.018686	12.73063	16.36478	0.185122	9.128433	-9.60771	-13.6419	-0.15432
9.275688	12.84732	16.64678	0.188312	9.275688	-9.72857	-13.8337	-0.15649
9.53408	12.95568	16.92601	0.191471	9.53408	-9.94112	-14.1671	-0.16026
9.791082	13.05848	17.20385	0.194614	9.791082	-10.1537	-14.5005	-0.16403
10.04947	13.15433	17.47891	0.197725	10.04947	-10.3676	-14.8367	-0.16784
10.30647	13.24324	17.7512	0.200805	10.30647	-10.5801	-15.1701	-0.17161
10.34954	13.25436	17.79565	0.201308	10.56487	-10.7955	-15.5063	-0.17541
10.56487	13.32382	18.02209	0.20387	10.82187	-11.0108	-15.8424	-0.17921
10.82187	13.39744	18.28882	0.206887	11.08026	-11.2261	-16.1786	-0.18302
11.08026	13.46274	18.55554	0.209904	11.33726	-11.4428	-16.5148	-0.18682
11.33726	13.51969	18.8181	0.212874	11.59565	-11.6596	-16.851	-0.19062
11.59565	13.57248	19.08205	0.21586	11.85265	-11.8777	-17.1886	-0.19444
11.85265	13.61972	19.34322	0.218815	12.11105	-12.0958	-17.5261	-0.19826
12.11105	13.66	19.60578	0.221785	12.36805	-12.3153	-17.8651	-0.20209
12.36805	13.69612	19.86417	0.224708	12.62644	-12.5348	-18.2041	-0.20593
12.62644	13.7253	20.12534	0.227662	12.88344	-12.7556	-18.543	-0.20976
12.88344	13.7503	20.38373	0.230585	13.14183	-12.9779	-18.8834	-0.21361
13.14183	13.76975	20.64212	0.233508	13.19184	-13.021	-18.9501	-0.21437
13.39883	13.78503	20.89912	0.236415	13.39883	-13.2002	-19.2237	-0.21746
13.65584	13.79615	21.15752	0.239338	13.65584	-13.4238	-19.5641	-0.22131
13.83921	13.80031	21.34089	0.241413	13.91423	-13.6475	-19.9058	-0.22518
13.91423	13.80309	21.41591	0.242261	14.17123	-13.8739	-20.2476	-0.22905
14.17123	13.80587	21.67291	0.245169	14.42962	-14.099	-20.5907	-0.23293

Suction Side				Pressure Side			
x[mm]	y[mm]	s[mm]	s/C	x[mm]	y[mm]	s[mm]	s/C
14.42962	13.80309	21.9313	0.248092	14.68662	-14.3268	-20.9339	-0.23681
14.68662	13.79753	22.1883	0.250999	14.94501	-14.5533	-21.2784	-0.24071
14.94501	13.78503	22.44669	0.253922	15.20202	-14.7839	-21.6229	-0.2446
15.20202	13.76697	22.7037	0.256829	15.46041	-15.0159	-21.9702	-0.24853
15.46041	13.74336	22.96348	0.259768	15.71741	-15.2506	-22.3189	-0.25248
15.71741	13.71279	23.22187	0.262691	15.9758	-15.4868	-22.669	-0.25644
15.9758	13.67806	23.48304	0.265645	16.2328	-15.7257	-23.019	-0.2604
16.2328	13.63639	23.74421	0.2686	16.49119	-15.9633	-23.3705	-0.26437
16.49119	13.59054	24.00538	0.271554	16.7482	-16.2036	-23.722	-0.26835
16.7482	13.53636	24.26793	0.274524	17.00659	-16.444	-24.0748	-0.27234
17.00659	13.47663	24.53327	0.277526	17.13856	-16.5676	-24.2554	-0.27438
17.26359	13.40856	24.8	0.280543	17.26359	-16.6843	-24.4277	-0.27633
17.52198	13.33354	25.06811	0.283576	17.52198	-16.926	-24.7805	-0.28032
17.78037	13.25019	25.3404	0.286656	17.78037	-17.1677	-25.1348	-0.28433
18.03737	13.15989	25.61268	0.289736	18.03737	-17.4122	-25.489	-0.28834
18.29437	13.06265	25.88774	0.292848	18.29437	-17.6553	-25.8433	-0.29234
18.55277	12.96263	26.16419	0.295975	18.55277	-17.8998	-26.1989	-0.29637
18.80977	12.85427	26.44342	0.299134	18.80977	-18.1457	-26.5546	-0.30039
19.06816	12.73896	26.72682	0.30234	19.06816	-18.393	-26.913	-0.30445
19.32516	12.61671	27.0116	0.305561	19.32516	-18.6403	-27.2686	-0.30847
19.55716	12.49863	27.27139	0.3085	19.58355	-18.889	-27.627	-0.31252
19.58355	12.48474	27.30056	0.30883	19.84055	-19.1376	-27.9854	-0.31658
19.84055	12.34165	27.59507	0.312161	20.09756	-19.3877	-28.3438	-0.32063
20.09756	12.18884	27.89375	0.31554	20.35595	-19.6391	-28.7037	-0.3247
20.35595	12.03047	28.19798	0.318982	20.61295	-19.8906	-29.0635	-0.32877

Suction Side				Pressure Side			
x[mm]	y[mm]	s[mm]	s/C	x[mm]	y[mm]	s[mm]	s/C
20.61295	11.86516	28.50222	0.322423	20.87134	-20.1448	-29.426	-0.33287
20.87134	11.6929	28.8134	0.325943	20.9672	-20.2393	-29.5608	-0.3344
21.12834	11.51508	29.12597	0.329479	21.12834	-20.4018	-29.79	-0.33699
21.38673	11.32754	29.44548	0.333094	21.38673	-20.6602	-30.1554	-0.34112
21.64374	11.13166	29.76778	0.33674	21.64374	-20.9186	-30.5193	-0.34524
21.90213	10.92745	30.09841	0.34048	21.90213	-21.1811	-30.8875	-0.34941
22.15913	10.7149	30.43182	0.344251	22.15913	-21.4437	-31.2556	-0.35357
22.41752	10.49402	30.77078	0.348086	22.41752	-21.709	-31.6251	-0.35775
22.67452	10.26897	31.11252	0.351952	22.67452	-21.9758	-31.9961	-0.36195
22.93291	10.03836	31.45843	0.355865	22.93291	-22.2439	-32.3684	-0.36616
23.18992	9.798028	31.81129	0.359856	23.18992	-22.5162	-32.7434	-0.3704
23.333	9.660497	32.00995	0.362103	23.44831	-22.7898	-33.1199	-0.37466
23.44831	9.549361	32.1697	0.363911	23.70531	-23.0649	-33.4964	-0.37892
23.70531	9.288191	32.53645	0.368059	23.9637	-23.3427	-33.8756	-0.38321
23.9637	9.015908	32.91154	0.372302	24.22209	-23.6233	-34.2563	-0.38751
24.22209	8.7339	33.29357	0.376624	24.47909	-23.9054	-34.6383	-0.39184
24.47909	8.443558	33.68115	0.381009	24.63468	-24.079	-34.8717	-0.39448
24.7361	8.146269	34.0743	0.385456	24.7361	-24.1888	-35.0203	-0.39616
24.99449	7.842034	34.47439	0.389982	24.99449	-24.4763	-35.4079	-0.40054
25.25149	7.532242	34.87587	0.394523	25.25149	-24.7667	-35.7955	-0.40493
25.50988	7.209948	35.28985	0.399206	25.50988	-25.0584	-36.1845	-0.40933
25.76688	6.877929	35.70939	0.403952	25.76688	-25.3529	-36.5762	-0.41376
26.02527	6.536186	36.13726	0.408793	26.02527	-25.6516	-36.9708	-0.41822
26.28227	6.184718	36.57347	0.413727	26.28227	-25.9516	-37.3653	-0.42268
26.37535	6.056912	36.73184	0.415519	26.54067	-26.2545	-37.764	-0.42719

Suction Side				Pressure Side			
x[mm]	y[mm]	s[mm]	s/C	x[mm]	y[mm]	s[mm]	s/C
26.54067	5.827694	37.01384	0.418709	26.79767	-26.5615	-38.1641	-0.43172
26.79767	5.463724	37.45978	0.423753	27.05467	-26.8699	-38.5656	-0.43626
27.05467	5.091418	37.91127	0.42886	27.31306	-27.1825	-38.9712	-0.44085
27.31306	4.712166	38.37109	0.434062	27.57006	-27.4978	-39.3783	-0.44546
27.57006	4.32319	38.83648	0.439327	27.82845	-27.8146	-39.7867	-0.45008
27.82845	3.923101	39.31297	0.444717	28.07018	-28.1174	-40.1743	-0.45446
28.08546	3.511898	39.7978	0.450201	28.08546	-28.1369	-40.1993	-0.45474
28.34385	3.092359	40.29097	0.45578	28.34385	-28.4619	-40.6147	-0.45944
28.60085	2.663096	40.79108	0.461438	28.60085	-28.7898	-41.0314	-0.46416
28.85924	2.225498	41.29953	0.467189	28.85924	-29.1218	-41.4509	-0.4689
28.94398	2.081022	41.46623	0.469075	29.11624	-29.4566	-41.8733	-0.47368
29.11624	1.780954	41.81214	0.472988	29.37463	-29.7942	-42.2984	-0.47849
29.37463	1.328075	42.33448	0.478897	29.63164	-30.1373	-42.7276	-0.48334
29.63164	0.865472	42.86377	0.484884	29.89003	-30.4832	-43.1597	-0.48823
29.89003	0.394533	43.4	0.49095	30.14703	-30.8333	-43.5931	-0.49313
30.14703	-0.08613	43.94595	0.497126	30.40542	-31.1862	-44.0307	-0.49808
30.40542	-0.57652	44.50024	0.503396	30.66381	-31.5446	-44.4725	-0.50308
30.66381	-1.07246	45.0587	0.509714	30.92081	-31.9044	-44.9142	-0.50808
30.92081	-1.57674	45.6255	0.516126	31.1792	-32.2697	-45.3629	-0.51316
31.1792	-2.08797	46.19785	0.5226	31.24866	-32.3697	-45.4838	-0.51452
31.18198	-2.0963	46.20618	0.522694	31.43621	-32.6406	-45.813	-0.51825
31.43621	-2.6117	46.78131	0.5292	31.69321	-33.0129	-46.2659	-0.52337
31.69321	-3.14793	47.37589	0.535926	31.9516	-33.3908	-46.7244	-0.52856
31.9516	-3.69944	47.98575	0.542825	32.2086	-33.7742	-47.1856	-0.53377
32.2086	-4.26207	48.60394	0.549818	32.46699	-34.1618	-47.6509	-0.53904

Suction Side				Pressure Side			
x[mm]	y[mm]	s[mm]	s/C	x[mm]	y[mm]	s[mm]	s/C
32.46699	-4.83442	49.23186	0.556921	32.724	-34.5522	-48.1191	-0.54433
32.724	-5.41232	49.86394	0.564072	32.98239	-34.9481	-48.5914	-0.54968
32.98239	-5.99301	50.5002	0.571269	33.23939	-35.3482	-49.0665	-0.55505
33.15465	-6.38615	50.92946	0.576125	33.49639	-35.7538	-49.5472	-0.56049
33.23939	-6.57786	51.13784	0.578482	33.75478	-36.1637	-50.032	-0.56597
33.49639	-7.17244	51.7866	0.585821	34.01178	-36.579	-50.5196	-0.57149
33.75478	-7.77674	52.44369	0.593254	34.15209	-36.8069	-50.7878	-0.57452
34.01178	-8.39494	53.11328	0.600829	34.27017	-37	-51.0142	-0.57708
34.27017	-9.03119	53.79955	0.608592	34.52718	-37.4264	-51.5115	-0.58271
34.52718	-9.68411	54.50109	0.616528	34.78557	-37.8557	-52.013	-0.58838
34.78557	-10.3468	55.21236	0.624574	35.04257	-38.2891	-52.5173	-0.59409
34.9481	-10.7691	55.66524	0.629697	35.30096	-38.7267	-53.0244	-0.59982
35.04257	-11.015	55.92919	0.632683	35.55796	-39.1713	-53.5384	-0.60564
35.30096	-11.6929	56.65435	0.640886	35.81635	-39.6214	-54.0579	-0.61152
35.55796	-12.3792	57.38646	0.649168	36.07336	-40.0784	-54.5817	-0.61744
35.81635	-13.0793	58.13246	0.657607	36.33175	-40.5438	-55.1137	-0.62346
36.07336	-13.7934	58.89236	0.666203	36.58875	-41.0161	-55.6514	-0.62954
36.33175	-14.5213	59.66475	0.674941	36.79991	-41.4065	-56.0959	-0.63457
36.57208	-15.2173	60.40103	0.68327	36.84714	-41.494	-56.1945	-0.63568
36.58875	-15.2645	60.45104	0.683835	37.10553	-41.9747	-56.7405	-0.64186
36.84714	-16.0203	61.24983	0.692871	37.36253	-42.4637	-57.2934	-0.64812
37.10553	-16.7885	62.05973	0.702033	37.62093	-42.9555	-57.8491	-0.6544
37.36253	-17.5692	62.88214	0.711336	37.87793	-43.4542	-58.4103	-0.66075
37.62093	-18.3611	63.71427	0.72075	38.13493	-43.9585	-58.9757	-0.66715
37.87793	-19.1682	64.56168	0.730336	38.39332	-44.4711	-59.5494	-0.67364

Suction Side				Pressure Side			
x[mm]	y[mm]	s[mm]	s/C	x[mm]	y[mm]	s[mm]	s/C
38.04602	-19.7058	65.1257	0.736716	38.65032	-44.9892	-60.1287	-0.68019
38.13493	-19.9892	65.42298	0.740079	38.90871	-45.5144	-60.7136	-0.68681
38.39332	-20.8186	66.29123	0.749901	39.16572	-46.045	-61.3026	-0.69347
38.65032	-21.659	67.16921	0.759833	39.20878	-46.1353	-61.4026	-0.6946
38.90871	-22.5078	68.05691	0.769875	39.42411	-46.5827	-61.9	-0.70023
39.16572	-23.3677	68.95433	0.780026	39.68111	-47.1272	-62.5015	-0.70703
39.42411	-24.2346	69.8587	0.790257	39.9395	-47.6801	-63.1127	-0.71395
39.68111	-25.1112	70.77279	0.800597	40.1965	-48.2386	-63.7268	-0.72089
39.9395	-25.9961	71.69383	0.811016	40.4535	-48.8068	-64.3505	-0.72795
40.1965	-26.8921	72.62599	0.821561	40.7119	-49.3805	-64.9798	-0.73507
40.4535	-27.7965	73.56648	0.8322	40.9689	-49.9612	-65.6147	-0.74225
40.7119	-28.7078	74.51391	0.842918	41.22729	-50.5488	-66.2565	-0.74951
40.73551	-28.7898	74.60004	0.843892	41.4065	-50.9614	-66.7066	-0.7546
40.9689	-29.6275	75.46968	0.853729	41.48429	-51.1448	-66.9053	-0.75685
41.22729	-30.5513	76.42823	0.864573	41.74268	-51.7477	-67.561	-0.76426
41.48429	-31.4848	77.3965	0.875526	41.99968	-52.3589	-68.225	-0.77178
41.74268	-32.4295	78.37589	0.886605	42.25807	-52.9785	-68.896	-0.77937
41.98718	-33.3422	79.32054	0.897291	42.51508	-53.6037	-69.5725	-0.78702
41.99968	-33.388	79.36777	0.897826	42.77347	-54.2371	-70.256	-0.79475
42.25807	-34.3619	80.37633	0.909235	43.03047	-54.8817	-70.9506	-0.80261
42.51508	-35.3482	81.39462	0.920754	43.28886	-55.5374	-71.6549	-0.81058
42.77347	-36.3443	82.42401	0.932398	43.42084	-55.875	-72.0175	-0.81468
43.03047	-37.35	83.46175	0.944137	43.54725	-56.2015	-72.3676	-0.81864
43.17911	-37.9293	84.06049	0.950911	43.80425	-56.8711	-73.0844	-0.82675
43.28886	-38.3628	84.50781	0.955971	44.06265	-57.5434	-73.8054	-0.8349

Suction Side				Pressure Side			
x[mm]	y[mm]	s[mm]	s/C	x[mm]	y[mm]	s[mm]	s/C
43.54725	-39.3797	85.55666	0.967836	44.31965	-58.22	-74.5292	-0.84309
43.80425	-40.4021	86.61106	0.979763	44.57804	-58.8993	-75.2557	-0.85131
44.06265	-41.4301	87.67102	0.991754	44.83504	-59.5828	-75.9851	-0.85956
44.31965	-42.4623	88.73515	1.003791	45.09204	-60.2732	-76.7227	-0.8679
44.33493	-42.5262	88.80044	1.00453	45.30042	-60.8372	-77.3229	-0.87469
44.57804	-43.4986	89.80206	1.01586	45.35043	-60.9734	-77.4687	-0.87634
44.83504	-44.5433	90.87869	1.028039	45.60744	-61.6735	-78.2147	-0.88478
45.09204	-45.5935	91.95948	1.040266	45.86583	-62.3765	-78.9635	-0.89325
45.35043	-46.6563	93.05278	1.052633	46.12283	-63.0766	-79.7095	-0.90169
45.46157	-47.1258	93.53623	1.058102	46.38122	-63.7796	-80.4583	-0.91016
45.60744	-47.7357	94.16275	1.06519	46.63822	-64.4811	-81.2057	-0.91862
45.86583	-48.8026	95.26022	1.077604	46.89522	-65.1813	-81.9517	-0.92706
46.12283	-49.8681	96.3563	1.090003	47.13	-65.8175	-82.6296	-0.93472
46.38122	-50.935	97.45516	1.102434	47.15362	-65.8842	-82.7005	-0.93553
46.57015	-51.7171	98.25951	1.111533	47.41062	-66.5844	-83.4465	-0.94396
46.63822	-52.0005	98.55124	1.114833	47.66901	-67.2873	-84.1952	-0.95243
46.89522	-53.0647	99.64593	1.127216	47.92601	-67.9874	-84.9412	-0.96087
47.15362	-54.1316	100.7434	1.139631	48.1844	-68.6904	-85.69	-0.96934
47.41062	-55.1957	101.8381	1.152015	48.4414	-69.3905	-86.436	-0.97778
47.66901	-56.264	102.9369	1.164445	48.6998	-70.0949	-87.1862	-0.98627
47.6829	-56.3209	102.9953	1.165105	48.9568	-70.795	-87.9308	-0.99469
47.92601	-57.3281	104.0316	1.176828	48.95819	-70.7978	-87.935	-0.99474
48.1844	-58.3964	105.1305	1.189259	49.21519	-71.4952	-88.6782	-1.00315
48.4414	-59.4605	106.2252	1.201642	49.39995	-72.0008	-89.2158	-1.00923
48.6998	-60.5288	107.324	1.214073	49.47219	-72.1801	-89.4089	-1.01141

Suction Side				Pressure Side			
x[mm]	y[mm]	s[mm]	s/C	x[mm]	y[mm]	s[mm]	s/C
48.79565	-60.9234	107.7311	1.218677	49.61528	-72.3593	-89.6381	-1.01401
48.9568	-61.593	108.4187	1.226456	49.84727	-72.5649	-89.9493	-1.01753
49.21519	-62.6571	109.5148	1.238855	50.11539	-72.6718	-90.2369	-1.02078
49.47219	-63.7254	110.6137	1.251286	50.38351	-72.7163	-90.5092	-1.02386
49.73058	-64.7881	111.707	1.263653	50.65162	-72.6621	-90.7828	-1.02696
49.90562	-65.5147	112.4544	1.272108				
49.98897	-65.8564	112.8058	1.276084				
50.24597	-66.9205	113.9005	1.288467				
50.50437	-67.9888	114.9994	1.300898				
50.76137	-69.053	116.0941	1.313281				
51.01976	-70.1213	117.1929	1.325712				
51.36567	-71.5549	118.6682	1.342401				
51.37956	-71.7341	118.8474	1.344428				
51.36567	-71.9119	119.0267	1.346455				
51.2587	-72.1801	119.3156	1.349724				
51.14201	-72.3593	119.5295	1.352144				
50.91974	-72.5551	119.8254	1.355491				
50.65162	-72.6621	120.1144	1.35876				

# Appendix B

## Double Passage Vane Cascade Wall Coordinates

The  $x$ - $y$  manufacturing coordinates of the double passage vane cascade walls are presented.

Lower wall		Upper wall	
x [cm]	y [cm]	x [cm]	y [cm]
-19.1928	-7.274	-19.2791	5.3334
-18.9098	-7.2688	-18.8171	5.3556
-18.5961	-7.2561	-18.3361	5.376
-18.294	-7.2479	-17.8513	5.3958
-17.9794	-7.2368	-17.3455	5.4143
-17.6719	-7.2297	-16.821	5.4317
-17.3593	-7.2213	-16.2806	5.4487
-17.044	-7.2156	-15.7274	5.4667
-16.7081	-7.2058	-15.1657	5.4863
-16.3597	-7.197	-14.6543	5.5049

APPENDIX B. DOUBLE PASSAGE VANE CASCADE WALL COORDINATES163

Lower wall		Upper wall	
x [cm]	y [cm]	x [cm]	y [cm]
-16.0012	-7.1855	-14.1935	5.5235
-15.6404	-7.1753	-13.7761	5.5404
-15.2706	-7.1652	-13.374	5.5572
-14.8858	-7.1569	-12.9888	5.5717
-14.4915	-7.146	-12.5393	5.5887
-14.0794	-7.1376	-12.0324	5.6052
-13.6553	-7.1284	-11.4585	5.6262
-13.2413	-7.1157	-10.8778	5.645
-12.8714	-7.1001	-10.2603	5.6661
-12.4892	-7.0858	-9.672	5.6843
-12.0976	-7.0703	-9.0894	5.7053
-11.6913	-7.0553	-8.5616	5.7217
-11.2573	-7.0425	-8.0566	5.7383
-10.7766	-7.0319	-7.6129	5.7532
-10.3514	-7.0192	-7.1986	5.7697
-9.9438	-7.0067	-6.8332	5.7832
-9.5536	-6.9946	-6.4858	5.7971
-9.1807	-6.9826	-6.1559	5.8108
-8.8249	-6.9709	-5.8348	5.8231
-8.4351	-6.9618	-5.5224	5.8342
-8.0867	-6.9504	-5.213	5.8444
-7.7527	-6.9393	-4.9066	5.8543
-7.4331	-6.9287	-4.5885	5.8673
-7.1278	-6.9186	-4.2704	5.8803
-6.8367	-6.9089	-3.9517	5.8935

APPENDIX B. DOUBLE PASSAGE VANE CASCADE WALL COORDINATES164

Lower wall		Upper wall	
x [cm]	y [cm]	x [cm]	y [cm]
-6.5222	-6.9021	-3.6455	5.9079
-6.2378	-6.8925	-3.3498	5.8621
-5.9603	-6.8828	-3.0947	5.8148
-5.6901	-6.8732	-2.8655	5.7689
-5.4271	-6.8638	-2.6624	5.7269
-5.1715	-6.8547	-2.4633	5.6857
-4.8969	-6.8489	-2.2692	5.6454
-4.6492	-6.841	-2.0665	5.6032
-4.4278	-6.8311	-1.855	5.5564
-4.2322	-6.8191	-1.6349	5.5076
-4.0366	-6.807	-1.4379	5.4729
-3.8406	-6.795	-1.2611	5.474
-3.6209	-6.7856	-1.1031	5.4725
-3.3775	-6.7787	-0.9637	5.4701
-3.1105	-6.7743	-0.8433	5.4679
-2.8707	-6.7676	-0.7251	5.4648
-2.6577	-6.7587	-0.6141	5.4618
-2.4732	-6.7082	-0.5144	5.4591
-2.3145	-6.6802	-0.4293	5.4556
-2.1823	-6.6569	-0.3605	5.452
-2.0514	-6.6338	-0.3032	5.4489
-1.9217	-6.6109	-0.2535	5.4463
-1.793	-6.5864	-0.2061	5.4437
-1.6651	-6.5616	-0.1631	5.4415
-1.5375	-6.5368	-0.119	5.439

APPENDIX B. DOUBLE PASSAGE VANE CASCADE WALL COORDINATES165

Lower wall		Upper wall	
x [cm]	y [cm]	x [cm]	y [cm]
-1.4097	-6.5121	-0.0757	5.4354
-1.2812	-6.4872	-0.0415	5.4326
-1.135	-6.4591	-0.0135	5.4303
-0.9706	-6.4276	0.017	5.4278
-0.7881	-6.3928	0.0391	5.4259
-0.5878	-6.3545	0.0562	5.4245
-0.3704	-6.3129	0.0819	5.4224
-0.1646	-6.2734	0.1068	5.4204
0.0481	-6.2327	0.1286	5.4186
0.2809	-6.1918	0.1587	5.4161
0.5364	-6.1474	0.1928	5.4132
0.8425	-6.1007	0.2243	5.4103
1.2144	-6.0505	0.2591	5.4061
1.6228	-6.0224	0.2949	5.4019
2.0389	-6.0297	0.3294	5.3978
2.4655	-6.0945	0.363	5.3938
2.8419	-6.2287	0.3976	5.3897
3.1551	-6.4252	0.4314	5.3857
3.4036	-6.649	0.4665	5.3815
3.6161	-6.9029	0.4992	5.3776
3.7737	-7.1346	0.5326	5.3736
3.9108	-7.3748	0.5648	5.3686
4.0371	-7.6371	0.5945	5.364
4.1646	-7.9482	0.6222	5.3596
4.2642	-8.2101	0.6515	5.355

APPENDIX B. DOUBLE PASSAGE VANE CASCADE WALL COORDINATES166

Lower wall		Upper wall	
x [cm]	y [cm]	x [cm]	y [cm]
4.3503	-8.481	0.6763	5.3511
4.4769	-8.9323	0.6998	5.3474
4.6381	-9.4216	0.7258	5.3433
4.8378	-10.0545	0.7491	5.3396
5.1012	-10.8566	0.7707	5.3363
5.4165	-11.8312	0.7959	5.3323
5.6754	-12.6321	0.8194	5.3286
5.8798	-13.2595	0.8401	5.3253
6.0299	-13.713	0.8651	5.3202
6.1143	-13.9965	0.8904	5.3151
6.1697	-14.1836	0.9152	5.3101
6.25	-14.4474	0.9446	5.3042
6.3547	-14.7883	0.9779	5.2975
6.4834	-15.2067	1.0103	5.291
6.6787	-15.8367	1.0453	5.284
6.8912	-16.5243	1.0807	5.2768
7.1219	-17.273	1.116	5.2697
		1.1501	5.2613
		1.1854	5.2525
		1.2193	5.2439
		1.2541	5.2352
		1.2877	5.2267
		1.322	5.2181
		1.355	5.2099
		1.3889	5.2005

APPENDIX B. DOUBLE PASSAGE VANE CASCADE WALL COORDINATES167

Lower wall		Upper wall	
x [cm]	y [cm]	x [cm]	y [cm]
		1.4217	5.1906
		1.4555	5.1803
		1.4884	5.1703
		1.5224	5.16
		1.5554	5.1891
		1.5894	5.1812
		1.6225	5.1735
		1.6564	5.1657
		1.6894	5.158
		1.7234	5.1501
		1.7563	5.1424
		1.79	5.1346
		1.8228	5.127
		1.8565	5.1173
		1.8893	5.1056
		1.9228	5.0936
		1.9555	5.0819
		1.989	5.07
		2.0214	5.0584
		2.0544	5.0466
		2.0857	5.0354
		2.1188	5.0236
		2.1532	5.0104
		2.1913	4.9957
		2.2317	4.98

APPENDIX B. DOUBLE PASSAGE VANE CASCADE WALL COORDINATES168

Lower wall		Upper wall	
x [cm]	y [cm]	x [cm]	y [cm]
		2.277	4.9625
		2.3227	4.9448
		2.3672	4.9276
		2.4082	4.9104
		2.4466	4.891
		2.4801	4.874
		2.5117	4.858
		2.5415	4.8428
		2.5715	4.8276
		2.6003	4.813
		2.6299	4.798
		2.6586	4.7826
		2.6879	4.7639
		2.7163	4.7458
		2.7452	4.7274
		2.773	4.7097
		2.8012	4.6917
		2.8283	4.6745
		2.8557	4.657
		2.8821	4.6401
		2.9082	4.6194
		2.9352	4.5972
		2.9628	4.5743
		2.9896	4.5522
		3.0169	4.5296

APPENDIX B. DOUBLE PASSAGE VANE CASCADE WALL COORDINATES 169

Lower wall		Upper wall	
x [cm]	y [cm]	x [cm]	y [cm]
		3.043	4.5081
		3.0702	4.4855
		3.0986	4.4615
		3.1303	4.4281
		3.1648	4.3915
		3.2048	4.3492
		3.2469	4.3048
		3.2896	4.2569
		3.3306	4.2015
		3.3684	4.1503
		3.4009	4.1064
		3.4298	4.0675
		3.4552	4.0286
		3.4792	3.9887
		3.5018	3.9512
		3.5244	3.9135
		3.5463	3.8772
		3.5687	3.8401
		3.5903	3.8004
		3.6123	3.7566
		3.6338	3.7138
		3.6555	3.6705
		3.6764	3.6288
		3.6983	3.5849
		3.7212	3.5326

APPENDIX B. DOUBLE PASSAGE VANE CASCADE WALL COORDINATES170

Lower wall		Upper wall	
x [cm]	y [cm]	x [cm]	y [cm]
		3.7466	3.4746
		3.7747	3.4105
		3.807	3.3344
		3.8421	3.2453
		3.8794	3.1505
		3.9177	3.0504
		3.9556	2.9511
		3.9913	2.856
		4.0241	2.7687
		4.0535	2.693
		4.0788	2.628
		4.1014	2.5721
		4.1214	2.5235
		4.1401	2.4778
		4.1578	2.4386
		4.176	2.3995
		4.1954	2.3582
		4.2167	2.313
		4.2405	2.2628
		4.2679	2.2115
		4.298	2.1626
		4.3302	2.0738
		4.3638	2.0088
		4.3983	1.9422
		4.4328	1.8756

APPENDIX B. DOUBLE PASSAGE VANE CASCADE WALL COORDINATES 171

Lower wall		Upper wall	
x [cm]	y [cm]	x [cm]	y [cm]
		4.4673	1.8072
		4.5018	1.7358
		4.5365	1.664
		4.5713	1.5921
		4.6062	1.5199
		4.6413	1.4423
		4.6768	1.3636
		4.7127	1.2842
		4.7492	1.2034
		4.7873	1.1133
		4.8243	1.024
		4.8671	0.9207
		4.9159	0.801
		4.9706	0.6576
		5.0353	0.4879
		5.1156	0.2634
		5.1986	0.026
		5.3008	-0.2807
		5.4206	-0.6522
		5.5749	-1.1269
		5.765	-1.6843
		5.998	-2.3321
		6.2675	-3.4025
		6.5803	-4.3906
		6.8798	-5.3446

APPENDIX B. DOUBLE PASSAGE VANE CASCADE WALL COORDINATES172

Lower wall		Upper wall	
x [cm]	y [cm]	x [cm]	y [cm]
		7.1557	-6.231
		7.4222	-7.0904
		7.6478	-7.8184
		9.8656	-16.541
		9.9253	-16.5367

# Bibliography

- [1] T. Arts, M. Lambert de Rouvroit, and A.W. Rutherford. Aero-thermal Investigation of a Highly-Loaded Transonic Linear Turbine Guide Vane Cascade. Technical Note 174, von Karman Institute for Fluid Dynamics, Rhode Saint Genèse, Belgium, September 1990.
- [2] M. Benson. *3D Velocity and Scalar Field Diagnostics Using Magnetic Resonance Imaging with Application in Film-Cooling*. PhD Thesis, Stanford University, Stanford, CA, March 2011.
- [3] M.J. Benson, C.J. Elkins, and J.K. Eaton. 3D Velocity and Scalar Field Diagnostics Using Magnetic Resonance Imaging with Applications to Film-Cooling. Turbulent Flow Report 123, Stanford University, Stanford, CA, April 2011.
- [4] M.J. Benson, C.J. Elkins, and J.K. Eaton. Measurements of 3D velocity and scalar field for a film-cooled airfoil trailing edge. *Exp Fluids*, 51(2):443–455, March 2011.
- [5] M.J. Benson, C.J. Elkins, P. Mobley, and J.K. Eaton. Three-dimensional concentration field measurements in a mixing layer using magnetic resonance imaging. *Exp Fluids*, 49(1):43–55, September 2010.

- [6] M.J. Benson, C.J. Elkins, S.D. Yapa, J.B. Ling, and J.K. Eaton. Effects of varying Reynolds number, blowing ratio, and internal geometry on trailing edge cutback film cooling. *Exp Fluids*, 52(1):1415–1430, January 2012.
- [7] A. Binder and R. Romey. Secondary flow effects and mixing of the wake behind a turbine stator. *J Engineering for Power*, 105(1):40–46, April 1996.
- [8] D.G. Bogard and K.A. Thole. Gas turbine film cooling. *J Propulsion and Power*, 22(2):249–270, March-April 2006.
- [9] G.L. Brown and A. Roshko. On density effects and large structure in turbulent mixing layers. *J Fluid Mech*, 63(4):775–816, July 1974.
- [10] C.U. Buice and J.K. Eaton. Turbulent heat transport in a perturbed channel flow. *J Heat Transfer*, 121(2):322–325, May 1999.
- [11] E.M. Cherry, G. Iaccarino, C.J. Elkins, and J.K. Eaton. Separated flow in a three-dimensional diffuser: preliminary validation. Annual research briefs, Center for Turbulence Research, Stanford, CA, 2006.
- [12] F. Coletti, M.J. Benson, J. Ling, C.J. Elkins, and J.K. Eaton. Turbulent transport in an inclined jet in crossflow. *Int J Heat Fluid Flow*, 43(1):149–160, June 2013.
- [13] F. Coletti, K. Muramatsu, D. Schiavazzi, C.J. Elkins, and J.K. Eaton. Fluid flow and scalar transport through porous fins. *Phys Fluids*, 26(1):055104, May 2014.
- [14] T.E. Conturo and G.D. Smith. Signal-to-noise in phase angle reconstruction: Dynamic range extension using phase reference offsets. *Magnetic Resonance in Medicine*, 15(3):420–437, September 1990.

- [15] K.H. Dellimore, A.W. Marshall, and C.P. Cadou. Influence of compressibility on film-cooling performance. *J Thermophysics and Heat Transfer*, 24(3):506–515, July 2010.
- [16] D.J. Dorney, K.L. Gundy-Burlet, and D.L. Sondak. A survey of hot streak experiments and simulations. *International Journal of Turbo and Jet Engines*, 16(1):1–16, March 1999.
- [17] C.J. Elkins. *Heat Transfer in the Rotating Disk Boundary Layer*. PhD Thesis, Stanford University, Stanford, CA, April 1997.
- [18] C.J. Elkins and M.T. Alley. Magnetic resonance velocimetry: applications of magnetic resonance imaging in the measurement of fluid motion. *Exp Fluids*, 43.
- [19] C.J. Elkins, M.T. Alley, L. SaeTRAN, and J.K. Eaton. Three-dimensional magnetic resonance velocimetry measurements of turbulence quantities in complex flow. *Exp Fluids*, 46(1):285–296.
- [20] C.J. Elkins, M. Markl, N. Pelc, and J.K. Eaton. 4D magnetic resonance velocimetry for mean velocity measurements in complex turbulent flows. *Exp Fluids*, 34(4):494–503, April 2003.
- [21] J.C. Gatenby and J.C. Gore. Characterization of turbulent flows by nmr measurements with pulsed gradients. *J Magn Reson A*, 110(1):26–32, September 1994.
- [22] R.J. Goldstein and R.A. Spores. Turbulent transport on the endwall in the region between adjacent turbine blades. *J Heat Transfer*, 110(4):862–869, November 1988.
- [23] R.J. Goldstein, Ed. *Fluid Mechanics Measurements*. Taylor and Francis, 1101 Vermont Ave, NW, Suite 200, Washington DC 20005-3521, 1996.

- [24] S. Grundmann, F. Wasserman, R. Lorenz, B. Jung, and C. Tropea. Experimental investigation of helical structures in swirling flows. *Int J Heat Fluid Flow*, 37(1):51–63, October 2012.
- [25] G. Iaccarino and C.J. Elkins. Towards rapid analysis of turbulent flows in complex internal passages. *Flow Turbulence Combustion*, 77(1):27–39, April 2006.
- [26] E. Issakhanian, C.J. Elkins, and J.K. Eaton. In-hole and mainflow velocity measurements of low-momentum jets in crossflow emanating from short holes. *Exp Fluids*, 53(1):1765–1778, October 2012.
- [27] S. Jenkins and D.G. Bogard. Superposition predictions of reduction of hot streaks by coolant from a film-cooled guide vane. *J Turbomach*, 131(1):041002–1 – 041002–9, October 2009.
- [28] S. Jenkins, K. Varadarajan, and D.G. Bogard. The effects of high mainstream turbulence in turbine vane film cooling on the dispersion of a simulated hot streak. *J Turbomach.*, 126(1):203–211, January 2004.
- [29] S.C. Jenkins and D.G. Bogard. Scaling of guide vane coolant profiles and the reduction of a simulated hot streak. *J Turbomach*, 129(1):619–627, July 2007.
- [30] M.B. Kang, A. Kohli, and K.A. Thole. Heat transfer and endwall measurements in the leading edge region of a stator vane endwall. *J Turbomach.*, 121(3):558–568, July 1999.
- [31] M.B. Kang and K.A. Thole. Flowfield measurements in the endwall region of a stator vane. *Transactions of the ASME*, 122(3):458–466, November 2000.
- [32] L. Kaufman, D.M. Kramer, L.E. Crooks, and D.A. Ortendahl. Measuring signal-to-noise ratios in MR imaging. *Radiology*, 173(1):265–267, September 1989.

- [33] P.M. Kodzwa, A. Vicharelli, G. Medic, C.J. Elkins, J.K. Eaton, G.M. Laskowski, and P.A. Durbin. Evaluation of alternatives for two-dimensional linear cascade facilities. *J Turbomachinery*, 131(1):031001–1 – 031001–11, July 2009.
- [34] M. Kurosaka, J.B. Gertz, J.E. Graham, J.R. Goodman, P. Sundaram, W.C. Riner, H. Kuroda, and W.L. Hankey. Energy separation in a vortex street. *J Fluid Mech*, 178(1):1–29, May 1987.
- [35] R.W. Ladenburg. *Physical Measurements in Gas Dynamics and Combustion, Part 1*. Princeton University Press, Princeton, NJ, 1954.
- [36] L.S. Langston. Crossflows in a turbine cascade passage. *Transactions of the ASME*, 102(4):866–874, October 1980.
- [37] L.S. Langston, M.L. Nice, and R.M. Hooper. Three-dimensional flow within a turbine cascade passage. *J Engineering for Power*, 99(1):21–28, January 1977.
- [38] G.M. Laskowski, A. Vicharelli, G. Medic, C.J. Elkins, J.K. Eaton, and P.A. Durbin. Inverse design of and experimental measurements in a double-passage transonic turbine cascade model. *J Turbomachinery*, 127(1):619–626, July 2005.
- [39] J. Ling. *Improvements in Turbulent Scalar Mixing Modeling for Trailing Edge Slot Film Cooling Geometries: A combined experimental and computational approach*. PhD Thesis, Stanford University, Stanford, CA, July 2014.
- [40] J.B. Ling, S.D. Yapa, M.J. Benson, C.J. Elkins, and J.K. Eaton. Three-dimensional velocity and scalar field measurements of an airfoil trailing edge with slot film cooling. *J Turbomach*, 135(3):031018–1 – 031018–8, May 2013.
- [41] K.P. Lo, C.J. Elkins, and J.K. Eaton. Separation control in a conical diffuser with an annular inlet: center body wake separation. *Exp Fluids*, 53(1):1317–1326, August 2012.

- [42] M. Markl, F.P. Chan, M.T. Alley, K.L. Wedding, M.T. Draney, C.J. Elkins, D.W. Parker, R. Wicker, C.A. Taylor, R.J. Herfkens, and N.J. Pelc. Time-resolved three-dimensional phase-contrast mri. *J Magnetic Resonance Imaging*, 17(4):499–506, April 2003.
- [43] Dwight G. Nishimura. *Principles of Magnetic Resonance Imaging*. www.lulu.com, Raleigh, NC, 2010.
- [44] G. Oates, editor. *Aerodynamics of Aircraft Engine Components*, volume 2 of *AIAA Education Series*, Chap. 5, pages 274–328. American Institute of Aeronautics and Astronautics, Inc., 1633 Broadway, New York, NY 10019, 1<sup>st</sup> edition.
- [45] J. Ohlsson, P. Schlatter, P.F. Fischer, and D.S. Hennington. Direct numerical simulation of separated flow in a three-dimensional diffuser. *J Fluid Mech*, 640(1):307–318, January 2010.
- [46] N. Pelc, F. Sommer, K. Li, T. Brosnan, R. Herfkens, and D. Enzmann. Quantitative magnetic resonance flow imaging. *Magnetic Resonance Quarterly*, 10(3):125–147, September 1994.
- [47] N.J. Pelc, M.A. Bernstein, A. Shimakawa, and G.H. Glover. Encoding strategies for three-direction phase-contrast mr imaging for flow. *J Magnetic Resonance Imaging*, 1(4):405–413, July/August 1991.
- [48] T. Povey, K.S. Chana, T.V. Jones, and J. Hurrion. The effect of hot streaks on HP vane surface and endwall heat transfer: An experimental and numerical study. *J Turbomach*, 129(1):32–43, January 2007.
- [49] T. Povey and I. Qureshi. Developments in hot-streak simulators for turbine testing. *J Turbomach*, 131(1):031009–1 – 031009–15, July 2009.

- [50] V.M. Repukhov. Effects of compressibility and non-isothermal conditions on the performance of film cooling. *J Engineering Physics and Thermophysics*, 19(5):1401–1408, November 1970.
- [51] R.J. Roback and R.P. Dring. Hot streaks and phantom cooling in a turbine rotor passage: Part 1 - separate effects. *J Turbomach*, 115(4):657–666, October 1993.
- [52] R.J. Roback and R.P. Dring. Hot streaks and phantom cooling in a turbine rotor passage: Part 2 - combined effects and analytical modeling. *J Turbomach*, 115(4):667–674, October 1993.
- [53] D. Schiavazzi, F. Coletti, G. Iaccarino, and J.K. Eaton. A matching pursuit approach to solenoidal filtering for three-dimensional velocity measurements. *J Computational Physics*, 263(1):206–221, April 2014.
- [54] O.P. Sharma and T.L. Butler. Predictions of endwall losses and secondary flows in axial flow turbine cascades. *J Turbomach.*, 109(2):229–236, April 1987.
- [55] C. Sieverding and P. Van Den Bosche. The use of colored smoke to visualize secondary flows in a turbine-blade cascade. *J Fluid Mech*, 134(1):85–89, May 1983.
- [56] C.H. Sieverding, T. Arts, R. Denos, and F. Martelli. Investigation of the flow downstream of a turbine trailing edge cooled nozzle guide vane. *J Turbomach*, 118(1):291–300, April 1996.
- [57] G. Suryan. Nuclear resonance in flowing liquids. *Proc Indian Acad Sci Sect A*, 33.
- [58] K.A. Thole and D.G. Knost. Heat transfer and film-cooling for the endwall of a first stage turbine vane. *J Heat and Mass Transfer*, 48(1):5255–5269, October 2005.

- [59] A. Vicharelli and J.K. Eaton. Turbulence measurements in a transonic two-passage turbine cascade. *Exp Fluids*, 40(6):897–917, March 2006.
- [60] S.D. Yapa, C.J. Elkins, and J.K. Eaton. Endwall vortex effects on turbulent dispersion of film coolant in a turbine vane cascade. *Proceedings of ASME Turbo Expo 2014 (GT2014-25484)*.
- [61] S.D. Yapa, C.J. Elkins, and J.K. Eaton. Quantitative MRI measurements of hot streak development in a turbine vane cascade. *Proceedings of ASME Turbo Expo 2015 (GT2014-42767)*.
- [62] S.D. Yapa, C.J. Elkins, and J.K. Eaton. Comparison of magnetic resonance concentration measurements in water to temperature measurements in compressible air flows. *Exp Fluids*, 55(11):1834–1 – 1834–14, Nov 2014.

Sayuri D. Yapa

I certify that I have read this dissertation and that, in my opinion, it is fully adequate in scope and quality as a dissertation for the degree of Doctor of Philosophy.

---

(John K. Eaton) Principal Adviser

I certify that I have read this dissertation and that, in my opinion, it is fully adequate in scope and quality as a dissertation for the degree of Doctor of Philosophy.

---

(Gianluca Iaccarino)

I certify that I have read this dissertation and that, in my opinion, it is fully adequate in scope and quality as a dissertation for the degree of Doctor of Philosophy.

---

(Christopher J. Elkins)

Approved for the University Committee on Graduate Studies

---